

Imaging and Control of Surface Reactions

vorgelegt von Diplom-Physiker

Pablo Sánchez Bodega

von der Fakultät II - Mathematik - und Naturwissenschaften
der Technische Universität Berlin
zur Erlangung des akademischen Grades

Doktor der Naturwissenschaft

-Dr.rer.nat.-

genehmigte Dissertation

Promotionsausschuss:

Vorsitzender: Prof. Dr. E. Sedlmayr

Gutachter: Prof. Dr. M. Dähne

Gutachter: Prof. Dr. H. H. Rotermund

Tag der wissenschaftlichen Aussprache: 15.04.2008

Berlin 2008

D 83

Kurzfassung

Ein faszinierendes Phänomen in räumlich gedehnten Systemen, die sich weit vom thermischen Gleichgewicht befinden, ist die spontane Strukturbildung. Unter den ausgedehnten Systemen heben sich durch ihr vielfältiges raumzeitliches Verhalten insbesondere die Reaktions-Diffusions-Systeme hervor. Technologische Fortschritte der letzten Jahrzehnten auf dem Gebiet der Abbildungsverfahren erlauben eine immer vollkommenere Charakterisierung der Raum-Zeit-Dynamik von Oberflächenreaktionen. Außerdem wurde einer Reihe von Ansätze nachgegangen um die raumzeitliche Dynamik zu gestalten und zu kontrollieren. Das spontane Verhalten eines Systems kann durch Verwendung schwacher Steuerimpulsen in eine bestimmte Richtung gelenkt werden, was eine Kombination vom theoretischen Verständnis des physikalischen Phänomens und dessen experimentellen Nachweises voraussetzt. In der vorliegenden Dissertation werden einige Verfahren zur visuellen Oberflächendarstellung in Experimenten mit externkontrollierten Oberflächenreaktionen verwendet, wobei zwei katalytische Reaktions-Diffusions-Systeme und deren entsprechende Strukturbildung erforscht werden: Die CO-Oxidation auf Platin (110) und der Lochfraß von Edelstahl.

CO-Oxidation auf Pt(110)-Einkristall-Oberflächen stellt ein bekanntes 2D-System mit einer Vielzahl möglicher Konzentrationsstrukturen dar. PEEM (Photoemissions-elektronen-Mikroskopie) wurde zur Erforschung dieser raumzeitlichen Strukturen verwendet. Verfahren für periodisches globales Forcieren wurden bei verschiedenen Resonanz-Zuständen eingesetzt um raumzeitliches Chaos zu steuern und vorher nie gesehene Strukturen zu induzieren. Es wird auch die gezielte Einführung von Rauschen, sowie die dabei auftretenden Strukturen vorgestellt. Des weiteren wurde Interferometrie verwendet um die Topografie einer ultra-dünnen Platinfolie zu vermessen. Die katalytische Dynamik der Reaktion und die damit verbundenen thermischen Effekte führen zu einer Deformierung der Folie und zur Entstehung von raumzeitlichen Strukturen.

Von erheblicher Bedeutung für die Sicherheit von Gebäuden und von Bauteilen in der Industrie ist das Problem des Lochfraßes von Metallen. Es wurde ein morphologischer Ansatz zum Verständnis des Prozesses und um den Weg zu neuen Test- und Verhütungsverfahren zu ebnen unternommen. Eine Kombination zweier Methoden der Oberflächenforschung, Atomarekräfterastermikroskopie und Rasterelektronenmikroskopie, wurde verwendet um die verschiedenen Stufen der Löcher in Edelstahl unter kontrol-

lierten Bedingungen bildlich darzustellen. Verschiedene präparative Verfahren wurden ebenfalls miteinander verglichen. Eine nähere Untersuchung der zeitlichen Entwicklung der generierten Löcher und deren Profile könnte dazu beitragen, neue Methoden zur Prüfung der Korrosionsfestigkeit von Legierungen zu erarbeiten.

Abstract

Spontaneous pattern formation is a fascinating phenomenon in spatially extended systems far from thermal equilibrium. Among extended systems, reaction-diffusion systems stand out for the wealth spatiotemporal behavior that they display. Technological advances in imaging during the last few decades have allowed an ever improving characterization of the space-time dynamics of surface reactions. In addition, a wide range of approaches have been pursued to design and control spatiotemporal dynamics. The spontaneous activity of a system can be steered in a desired direction by applying weak control impulses; this implies the combination of theoretical understanding of physical phenomenon with experimental verification. In this thesis, a number of surface imaging techniques are used in experiments where surface reactions are externally controlled; in particular, two catalytic reaction-diffusion systems and their corresponding pattern formation are studied: CO oxidation of platinum (110), and pitting corrosion on stainless steel.

CO oxidation on Pt(110) single crystal surfaces is a well known 2D system with a great number of possible concentration patterns; PEEM (photoemission electron microscope) was used for the study of such spatiotemporal structures. Periodic global forcing techniques were applied within different resonant regimes to control spatiotemporal chaos and to induce never before seen patterns. Purposeful introduction of noise into the system, and the corresponding emerging structures are also presented. Moreover, interferometry was used to map the topography of an ultra-thin platinum foil. The catalytic dynamics and thermal effects involved in the reaction resulted in the deformation of the foil and the emergence of spatiotemporal patterns.

For general safety and in industry, the problem of pitting corrosion on metals is crucial. A morphological approach has been done to understand this process and to pave the way for new testing and prevention techniques. The combination of two surface techniques, atomic force and scanning electron microscopy, was used to visualize the pits growth on stainless steel under controlled parameters. Different sample preparation methods are also compared. The study of the generated holes and their profiles in time can help develop new methods to test the alloys corrosion resistance.

Contents

1	Introduction	1
2	Background	5
2.1	Pattern formation and self-organization in reaction-diffusion systems . . .	5
2.2	Stability and bifurcation	7
2.2.1	Bifurcations and normal forms	10
2.3	Distributed active media	12
2.3.1	Monostable media	13
2.3.2	Bistable media	14
2.3.3	Excitable media	14
2.3.4	Oscillatory media	15
2.3.5	Chemical turbulence	16
2.4	Catalytic oxidation of CO on platinum (110)	17
2.4.1	Carbon monoxide and oxygen adsorption on Pt(110)	17
2.4.2	Reaction mechanism	23
2.4.3	Thermodynamics of the CO oxidation on platinum	27
2.4.4	Mathematical model	28
2.4.5	Pattern formation in the CO oxidation system	32
2.4.6	Experimental setup	35
2.5	Pitting corrosion on stainless steel	41

2.5.1	Corrosion mechanism	41
2.5.2	Experimental setup	44
3	Global control on the catalytic CO oxidation on Pt(110)	51
3.1	Resonant forcing	52
3.1.1	Preliminary approach	52
3.1.2	Experimental implementation	57
3.1.3	2:1 Resonant forcing	61
3.1.4	3:1 Resonant forcing	69
3.1.5	4:1 Resonant forcing	74
3.1.6	Forcing effect on propagating pulses (1:1, 2:1, 3:1, 4:1)	77
3.1.7	Conclusions	78
3.2	Effect of noise	80
3.2.1	Experimental implementation	80
3.2.2	Turbulence suppression by noise	81
3.2.3	Transitions anticipated by noise	84
3.2.4	CO ₂ production increment	88
3.2.5	Discussion	88
3.2.6	Appendix: reaction model	91
4	Ultra-thin Platinum foil	93
4.1	The sample and the setup	94
4.2	Calibration	98
4.3	Titration experiments	101
4.3.1	Reaction of oxygen with preadsorbed CO	101
4.3.2	Reaction of CO with preadsorbed oxygen	103
4.3.3	Parameter dependence of the titration	103

4.4	Pattern formation	106
4.5	Sensitivity of the method	108
4.6	Discussion	111
4.7	Appendix: algorithm for the topography reconstruction	115
5	Pitting corrosion on stainless steel	119
5.1	AFM <i>in situ</i> experiments	120
5.1.1	Electrochemical unit	120
5.1.2	Sample preparation	122
5.2	Results	124
5.2.1	AFM	124
5.2.2	SEM	128
5.3	Conclusions and future work	128
6	Summary	131
6.1	CO oxidation on Pt(110)	131
6.2	Pitting corrosion on stainless steel	133
	Bibliography	135
	Acknowledgments	152
	Publications	153
	Curriculum Vitae	154

Chapter 1

Introduction

“The scientist does not study nature because it is useful; he studies it because he delights in it, and he delights in it because it is beautiful. If nature were not beautiful, it would not be worth knowing, and if nature were not worth knowing, life would not be worth living”

Henri Poincaré

Why are the furs of certain animals, like the leopard (Fig. 1.1), spotted whereas the furs of others are striped (tiger, zebra)? Why are the spots of the giraffe much bigger than and different from those of the leopard? Why do some animals, such as the mouse and the elephant, not have any pattern at all? Why do some animals, such as the cheetah and the jaguar, have spotted bodies and striped tails, but there are no animals with striped bodies and spotted tails?

All of these questions can be addressed by a mathematical modeling. James D. Murray proposed a model [1, 2] that describes a reaction-diffusion system in which two different chemical products react and propagate through the skin: one which stimulates the production of melanin (coloring the skin) and one which inhibits this production. This is an example of a reaction-diffusion system, in which a unique set of differential equations seems to reproduce most of the animal fur patterns found in nature.

Although pattern formation has always been a major attraction and artists have repeatedly been inspired by spatiotemporal regularities in nature, its study as we know it began in the early 1950's in two quite different places. First, theoretical work was done by the English mathematician Alan Turing (1912-1954) on morphogenesis not long before he died (the term "morphogenesis" is now referred to by the generally more understandable term "pattern formation"). He showed that the coupling of nonlinear kinetics with diffusion may lead to spatial differentiation and structures (which were later named Turing patterns) [3]. Second, completely independent from Turing, there was the important experimental work of the Russian biophysicist Boris Belousov (1893-1970). He was the first to report the complex dynamical behavior of nonlinear reaction kinetics coupled with a diffusive transport in the oxidation of malonic acid [4]. At that time much of Belousov's work was either unpublished or unrecognized for many years. Therefore, the theory of reaction-diffusion lay dormant until around 1968 when a number of paths came together. A Russian biochemist named Anatoly Zhabotinsky had been improving Belousov's experimental work and Western scientists learnt of it at a symposium in Prague in 1968. At the same time, the (Russian born) Belgian chemist Ilya Prigogine (1917-2003) and co-workers following up Turing's work formulated and analyzed a model for chemical self-organizing non linear reactions (known as the Brusselator), which fitted in with some of Prigogine's earlier work [5]. This earlier work showed that the spontaneous creation of order is not forbidden by the Second Law of Thermodynamics, and later played a significant role in Prigogine's 1977 Nobel Prize for Chemistry; by the exchange of matter and energy with the environment, open systems far from thermodynamic equilibrium are able to export entropy, so that spontaneous ordered patterns can emerge [6].

The mathematical foundations to adequately describe the nonlinear dynamics, nowadays adapted to reaction-diffusion systems far from equilibrium, are based on the work of the French mathematician and physicist Henri Poincaré (1854-1912) [7]. He first described the complex dynamics of systems with three degrees of freedom. Since then, nonlinear dynamics has been intensively investigated, in particular chaotic behavior and instabilities due to parameter changes (bifurcations) [8].

Today, pattern formation is a major branch of nonlinear science, where a common set of fundamental concepts are used to describe how non-equilibrium processes lead to (often visible) structures to appear in a wide variety of complex systems within physics, chemistry, geology, biology, and sociology.

A particular exemplary reaction-diffusion system are spatiotemporal patterns evolving during chemical reactions on surfaces. The field of surface science was established about a century ago by Irving Langmuir (1881-1957). “For his discoveries and investigations in surface chemistry” he was awarded with the Nobel Prize for Chemistry in 1932. Langmuir was a versatile scientist that dedicated part of his efforts to the foundation of modern surface science, with key contributions like the invention of the diffusion pump (of vital importance for vacuum techniques). He also introduced concepts like monolayer (ML), valence shell, and isotope, and he indicated the importance and lack of knowledge about heterogeneous catalysis [9].

During the last four decades, Gerhard Ertl (1936-) and coworkers have further developed surface science thanks to Ertl’s innovative approach to catalyzed chemical reactions. Partly due to his studies of the catalytic oxidation of CO on platinum, Ertl was awarded the Nobel Prize in Chemistry 2007. This particular chemical reaction has a clear practical relevance since CO is the product of incomplete combustion of carbon based fuels. Due to the extreme toxicity of CO is desirable to convert it to CO₂ for which, among others, cars are equipped with a catalytic converter. The macroscopic kinetics of the CO-Pt system features an oscillatory reaction rate (Fig. 1.1) [10] and nonlinear cooperative behavior along the surface [11], which have been extensively studied and interpreted through imaging techniques and models. Following that research line, and after the background provided in chapter 2, chapter 3 of this thesis describes global purposeful modifications of the CO-Pt reaction-diffusion system, namely resonant forcing and the artificial introduction of noise. Next, chapter 4 focuses on the particular case of an ultra-thin platinum foil: the temperature diffusion and the heat of adsorption and reaction play a causal role in reshaping the topology of the sample, which is characterized with the help of a new interferometric setup.

The information provided by direct real-time reaction visualization has frequently proved to be essential for the advance of surface science, particularly in the study of the spatial and temporal regularities of pattern formation. In the case of reaction-diffusion systems, PEEM (photoemission electron microscope, used in chapter 3), as described in [12] and subsequent improvements done in the Fritz Haber Institute, Berlin, made it possible to discover the profuse spatiotemporal pattern formation phenomena arising from the CO oscillatory reaction rates reported some years earlier [13]. Later, techniques like EMSI (ellipso-microscopy for system imaging), RAM (reflection anisotropy microscopy), and interferometry (as presented in chapter 4) played an important role in the understanding of active media and cooperative behavior in surface reactions.

Another relevant surface chemical reaction that presents a cooperative and nonlinear behavior is the pitting corrosion of metals. In 2004, Rotermund's group succeeded in observing the propagation of corrosion on stainless steel with two different microscopes simultaneously: an ellipsometric and an optical microscope. The combination of imaging techniques turned out to be a successful approach: autocatalytic onset of pitting [14] and corrosion front propagation governed by diffusion mechanisms were reported [15]. In the present work (chapter 5), two well-know surface techniques, AFM and SEM, are combined to take on the problem of the morphology of corrosion pits, aiming at a better understanding of the process itself and to substantiate old and new models.

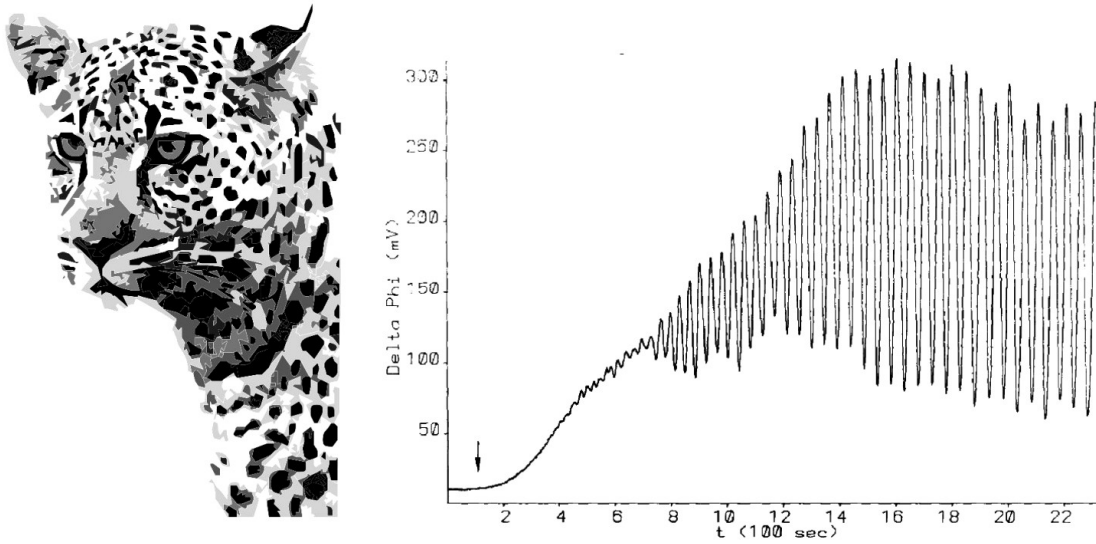


Figure 1.1: Left, image of the patterned fur of a leopard (modified from [16]). Right, plot reproduced from [10]: slow growth of periodic CO reaction rate oscillations on Pt(110) after an increase of oxygen pressure (marked with an arrow) from 1.5×10^{-4} to 2.0×10^{-4} Torr within 100 seconds ($T = 470$ K, $p_{CO} = 2.3 \times 10^{-5}$ Torr).

Chapter 2

Background

This chapter pertains to the scientific theoretical frame and the experimental setups involved in the present thesis. The first sections pay special attention to reaction-diffusion systems in general, the CO oxidation on Pt(110) in particular, and the corresponding spatiotemporal pattern formation and imaging. The last part discusses the pitting corrosion on stainless steel as a cooperative mechanism and the experimental techniques used to characterize it.

2.1 Pattern formation and self-organization in reaction-diffusion systems

Regular patterns are found in abundance in nature, from the ripples of a desert dune to the spots on a cheetah's fur. There has been a flurry of recent research activity seeking to explain their appearance and evolution. The preference of one pattern before another has turned out to be an inherent nonlinear phenomenon [17].

The term “self-organizing” seems to have been first introduced in 1947 by the psychiatrist and engineer W. Ross Ashby [18], but did not become commonplace in the scientific literature until its adoption by physicists and researchers in the field of complex systems in the 1970s and 1980s.

Synergetics is an interdisciplinary field of research that deals with material or immaterial systems, composed of, in general, many individual parts [19]. It focuses its attention on the spontaneous, self-organized emergence of new qualities which may be structures, processes, or functions. Synergetics looks for general principles of self-organization independent of the nature of the individual parts that make up the system.

The inner organization of an open system may increase in complexity without being guided or managed by an outside source. Such self-organizing systems typically display spontaneous formation of patterns. They are present in different disciplines such as biology, cybernetics or human society. Self-organization in chemistry encompasses a number of systems, namely liquid crystals, autocatalytic networks, reaction-diffusion systems and oscillating chemical reactions.

Spatial and temporal patterns can be observed in far from thermodynamic equilibrium systems of reacting and diffusing chemical compounds: diffusion links together the dynamics of neighboring points in space, and in combination with the nonlinear reaction kinetics, results in the formation of a wide variety of spatiotemporal structures.

Among homogeneous catalytic reactions, one of the first recorded examples of pattern formation stemming from a reaction-diffusion phenomena is the 3D Belousov-Zhabotinsky reaction, where malodyc acid is oxidized by bromate ions in the presence of a ferroin catalyst: oscillating spirals and target patterns are seen with alternating color arms or rings.

Within heterogeneous catalysis, an outstanding example of 2D reaction-diffusion is the catalytic CO oxidation on Pt (110), which is one of the two systems to be studied in this thesis. It features spontaneous oscillations caused by the excitability of the system, where some local spatial coherence is introduced by diffusion; neighboring molecules or parts of the surface oscillate in some definite phase relation to one another.

The second system to be studied in this thesis is the corrosion and pit formation on metals, which can also be considered as a reaction-diffusion process. The transition in such a chemical system from a negligible small and localized damage to a highly affected corroded surface can be described using the conceptual framework of nonlinear dynamics [20]. Numerical simulations [21] based on the latter showed how interactions among nucleation events can lead to the formation of clusters of metastable pits and to an

explosive growth in the total number of pits. Later, experiments supported by combined optical techniques were able to visualize and confirm such a cooperative behavior [14, 15].

The temporal behavior of a reaction system is governed by rate equations involving the chemical concentrations. Therefore, the spatiotemporal dynamics of a reaction-diffusion system may well be defined by adding diffusion terms to the rate equations. A general system of reaction rate equations is given by

$$\dot{\mathbf{u}} = \mathbf{f}(\mathbf{u}, \mathbf{p}) \quad (2.1)$$

where $\mathbf{u} = (u_1, u_2, \dots, u_n)$ represent the state of each individual element within the active media, \mathbf{p} denotes the set of n parameters p_j , and \mathbf{f} represents the vector containing the kinetic terms. Eq. 2.1 describes homogeneous dynamics where the reactor is well stirred and so diffusive transport is absent in the resulting uniform distribution of reactants.

For a system of n species, a general form of the diffusion equation can be written as

$$\partial_t \mathbf{u} = \mathbf{D} \nabla^2 \mathbf{u}. \quad (2.2)$$

The diffusion matrix \mathbf{D} often adopts the diagonal form if diffusion of the different species can be considered independent from each other. Combining Eq. 2.1 with Eq. 2.2, the general reaction-diffusion equation for n components can be written as:

$$\partial_t \mathbf{u} = \mathbf{f}(\mathbf{u}, \mathbf{p}) + \mathbf{D} \nabla^2 \mathbf{u}. \quad (2.3)$$

2.2 Stability and bifurcation

The analysis of the system dynamics starts with its temporal behavior, neglecting the spatial degrees of freedom. Each state of a system like (2.1) corresponds to a point in phase space, spanned by the variables $\mathbf{u} = (u_1, u_2, \dots, u_n)$, and the temporal evolution of the system describes its *orbits* (phase space trajectories). The dynamics is deterministic: only the initial conditions determine the state of the system through the function $\mathbf{f}(\mathbf{u}, \mathbf{p})$, because the time derivative in system (2.1) is of first order. The temporal behavior of the system is governed by the topology of its phase space, and since the system is dissipative, conservation laws for quantities such as energy do not exist. It may show regions where trajectories are trapped when $t \rightarrow \pm\infty$ (*limit sets*). They are called *attractors* if the

limit set is approached for $t \rightarrow +\infty$. A system may have various attractors, each having its attraction basin. Whereas if the trajectories described are periodic, they can be called *limit cycle*. All the initial conditions lying in a given basin of attraction will end up in the corresponding attractor. *Separatrices* set the limit between neighboring basins of attraction. Limit sets for $t \rightarrow -\infty$ are called *repellers*.

Next comes the stability analysis of such *fixed points* \mathbf{u}^s . They are defined by the condition $\dot{\mathbf{u}} = \mathbf{0}$. A fixed point \mathbf{u}^s is said to be asymptotically stable if small perturbations $\delta\mathbf{u}(t) \equiv \mathbf{u}(t) - \mathbf{u}^s$ of that state are damped down. Stability is checked through a linear stability analysis. The difference vector $\delta\mathbf{u}(t)$ is inserted into Eq. 2.1 and \mathbf{f} is expanded around \mathbf{u}^s in a Taylor series, where only the linear term is kept, yielding

$$\dot{\delta\mathbf{u}} = \mathbf{J}(\mathbf{u}^s) \delta\mathbf{u} \quad \text{with} \quad J_{ij} = \frac{\partial f_i}{\partial u_j}. \quad (2.4)$$

The real parts of the eigenvalues $\lambda_1, \lambda_2, \dots, \lambda_n$ of the Jacobian \mathbf{J} at the fixed points \mathbf{u}^s are the exponential growth rates of the perturbation $\delta\mathbf{u}(t)$ along the eigenvectors of \mathbf{J} , and therefore, determine the stability of \mathbf{u}^s :

$$\bullet \quad \text{if } \forall i \in [1, n], \operatorname{Re} \lambda_i < 0 \quad \Rightarrow \mathbf{u}^s \text{ asymptotically stable} \quad (2.5)$$

$$\bullet \quad \text{if } \exists i \in [1, n], \operatorname{Re} \lambda_i > 0 \quad \Rightarrow \mathbf{u}^s \text{ asymptotically unstable} \quad (2.6)$$

The application of the linear stability analysis assumes that higher order terms $\mathcal{O}(|\delta\mathbf{u}|^2)$ have no influence on the topology of the trajectories close to the fixed points. If at least one eigenvalue of the Jacobian is zero while the others are negative, a linear analysis is not sufficient; this happens at *bifurcations* and will be discussed later. We will consider now only *hyperbolic* fixed points, those with eigenvalues real part different from zero.

Linear stability analysis of a fixed point in a two-dimensional phase space yields to a quadratic equation for the eigenvalues λ_1 and λ_2

$$\lambda_{1,2} = \frac{1}{2} \left(\operatorname{Tr} \mathbf{J} \pm \sqrt{(\operatorname{Tr} \mathbf{J})^2 - 4 \operatorname{Det} \mathbf{J}} \right), \quad (2.7)$$

where $\operatorname{Tr} \mathbf{J}$ denotes the trace and $\operatorname{Det} \mathbf{J}$ the determinant of the Jacobian \mathbf{J} . Depending on their eigenvalues, the fixed point stemming from such a system can be stable or unstable, and can be classified as *nodes*, *foci*, or *saddle points*. A node possesses two real

eigenvalues. A focus has two complex conjugated eigenvalues. A fixed point is a saddle point if it has positive and negative eigenvalues. The different types of fixed points for a two-dimensional vector field are summarized in Fig. 2.1.

Furthermore, to understand the dynamics of a system requires an analysis of its *nullclines*. That is, curves, planes, or hyper-surfaces in phase space on which the temporal derivative of one of the dynamical variables is zero ($\dot{\mathbf{u}}_i = 0$). The intersections between nullclines correspond to fixed points of the system.

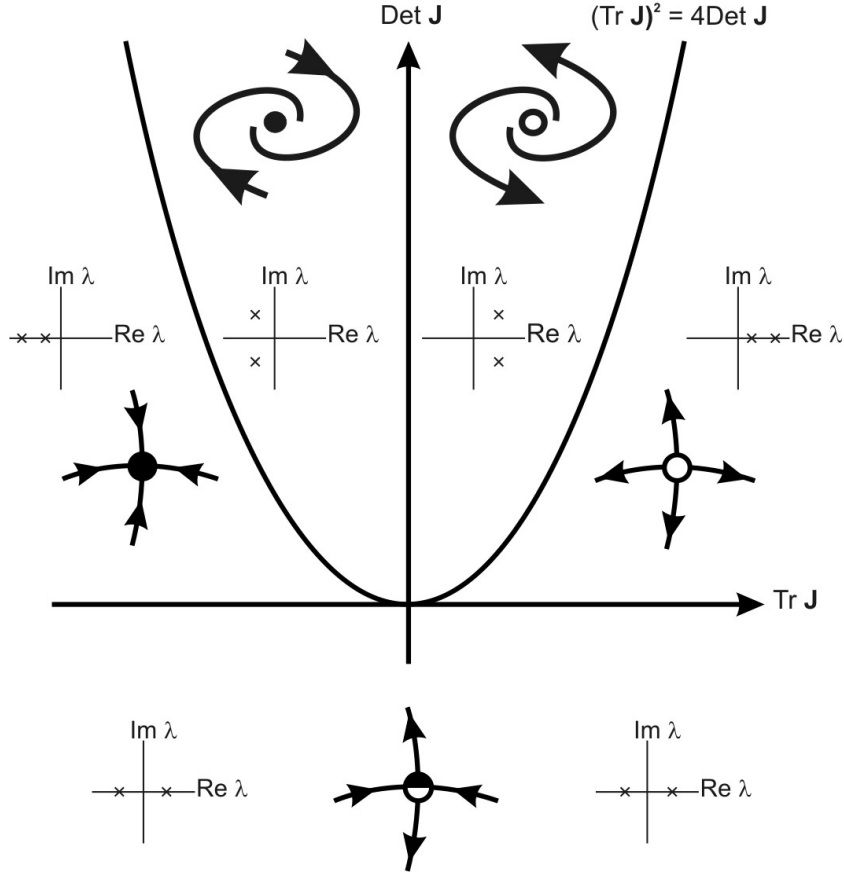


Figure 2.1: Hyperbolic fixed points in two-dimensional vector fields. Type and stability of a fixed point is determined by the eigenvalues of the Jacobian \mathbf{J} . The line $\text{Det } \mathbf{J} = 0$ separates saddles from nodes and the curve $(\text{Tr } \mathbf{J})^2 = 4 \text{Det } \mathbf{J}$ nodes from foci. The insets schematically display the corresponding eigenvalues in the complex plane.

2.2.1 Bifurcations and normal forms

At a bifurcation there is a sudden qualitative-dynamics change in response to changes in one or more parameters of the equations that describe the temporal behavior of a system, for instance Eq. 2.1 in section 2.1. There will be obvious differences in the phase portrait, and there will typically be a change in the number and stability properties of fixed points or periodic orbits. The parameters that lead to these changes are called *bifurcation parameters* and the point in parameter space at which the changes occur is referred to as *bifurcation point*. If we let μ be a vector of a bifurcation parameter, then the critical value for $\mu = \mu_c$ is a bifurcation point. Local bifurcation theory is concerned with dynamics changes in the neighborhood of a fixed point or periodic orbit. There also are global bifurcations with a large-scale impact [22] which will not be considered here.

For simplicity and suitability with the following chapters, let's just consider a stationary state \mathbf{u}^s which lies in the two-dimensional phase space and which depends only on one parameter p . It presents two cases of interest: either one real eigenvalue of the Jacobian \mathbf{J} changes sign, or a pair of complex conjugate eigenvalues of \mathbf{J} crosses the imaginary axis.

In the first case, the matrix \mathbf{J} becomes singular ($\text{Det}\mathbf{J} = 0$) at the critical parameter value $\mathbf{p} = \mathbf{p}_c$ and, according to the implicit function theorem [8, 23], the solution $\mathbf{u}_s(\mathbf{p})$ is no longer a smooth function of p . This implies a change of stability on the fixed point and the existence of new stationary solutions; in such so called *saddle-point* or fold bifurcation a new stationary stable solution appears. Besides that, another bifurcation known as *pitchfork bifurcation* (Fig. 2.2) may also appear if one real eigenvalue becomes positive. Here, a stable fixed point loses its stability and at the same time two new stable fixed points appear. In other words, the system is then bistable. In the second case, the matrix \mathbf{J} is invertible at the parameter value $\mathbf{p} = \mathbf{p}_c$, and the stationary solution $\mathbf{u}_s(\mathbf{p})$ remains a smooth function at this bifurcation point, the trace $\text{Tr}\mathbf{J}$ of the Jacobian vanishes at that parameter value \mathbf{p}_c and a *Hopf bifurcation* occurs (Fig. 2.3). For the present work, this is one of the most important kind of bifurcation because it is the simplest case leading to periodic behavior in time; once the bifurcation point is crossed, a focus loses its stability and gives rise to a harmonic limit cycle, small in amplitude, that follows a square root dependence close to the bifurcation point. Far from the Hopf bifurcation, the oscillations may become anharmonic and increase significantly in amplitude.

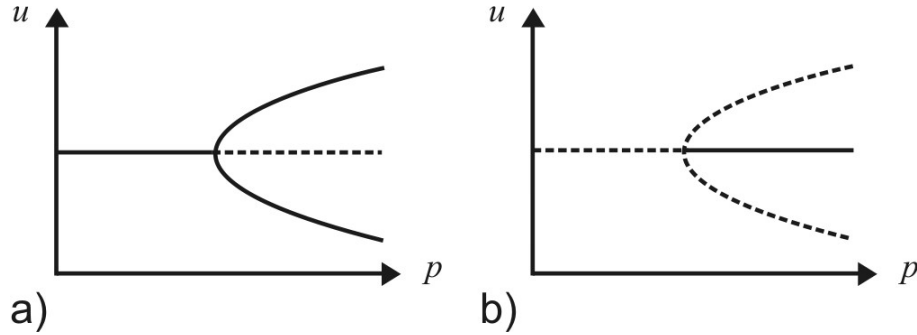


Figure 2.2: Pitchfork bifurcations diagrams. a) supercritical and b) subcritical pitchfork bifurcations. Stable solutions are shown as bold lines and unstable solutions as dotted lines.

Some bifurcations (Hopf or pitchfork for instance) may appear in a super- or subcritical form. In a *supercritical* bifurcation, the existing solutions become unstable while newly emerging solutions are stable. In a *subcritical* bifurcation the opposite occurs. Examples are shown in Fig. 2.2 and Fig. 2.3.

One of the main methods of simplifying dynamical systems is to reduce the dimension of the system. Center manifold theory is a rigorous mathematical technique that makes this reduction possible, at least near equilibria [23]. Close enough to a bifurcation and after an eventual short transient, the dynamics of the system 2.1 takes place on the center manifold, which is of great advantage: close to a bifurcation the study of the complete dynamics is reduced to the analysis of the center manifold. The so-called *normal form* is the differential equation that describes the center manifold system, and as its dimensionality is normally lower than the phase space dimension n , the reduced system is usually easier to solve. Furthermore, the normal form is universal and all dynamical systems undergoing the same bifurcation can be described by the same normal form close to the bifurcation point.

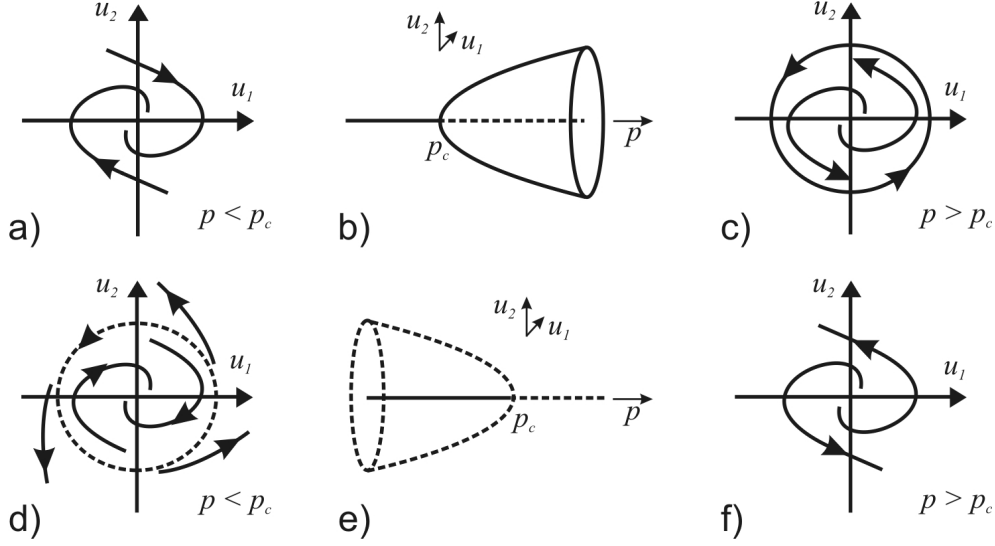


Figure 2.3: Hopf bifurcation diagrams for b) supercritical and e) subcritical cases, with their corresponding phase plane diagrams close to the bifurcation for $p < p_c$ [a) super- and d) subcritical], and $p > p_c$ [c) super- and f) subcritical]. Stable solutions are shown as continuous lines, unstable solutions as dashed lines.

2.3 Distributed active media

A spatially distributed system can be viewed as a large population of interacting non-linear active elements, with a certain degree of coordination within its individual parts, which are either distinct units or represent sufficiently small pieces of a bigger continuous medium. Active media are indeed commonly classified according to the local dynamics of their individual elements; many systems described by Eq. 2.3 feature either monostable, bistable, oscillatory, or excitable behavior [24]. A reaction-diffusion system (section 2.1) is a model of a spatially extended (or distributed) medium and is described by a set of partial differential equations as shown in Eq. 2.3.

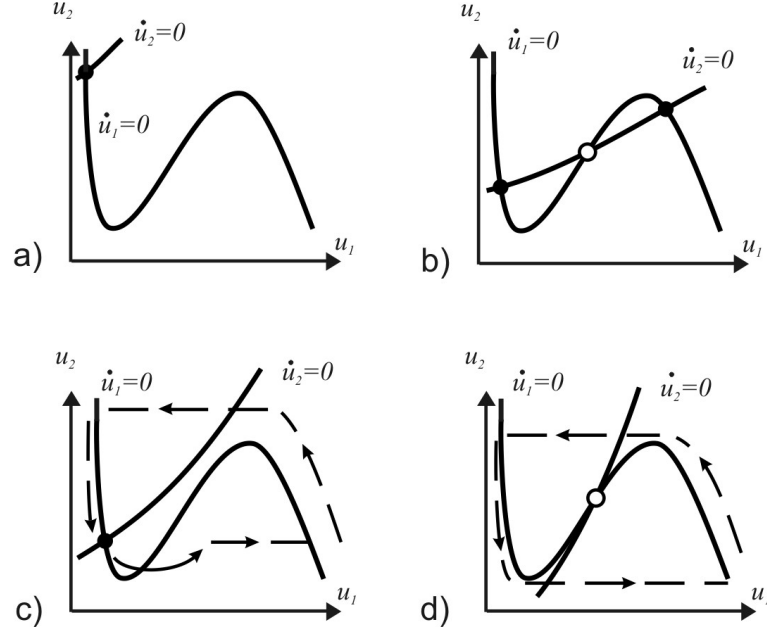


Figure 2.4: Schematic phase space diagrams showing nullclines and fixed points of a) a monostable, b) a bistable, c) an excitable, and d) an oscillatory system. The trajectories in phase space (dashed lines) illustrate in c) a typical excitable trajectory, and in d) the oscillatory limit cycle. Hollow circles represent unstable fixed points whereas filled circles are stable fixed points. They are displayed assuming a clear separation of time scales (u_1 dynamics are faster than u_2 dynamics).

2.3.1 Monostable media

Its dynamics are determined by a single stable fixed point (Fig. 2.4 a)). The system experiences damping after every perturbation, returning to the original steady state.

2.3.2 Bistable media

Bistable media consist of elements that have two steady states, stable under small perturbations. Nevertheless, sufficiently strong perturbations can cause transitions between these states (Fig. 2.4 b)). The most common pattern in bistable media is a trigger wave; its propagation triggers the transition from one stable stationary state of the medium to the other, crossing through an unstable saddle point. The propagation velocity of a flat front is determined by the properties of the bistable medium [24].

2.3.3 Excitable media

An element of an excitable medium exhibits one stable fixed point corresponding to the only intersection of the nullclines in phase space (Fig. 2.4 c)). The key idea in the concept of an excitable medium is that small perturbations on the stationary state decay and the dynamics converge quickly to the initial steady state, while a large enough perturbation (above a certain excitability threshold) involves a burst of activity before returning to its state of rest. This response is strongly nonlinear and is accompanied by a large excursion of the system's variables through the phase space. Such initially localized large perturbation spreads through the system by stimulating neighboring areas to a fast response, thus keeping the initial impulse alive. In the wake of this traveling pulse the system is refractory and cannot excite again. This is the recovery phase and once the *refractory time* is consumed, traveling waves can pass through the element again, re-starting the excitation excursion. This circumstance multiplies the number of possible patterns developed. In two-dimensional media, well known merging patterns are plane waves, target patterns (expanding concentric circles), and spirals [25]. A broken end of an excitable pulse curls and evolves into a rotating spiral wave with a characteristic wavelength and rotation frequency that depend exclusively on the system properties. Once triggered, parameter changes may cause the spiral wave to undergo drift motion, meandering [26, 27], or transit to chemical turbulence [28]. The wave velocity is normally determined by the reaction parameters and the diffusion coefficient. Two propagating waves annihilate each other after colliding. In reaction-diffusion chemical systems a fast response can propagate through diffusive coupling with adjacent areas.

In three dimensions, excitation waves can produce intricate figures such as scroll waves, rings, or knots [29].

Excitability is observed in a wide range of systems, namely lasers, chemical reactions, ion channels, neural systems, cardiovascular tissue, and climate dynamics. Common to all of them is the existence of a “rest” state, an “excited” (or “firing”) state, and a “refractory” (or “recovery”) state.

2.3.4 Oscillatory media

The phase space of an oscillator typically shows an unstable fixed point and a stable limit cycle, hence the system cannot settle down to a stationary configuration (Fig. 2.4 d)). For any initial condition, the oscillator ends up at the limit cycle to remain there. Kuramoto [30] and Winfree [31] demonstrated that the onset of synchronization in oscillator populations represents a phase transition. Below the transition point, the motion of individual oscillators in a multitude is not correlated. Nevertheless, as the interaction between them becomes stronger, correlations between dynamical states of oscillators in a fraction of the multitude develop: the frequencies of these oscillators become identical. Near the transition point, the size of the coherent oscillator group is small, but the group grows as interactions are increased. Moreover, the synchronization transition is accompanied by symmetry breaking. The phase of collective oscillations is arbitrary, but is fixed in a particular realization. Basic concepts of statistical theory of critical phenomena can be used in the studies of synchronization. Macroscopic oscillations may emerge from the mutual synchronization of a large number of more elementary, individual oscillatory processes. The mechanisms governing the spontaneous organization of such cyclic elements are intricate, and may be considerably dissimilar for different systems. Diffusively coupled arrays of periodic oscillators may exhibit rotating spiral waves, target patterns, and spatiotemporal chaos (chemical turbulence). The wave velocity is normally determined by the reaction parameters and the diffusion coefficient.

2.3.5 Chemical turbulence

Turbulence is a spatiotemporal phenomena, generally understood as irregular, apparently random motion of a fluid. In the context of reaction-diffusion extended systems, chemical turbulence is referred to as spontaneous spatiotemporal chaotic dynamics arising through diffusive coupling, the local dynamics itself being non-chaotic. This situation typically occurs in excitable and oscillatory media when diffusive coupling destabilizes uniform oscillations in the course of time, amplifying existing phase gradients, and it is characterized by irregular and spatiotemporal disordered patterns. An analysis of such turbulence can be performed based on the statistical properties of topological defects in the system [32].

Different turbulence suppression methods are considered in chapter 3, where global modifications of one of the reaction parameters are purposefully applied to the system; different ways of control and suppression of chemical turbulence on a surface reaction are there presented.

2.4 Catalytic oxidation of CO on platinum (110)

The occurrence of kinetic oscillations during the catalytic oxidation of CO on a platinum surface under continuous flow conditions has been investigated extensively in the recent past. These oscillations are coupled to periodic transformations between the two structural modifications of the Pt (110), which propagate across the surface area of the sample. Such a far from equilibrium system shows nonlinear surface reactions stemming into a number of interesting dynamics and spatiotemporal behaviors. The investigation of structures arising from the lateral variation of concentration species at the surface requires adequate techniques, and only became possible after the development of surface imaging methods like PEEM [33, 34], Reflection Anisotropy Microscopy (RAM), or Ellipso-Microscopy for Surface Imaging (EMSI) [13].

The present section is focused on a specific reaction-diffusion system, the catalytic oxidation of CO on platinum (110). The processes of adsorption of oxygen and CO, the mechanism of the reaction, the concentration pattern formation, and the reaction rate oscillations are presented. Finally, the experimental setup used in this work is described.

2.4.1 Carbon monoxide and oxygen adsorption on Pt(110)

This section overcomes the catalytic CO oxidation; first, a paragraph about the platinum (110) structure, which is followed by an explanation of the corresponding CO and oxygen adsorption. The reaction mechanism and its modeling can be better understood afterwards.

2.4.1.1 Platinum (110)

At room temperature, the clean surface of the face centered cubic (fcc) platinum crystal has a lattice parameter $a = 3.92 \text{ \AA}$ (Fig. 2.6), and the closest-neighbors distance between the platinum atoms $d = 2.77 \text{ \AA}$. The corresponding (110) surface has a (1×2) structure, also called missing row reconstruction because free rows alternate with platinum rows along the $[\bar{1}10]$ direction (Fig. 2.7) [35, 36, 37, 38, 39]. The missing row structure features a large fraction of energetically advantageous (111) microfacets. Nevertheless, platinum

is known to undergo an adsorbate-induced reconstruction [39, 40, 41] that yields a (1×1) structure, with the atoms arranged as in the bulk.

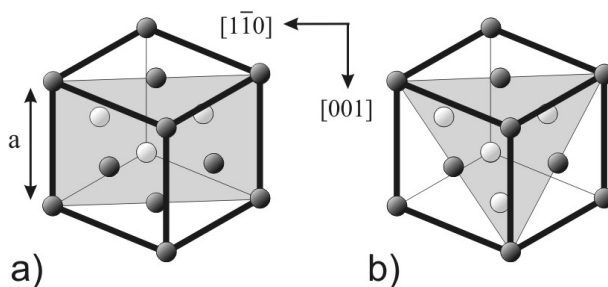


Figure 2.5: Face centered cubic (fcc) crystal structure: the shaded plane represents a) the (110) plane and b) the (111) plane. Reproduced from [42].

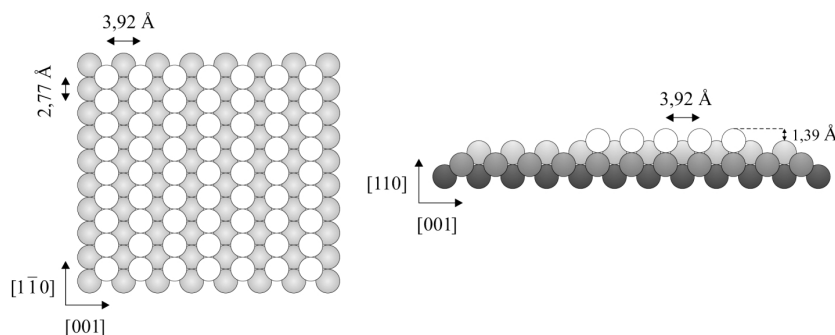


Figure 2.6: Hard-sphere model showing the (1×1) structure of the Pt(110) surface. Top view (left) and cross section (right) of the first layers. Reproduced from [43].

2.4.1.2 Carbon monoxide on Pt(110)

CO adsorption on d-metals (such as Cu or Pt) is molecular. It adsorbs through a weakly bound precursor state that allows diffusive mobility through the surface. On a Pt(110) crystal, CO molecules adsorb following the donation-backdonation Blyholder mechanism [44, 45] shown in Fig. 2.8. The 5σ and the 2π frontier molecular orbitals (MO) of the

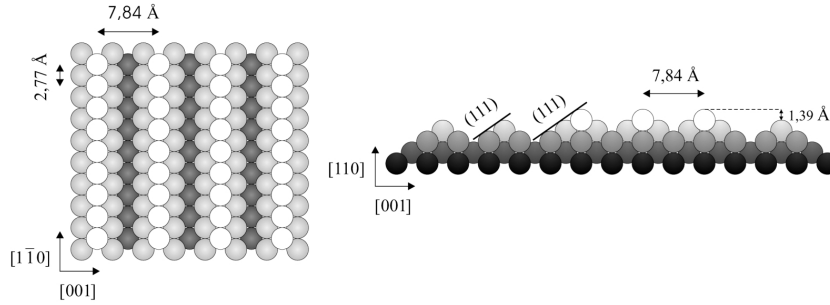


Figure 2.7: Hard-sphere model showing the (1×2) structure of the Pt(110) surface. Top view (left) and cross section (right) of the first layers. Reproduced from [43].

CO molecule are substantially modified by the presence of the metal surface. A filled 5σ single orbital interacts with the empty $d\sigma$ metal orbital leading to a partial transfer of electron density to the metal. At the same time, the filled $d\pi$ metal orbital overlaps with the 2π antibonding molecular orbital of the CO. As the 5σ and 2π MO are localized mainly at the carbon atom, the bonding occurs with the carbon facing the metal surface.

Initially, for the (1×2) structure, the CO sticking probability on Pt(110) $s_{co}^0 \approx 1$ [35, 46, 47], and remains almost constant for low coverage of CO. Nevertheless, for higher coverage ($u \geq 0.35$) the sticking coefficient decreases. According to Gasser and Smith who described it in [48], $s_{co} = s_{co}^0(1 - u^q)$ where q is a mobility parameter between 3 and 4. The CO saturation coverage on Pt(110) is equal to unity [35, 46, 49, 50].

The adsorption of CO on the missing row reconstructed (1×2) Pt(110) surface causes a lifting of the reconstruction. LEED analysis showed that the process starts for coverage of 0.2 ML (monolayer), and a bulk truncated (1×1) phase is completed for coverage of 0.5 ML [51]. STM observation [40] revealed that at 300 K this process is initiated by homogeneous nucleation of small characteristic (1×1) patches. Their further growth is limited by thermal activation; migration of Pt atoms is restricted to a few lattice sites. At higher temperatures, correlated jumps cause the lateral displacement of longer chains and the enhanced surface mobility leads to the formation of larger, strongly anisotropic (1×1) islands.

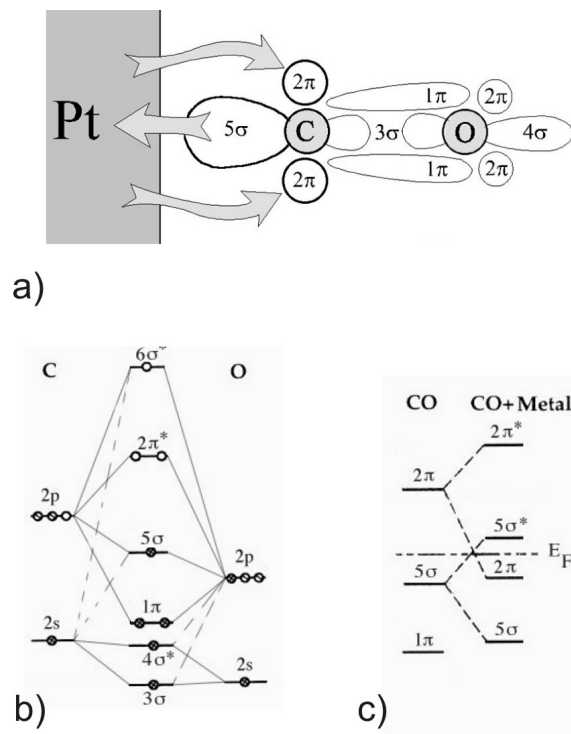


Figure 2.8: a) the Blyholder model of the CO bonding on platinum [44]. Molecular orbital corresponding to b) a free carbon monoxide, and c) a CO-metal [52].

CO is diffusively mobile on the Pt(110) surface, and has a diffusion constant that depends on the crystallographic orientation. On both the (1×1) and the (1×2) phases, the diffusion constant is larger in the $[1\bar{1}0]$ direction than in the $[001]$ orientation [53].

Thermal desorption spectra of adsorbed CO show a strong coverage dependence on the occupied lattice sites. For coverage below 0.4 ML a single peak is measured between 510 and 530 K (see Fig. 2.10 a)). This peak shifts towards lower temperatures with increasing coverage up to 0.5 ML, to remain fixed for even higher coverage. Nevertheless, at temperatures between 400 and 425 K, a second peak appears at higher coverage that shifts to lower temperatures with increasing coverage [46, 54, 55]. At saturation, the areas under both peaks are equal.

2.4.1.3 Oxygen on Pt(110)

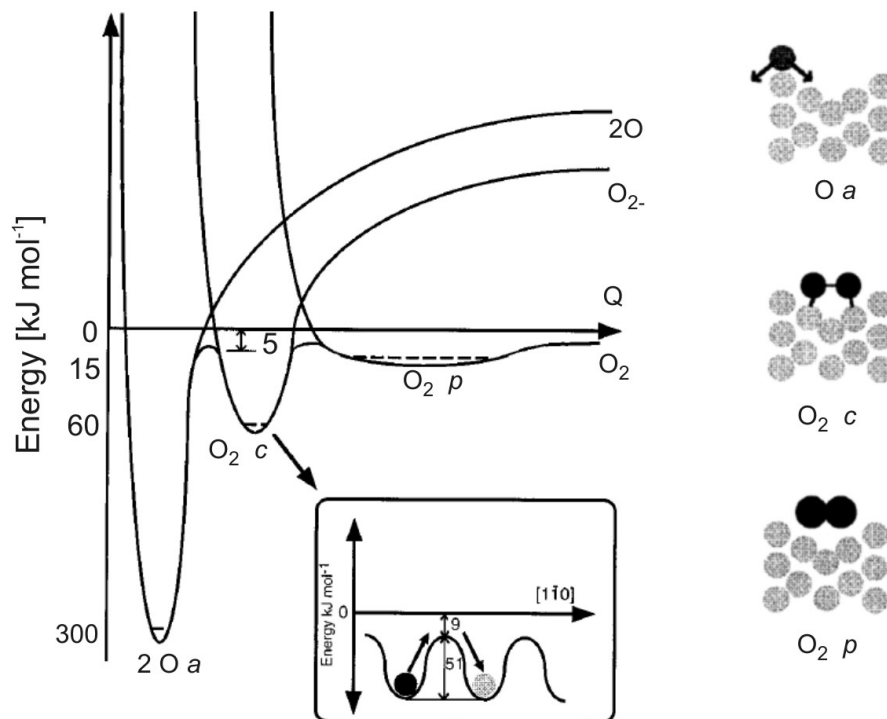


Figure 2.9: A schematic one-dimensional representation of the Potential Energy Surface (PES) for oxygen atomic adsorption (*a*), dissociative chemisorption of O_2 (*c*), and molecular physisorption of O_2 (*p*) on Pt(110) (1×2). *Q* represents an undefined reaction coordinate. Reproduced from [56].

Dissociative oxygen adsorption on the Pt(110) surface takes place at temperatures above 240 K [57]. Electron Energy Loss Spectroscopy (EELS) data suggests that oxygen follows a precursor mediated adsorption process [56]: the physisorbed state is a precursor to chemisorbed dioxygen, and the latter is the precursor state to the dissociative oxygen state (schematically represented in Fig. 2.9). Below 0.25 ML coverage oxygen is adsorbed into a fluxional state with constant rearrangement of adatoms, where alternating sites along the $[1\bar{1}0]$ rows can be occupied due to lateral repulsive interactions between these adatoms. A different regime is reached with coverage between 0.25 and 0.5 ML, where oxygen remains fixed at the fcc sites on the walls of the valleys (microfacets). Alternating sites are occupied, again, thanks to repulsive interactions between adatoms. The structures would give rise to a c -(2×4) or a (2×2) LEED pattern with ordering across

the missing rows ([001] direction). Instead, at oxygen coverage below 0.5 ML, a (1×2) LEED diffraction pattern is retained, indicating disorder between the rows [56]. At coverage greater than 0.5 ML, additional slow oxygen uptake produces a coverage-dependent variable unit mesh structure consistent with low density domain walls; these structures are consistent with a (10×2) pattern at coverage of 0.75 ML (experimentally measured) [56].

The activation energies for oxygen diffusion are high and strongly dependent on the crystallographic orientation. Therefore, diffusion is basically limited to the $[1\bar{1}0]$ direction, never perpendicular to the missing row fringes, and highly coverage dependent [53]. Nevertheless, for the particular experiments presented in the following chapters, an experimental temperature range below 540 K allows for neglecting oxygen diffusion.

Oxygen desorbs exclusively in molecular form. Thermal desorption spectra for low coverage shows a single peak around 840 K (see Fig. 2.10 b)). As the coverage increases, the peak shifts to lower temperature, and for high coverage, desorption takes place at 740 K [56, 57] by a direct process.

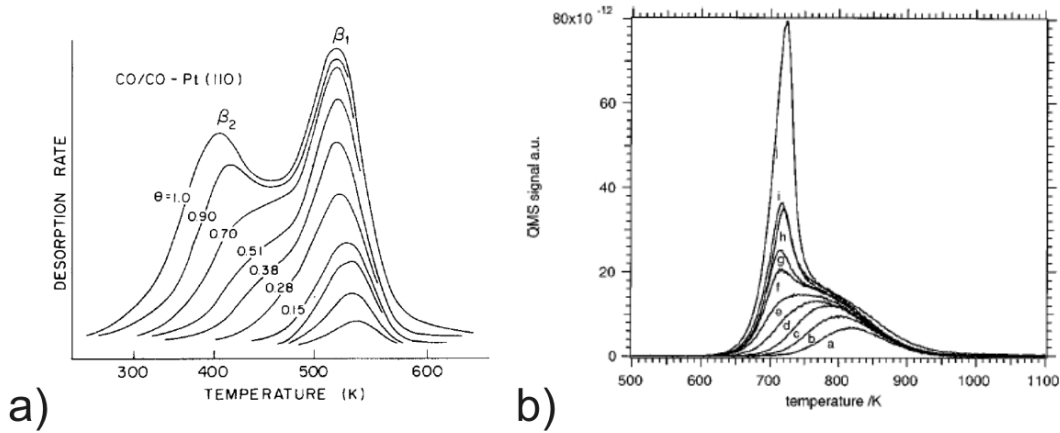
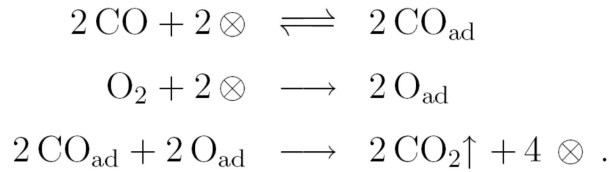


Figure 2.10: Temperature programmed desorption spectra. a) CO from Pt(110), for different surface fractional coverage $\theta = 1.0, 0.9, 0.7, 0.51, 0.38, 0.28, 0.15$. Reproduced from [54]. b) oxygen from Pt(110) for different surface coverage: *a* 0.11 ML, *b* 0.17 ML, *c* 0.24 ML, *d* 0.28 ML, *e* 0.33 ML, *f* 0.41 ML, *g* 0.45 ML, *h* 0.47 ML, *i* 0.52 ML. Reproduced from [56].

2.4.2 Reaction mechanism

The previous sections were dedicated to the adsorption of CO and oxygen on Pt(110) independently. This section considers a system combining both species in the gas phase, and their reaction on a platinum sample. It has been well established that the reaction mechanism follows a Langmuir-Hinshelwood scheme [58], described by the following three equations:



where \otimes stands for a free adsorption site and the index ‘*ad*’ indicates that the species is in adsorbed state. Both CO and oxygen have to adsorb from the gas phase on the surface for the catalytic reaction to take place: an adsorbed CO molecule can react with an adsorbed oxygen atom from a neighboring lattice site to form carbon dioxide, which is immediately released to the gas phase (see Fig. 2.11 a)). This process leaves two vacant sites on the platinum surface, available for adsorption of new reactants. Adsorbed CO molecules are bound to the surface considerably more weakly than oxygen atoms. Within the frame of the experimental temperature conditions of this work, desorption and diffusion mobility of CO have to be taken into account, while both can be neglected in the case of adsorbed oxygen.

In the reaction environment, the reactants compete for the empty adsorption sites; for a number of reasons CO has advantages in that competition over oxygen. First, a single empty adsorption site is enough for a CO molecule to stick on the catalytic surface, while oxygen needs two adjacent free sites. Second, precursor mediated processes allow CO molecules to hop between different locations, increasing the probability of binding to an adequate adsorption site. Third, oxygen forms a very open adlayer structure, allowing CO to adsorb and react (see Fig. 2.11 a)). In contrast, a fully CO covered surface prevents completely the adsorption of oxygen and, hence, poisons the reaction [59] (see Fig. 2.11 b)). This behavior is referred to as *asymmetric inhibition* and induces *bistable* dynamics in a wide range of parameters, with a mainly oxygen covered reactive state and a CO covered non-reactive state coexisting beside each other.

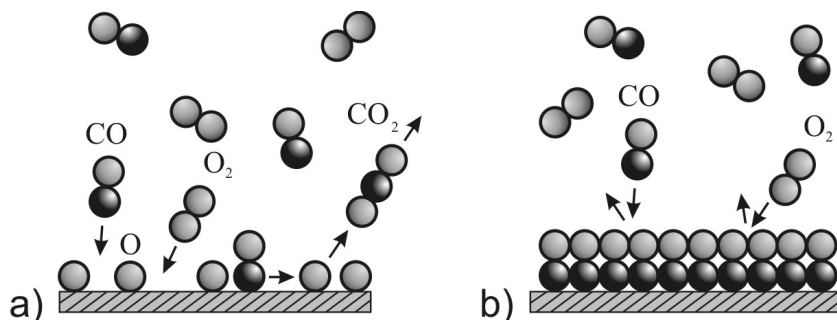


Figure 2.11: a) illustrative drawing of the principles involving adsorption of CO and oxygen molecules, diffusion of CO, and CO₂ formation. b) CO compact adsorbate layer completely covering the platinum and poisoning the reaction.

An additional mechanistic step is required in order to explain the reaction mechanism, crucial for the development of the *excitable* and *oscillatory* dynamics: an internal negative feedback loop (see Fig. 2.12). It consists of a structural transition of the Pt(110) surface between (1×2) and the (1×1) bulk terminated structure. When the crystal is freshly prepared, the surface reconstructs a (1×2) structure (missing row phase). The driving force for this reconstruction is the formation of (111) microfacets that are energetically favored. When CO is admitted to the (1×2) surface, this reconstruction will be lifted and a phase transition to the (1×1) phase occurs [35, 40, 55]. This reconstruction starts at a fractional coverage of 0.2, and is considered complete at a coverage of 0.5. The activation energy for this phase transition is 29 kJ/mol [60]. Under oscillation conditions, when there is a flow of both oxygen and carbon monoxide, the following can happen for particular reaction parameters (temperature and partial pressures): when the surface is CO covered (low reactivity), the reconstruction is lifted but the sticking coefficient of oxygen on the non-reconstructed surface is higher compared to the reconstructed one by a factor of 2 [61]. More oxygen will therefore be able to adsorb in the competitive adsorption process. As a consequence, the surface will show an oxygen covered state. And once the surface is oxygen covered, with no CO species to lift the reconstruction, it will reconstruct again. The reconstructed surface has a low sticking coefficient for oxygen, thus enabling CO to take over. Now the surface is mainly CO covered and the

oscillation cycle (loop) starts again. In this picture, the velocity of the phase transition is a key factor, because it determines the system oscillating period.

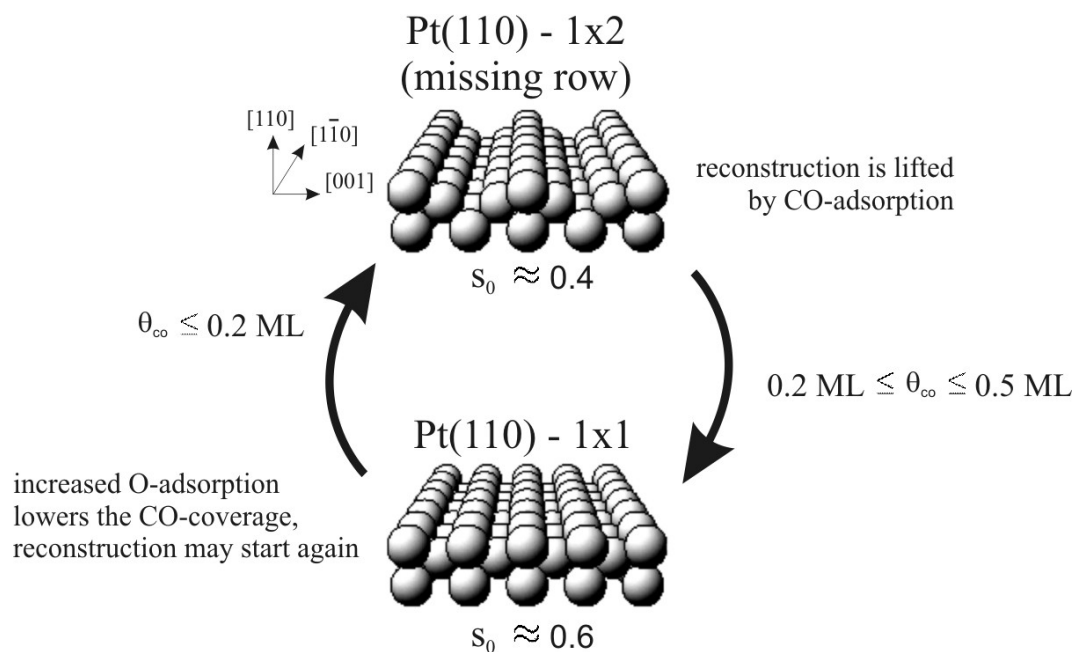


Figure 2.12: Schematic illustration of the adsorbate induced structural transition (feedback loop) of the Pt(110) surface.

2.4.2.1 Spatial coupling

Two different mechanisms establish spatial coupling between the different locations on the catalytic surface: CO diffusion and gas phase global coupling. Surface diffusion of adsorbed CO molecules gives rise to local coupling between neighboring sites. Diffusion is fast along the $[1\bar{1}0]$ orientation of the Pt(110) single crystal surface, while it is slower by a factor of about 2 parallel to the $[001]$ orientation of the substrate lattice. Due to this diffusion anisotropy, spatial patterns are elliptically deformed. The second type of spatial coupling acts via gas phase as a consequence of mass balance in the reaction. Since the mean free path of the gases at low pressures is typically large in comparison to the size

of the chamber, local partial pressure variations that result from the consumption of the reactants, quickly extend to affect the whole system [62]. Consequently, the gas-phase coupling is global. It has been experimentally found that the interplay between diffusion and gas phase coupling can lead to such phenomena as synchronous oscillations [63], standing waves [34], and cellular structures [64]. The partial pressures variations due to gas phase coupling are typically less than 2 - 3 % in magnitude [65].

An additional coupling may stem from the reaction thermodynamics and the consequent heat flows, even with associated formation of patterns. Only for higher pressures [66, 67] or ultrathin catalysts (chapter 4) [68, 69] the effect of thermal coupling plays a role. At lower pressures isothermal conditions prevail and heat transport is absent.

2.4.2.2 Faceting

Below the critical temperature of 530 K, another reversible restructuring process takes place on the Pt surface during the CO oxidation: *faceting*. The initially flat platinum surface facets under the influence of the catalytic reaction into new orientations; (100) steps are accumulated during the (1×1) to (1×2) reconstruction process. The direction of faceting ($[110]$) is perpendicular to the direction of the (1×2) reconstruction ($[001]$) [70]. Above this critical temperature, thermal reordering keeps the surface flat.

Faceting is a dissipative Turin structure [71], only obtained under non-equilibrium conditions in a continuous flow of CO and oxygen [70]. The facets are formed on a time scale of several minutes, and their size is of the order of 100 Å [70, 72]. The faceting process on Pt(110) increases the catalytic activity due to a higher oxygen sticking coefficient on the faceted surface [73, 74]. PEEM (see below) cannot image surface faceting, and only becomes apparent indirectly through its influence on the reaction dynamics.

2.4.2.3 Subsurface oxygen

Another feature of the reaction mechanism is the formation of *subsurface oxygen*. Under certain conditions, oxygen atoms not only adsorb on the surface, but an oxygen species may also migrate underneath the surface top layer. After being stored below the surface

for a certain time, oxygen atoms may later be released back onto the surface. The formation of subsurface oxygen only happens on the nonreconstructed (1×1) surface, and in return, subsurface oxygen tends to stabilize this phase, affecting the reaction dynamics. It is for instance responsible for the reflective collision of traveling excitation waves, a rather unusual phenomenon in reaction-diffusion systems [63]. PEEM (see section 2.4.6.2) images subsurface oxygen as very bright patches [75]: a dipole inversion when subsurfaced causes a decrease of the oxygen work function.

2.4.3 Thermodynamics of the CO oxidation on platinum

The heat of adsorption of CO and of oxygen on platinum are crucial parameters for the kinetic models of the CO catalytic reaction on Pt(110), as well as the surface desorption energies of CO₂. In the literature concerned with this point, insofar pertinent for the present section, special attention is paid to the work of Wartnaby *et al.* [76] within D. A. King's group because their data was obtained with the same kind of ultra-thin platinum sample employed here in chapter 4. The cited authors also show in great detail how the adsorption heat of CO and oxygen is strongly correlated with the sticking probability.

2.4.3.1 Adsorption of CO on Pt(110)

Different research groups using different methods [35, 76] agree that the adsorption heat of CO on Pt(110) at 300K has an initial value of 183 kJ/mol, decreases monotonically to 146 kJ/mol at 0.5 ML, reaching 125 kJ/mol at the saturation coverage of 0.88 ML.

2.4.3.2 Adsorption of O₂ on Pt(110)

The microcalorimetric heat measurement by Wartnaby *et al.* [76] was pioneering work on the interaction of oxygen with Pt(110); the following data is taken from their work. Initially, adsorption heat is 332 ± 10 kJ/O₂ mol, declining with coverage to 215 ± 24 kJ/O₂ mol at 0.35 ML, and reaching a steady-state value of 153 ± 50 kJ/O₂ mol for higher coverage.

2.4.3.3 Thermodynamics of the reaction

The reaction enthalpy of the carbon dioxide formation $\text{CO} + \frac{1}{2} \text{O}_2 \longrightarrow \text{CO}_2$ is -283.17 kJ/mol [77]. There are two experimental possibilities to let this reaction run on the whole platinum surface in a controlled way: a CO (O) monolayer covers the surface and reacts completely away with O (CO), releasing CO_2 to the gas phase. These chemical reactions are called titrations and the next paragraphs are centered in these two particular reactions, including data extracted from [76, 78, 79].

2.4.3.4 Titration of an oxygen monolayer with CO on Pt (110)

The enthalpy change associated with this reaction is described by:

$$\Delta H = \Delta H_{\text{CO}_2} - \Delta H_{\text{ad,O}}, \quad (2.8)$$

where ΔH_{CO_2} is the formation enthalpy of CO_2 , and $\Delta H_{\text{ad,O}}$ the adsorption energy of oxygen per CO_2 mol.

2.4.3.5 Titration of a CO monolayer with oxygen on Pt (110)

The standard enthalpy formation for this reaction can be written as:

$$\Delta H = 2\Delta H_{\text{CO}_2} - 2\Delta H_{\text{ad,CO}}, \quad (2.9)$$

where ΔH_{CO_2} is the formation enthalpy of CO_2 , and $\Delta H_{\text{ad,CO}}$ the adsorption energy of CO per CO_2 mol.

2.4.4 Mathematical model

Krischer, Eiswirth, and Ertl developed a kinetic model to describe the temporal dynamics of the catalytic oxidation of CO on Pt(110), consisting of a set of ordinary differential equations (ODEs) and neglecting the spatial degrees of freedom: the KEE model [80]. Depending on the choice of external parameters, the model is able to reproduce monostable, bistable, excitable, and oscillatory dynamics. Subsequently, diffusive

coupling was introduced to the model to reproduce spatially extended systems [81]. The KEE model is well established and has been successfully used to study the dynamics of catalytic CO oxidation on Pt(110) numerically. Many experimental observations of spatiotemporal pattern formation in the CO oxidation system could be reproduced at least qualitatively [82, 83, 84, 85, 86].

2.4.4.1 The KEE model

The model decomposes the entire reaction into elementary steps and consists of three coupled ordinary differential equations for the local dynamics:

$$\begin{aligned}
 \frac{\partial u}{\partial t} &= \overbrace{k_1 p_{CO} s_{CO}}^{\text{adsorption}} - \overbrace{k_2 u}^{\text{desorption}} - \overbrace{k_3 u v}^{\text{reaction}} + \overbrace{D_x \frac{\partial^2 u}{\partial x^2} + D_y \frac{\partial^2 u}{\partial y^2}}^{\text{diffusion}} \\
 \frac{\partial v}{\partial t} &= \overbrace{k_4 p_{O_2} s_O}^{\text{adsorption}} - \overbrace{k_3 u v}^{\text{reaction}} \\
 \frac{\partial w}{\partial t} &= \overbrace{k_5 (f(u) - w)}^{\text{reconstruction}}
 \end{aligned}$$

where u is the CO coverage, v the oxygen coverage, and w the local fraction of the surface found in the nonreconstructed (1×1) structure. The three of them are normalized between zero and one, and together can be regarded as an example of a dynamical system of type 2.1 (see section 2.1).

The production of carbon dioxide with rate constant k_3 is involved in the first two equations. Desorption reduces the CO coverage with a rate constant of k_2 , while for oxygen it can be neglected (see section 2.4.1). The adsorption processes of CO and oxygen are determined by the respective impingement rates k_1 and k_4 , the sticking coefficients s_{CO}^0 and s_O^0 , and the partial pressures p_{CO} and p_{O_2} of the two components. The CO diffusion term $D\nabla^2 u$ has also been added [81], as pointed out above.

Both sticking coefficients are coverage dependent. For s_{co} a precursor effect has to be considered and is modeled following Gasser and Smith [48]. In the case of oxygen sticking s_o , a second order kinetics in the fraction of free sites needs to be considered and the difference in sticking probability between the (1×1) and (1×2) surface structures has to be taken into account. Hence, the initial sticking probabilities of CO and oxygen on the clean surface can be written:

$$s_{co} = s_{co}^0 (1 - u^3),$$

$$s_o = [s_{o,1 \times 1}^0 w + s_{o,1 \times 2}^0 (1 - w)] (1 - u - v)^2.$$

In the third equation of the KEE model, the constant k_5 represents the transition rate between the (1×1) missing row structure and the (1×2) bulk terminated surface. The function f , describing the equilibrium value of w , is exclusively determined by u , because only CO induces a lifting of the (1×2) reconstruction. In the original form of the KEE model [80], a piecewise approximation of f was used. For computational convenience, a different approach has been frequently used in the more recent versions [87] which only deviates lightly from the piecewise original approximation,

$$f(u) = \frac{1}{1 + \exp\left(\frac{u_0 - u}{\delta u}\right)}. \quad (2.10)$$

Here, the parameter u_0 determines the threshold value above which adsorbed CO molecules significantly affect the surface structure, and δu determines the steepness of the threshold. Both functions, f and the original piecewise form, are compared in Fig. 2.13.

Three external control parameters can be varied freely, namely the partial pressures p_{CO} and p_{O_2} of the two reactants and the temperature. The rate constants k_2 , k_3 , and k_5 show a significant temperature dependence that is generally modeled assuming an Arrhenius-type relation,

$$k_i = \nu_i \exp\left(\frac{-E_i}{kT}\right). \quad (2.11)$$

The reaction specific parameters such as sticking coefficients or activation energies were taken from the literature or determined in experimental studies of the individual reaction steps [80, 88, 89].

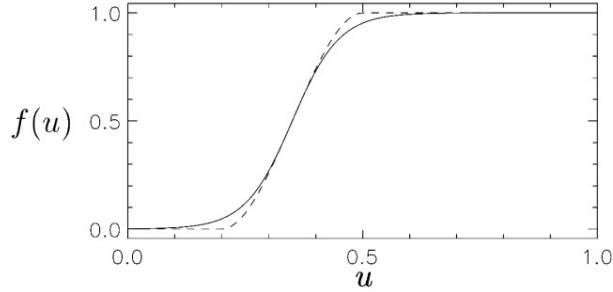


Figure 2.13: Plot of function $f(u)$ with $u_0 = 0.35$ and $\delta u = 0.05$ (solid line) and its piecewise original form (dashed line). Below $u \approx 0.2$, the surface is found almost completely in the reconstructed (1×2) structure, whereas the non-reconstructed (1×1) structure is almost exclusively present above $u \approx 0.5$. Reproduced from [65].

Introducing a spatial dependence of the variables u , v , and w , allows to model the dynamics on an extended single crystal surface. Since diffusion of oxygen can be neglected at the temperatures considered here, local coupling between the different locations on the platinum surface is only established by diffusion of CO ($D\nabla^2 u$).

2.4.4.2 Modifications

The KEE model has been changed and modified in many ways. In the previous section were mentioned the changes concerning f and the addition of the diffusion term $D\nabla^2 u$. A reduced two-variable version of the model was proposed with qualitatively similar results for many aspects of the spatiotemporal dynamics [90, 91]. Spiral waves [84, 92] and the emergence of chemical turbulence in the excitable regime [28, 93] were successfully studied using the two-variable version.

Furthermore, the three-variable model has been extended to account for additional phenomena that were considered irrelevant in the original version. An important effect is the global coupling through the gas phase. The model can be extended by an additional equation accounting for the evolution of CO partial pressure in the reaction chamber. In numerical simulations of the extended model, global coupling was found to influence the

spatiotemporal dynamics significantly, inducing *e.g.* standing waves and cluster patterns [94, 95, 96, 97, 98, 99, 100]. Subsurface oxygen was taken into account for new extensions of the original KEE model [63, 87, 97], so too the overall effect of faceting of the single crystal surface [80].

2.4.5 Pattern formation in the CO oxidation system

After discussing the kinetics, the microscopic mechanism, and a mathematical model for the CO oxidation on Pt(110), as done in the previous sections, the corresponding phenomena of nonlinear kinetics and appearance of spatiotemporal patterns can be better understood. The present section briefly reviews the main milestones in the research on the CO oxidation on platinum single crystal surfaces, and touches upon the more significant self-organized structures.

The group of E. Wicke discovered in 1972 the oscillations of the reaction rate in the catalytic oxidation of carbon monoxide [103]. The desire to explain the origin of this kinetic instabilities set off a burst of activity on the field of oscillatory surface reactions, of which the catalytic CO oxidation on platinum surfaces is one of the most extensively studied examples [59]. Investigations were focused on processes at well-defined single crystal surfaces under low pressure conditions.

In 1982 G. Ertl and co-workers observed for the first time oscillatory kinetics on single crystal surfaces in CO oxidation on Pt(100) [104]. In 1986, oscillations were also reported on Pt(110) [10], where the authors showed a broader range of behavior, including period doubling and deterministic chaos [105]. Subsequently, control techniques like periodic forcing were introduced [106, 107].

In the 1990s, the development of new spatially resolving optical techniques such as PEEM (in greater detail in section 2.4.6.2) [108] meant a significant step forward in spatiotemporal pattern formation research. Furthermore, ellipsomicroscopy for surface imaging (EMSI) and reflection anisotropy microscopy (RAM) [13] made it possible to also perform studies of pattern formation at atmospheric pressures [66, 109]. All these optical techniques resolve spatially images of concentration patterns on a catalytic surface in real time.

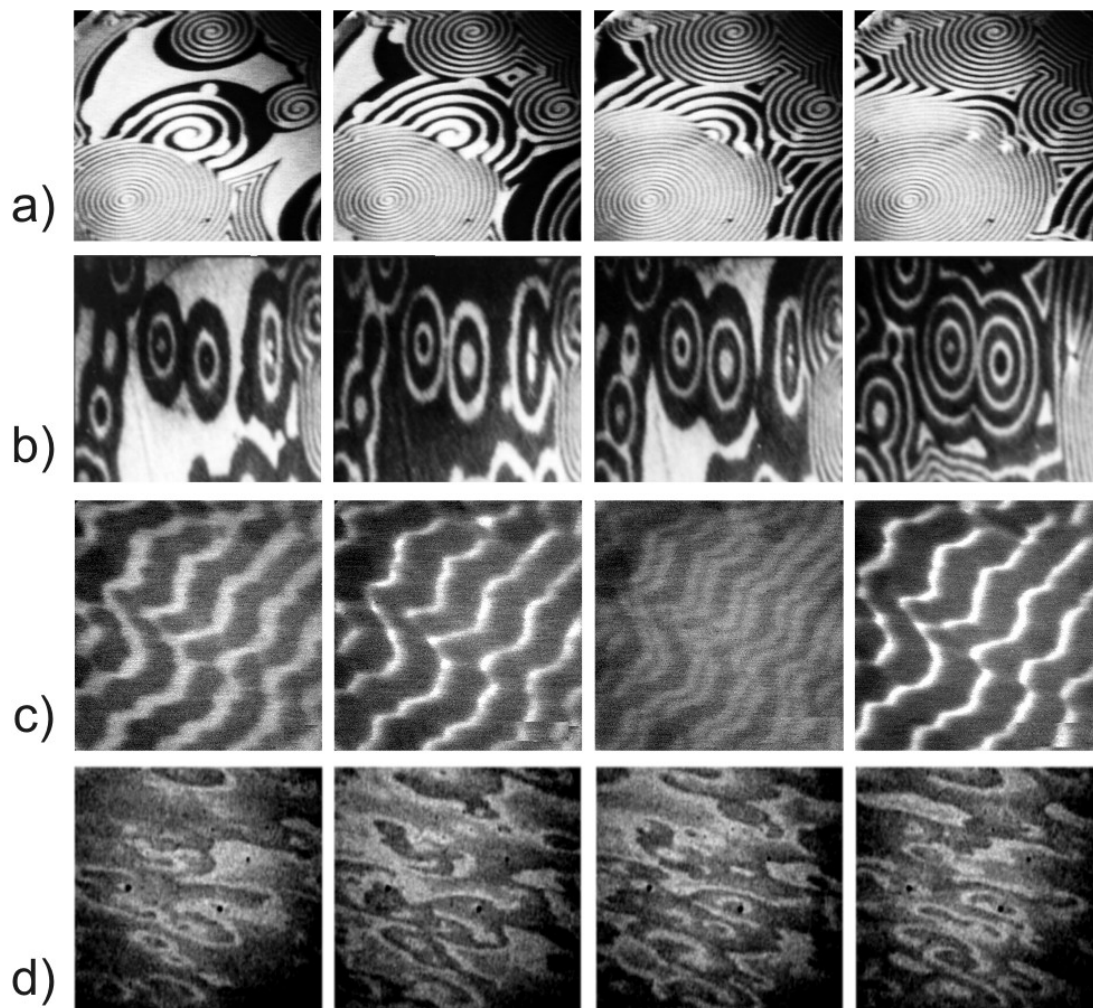


Figure 2.14: Snapshots of PEEM images displaying typical patterns during CO oxidation on Pt(110). Dark areas in the images correspond to predominantly oxygen covered regions, and bright areas indicate mainly CO covered regions. a) rotating spiral waves [101]. The different spatial wavelengths of spirals are due to the existence of different size surface defects to which some of the spirals are pinned. b) target patterns [33], c) standing waves [102], and d) chemical turbulence (taken from experiments corresponding to chapter 3). The size of the crystal area shown is: a) $400 \times 400 \mu\text{m}^2$, b) $200 \times 200 \mu\text{m}^2$, c) $300 \times 200 \mu\text{m}^2$, and d) $300 \times 300 \mu\text{m}^2$.

Proposed by Krischer, Eiswirth, and Ertl, and published in 1992 [80], the KEE model (introduced in section 2.4.4) describes the oscillations and excitable behavior in the CO oxidation reaction on Pt(110). It immediately became a powerful tool for the theoretical assesment of experiments, and has allowed to effectively reproduce the behavior of the system, at least qualitatively.

Among the surface chemical reactions, by far the richest variety of spatiotemporal patterns has been found in CO oxidation on Pt(110). The basic phenomenon underlying these patterns is that of a chemical wave. The latter can be defined as a steep concentration gradient, traveling with constant velocity in space. It was already recognized by Luther in 1906 [110], that chemical waves can arise if an autocatalytic reaction is involved. These chemical waves may appear as simple reaction fronts, or they may form pulses, spirals, target patterns, or even more complex forms including chemical turbulence [33, 34, 59, 101, 111, 112]. Some examples of these patterns are displayed in Fig. 2.14. Similar spatiotemporal structures have also been observed on other substrates, such as Pt(100), Pt(210), and polycrystalline Pt samples, so too for other surface chemical reactions [59].

In later studies efforts were made to guide the processes of self-assembly on the catalyst at will, focused on purposeful global and local modifications to influence the concentration patterns. Global control of parameters, like the modulation of the CO partial pressure, induced new patterns and suppressed chemical turbulence [65, 82, 113]. Local control has been based on the inclusion of microstructures on the catalytic surface [114, 115, 116], on the use of lasers to increase the reactivity in a very localized way, as well as on the combination of both [42, 117]. More information about the state of the research in this field can be found in [118].

2.4.6 Experimental setup

An introduction to the different setups and techniques that were used for the experimental part of this work related with the CO-Pt system follows.

2.4.6.1 Ultra high vacuum system (UHV)

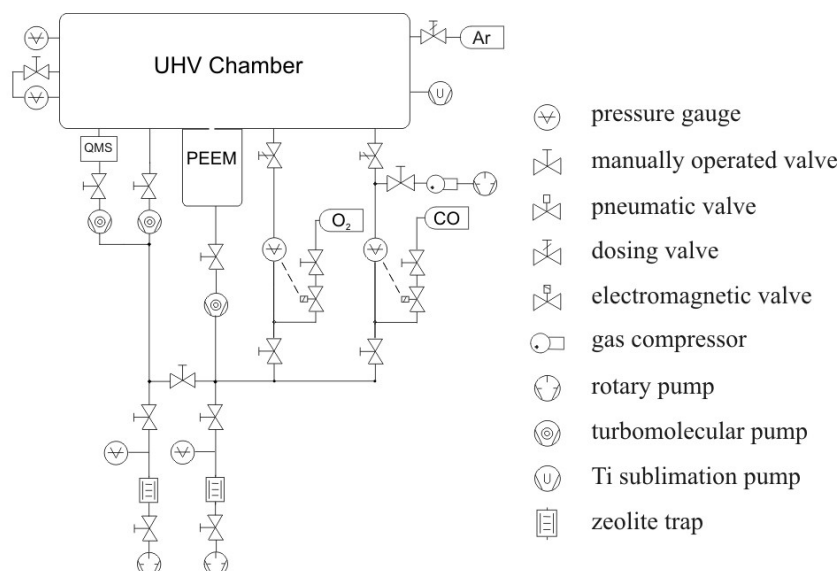


Figure 2.15: Sketch of the UHV chamber including pumping and gas supply system.

The experiments with CO oxidation on Pt(110) presented in this work were performed in a stainless steel ultrahigh vacuum (UHV) chamber, schematically shown in Fig. 2.15. Two rotary vane pumps establish a pre-pressure of 10^{-3} mbar, which is measured with two Pirani gauge. Zeolite traps prevent the lubricating oil of these roughening pumps to contaminate the UHV chamber. The vacuum inside the chamber is maintained by three turbomolecular pumps and a titanium sublimation pump. Combining all of them, the pressure in the 60 liter chamber is kept at a base pressure of 10^{-10} mbar. The pressure inside the UHV chamber is measured with a baratron differential capacitance manometer for low (10^3 - 1 mbar) and medium vacuum (1 - 10^{-3} mbar), and an ionization manometer for high (10^{-3} - 10^{-7} mbar) and ultrahigh vacuum (10^{-7} - 10^{-12} mbar). Leaks and chemical species tests are done with a differentially pumped quadrupole mass spectrometer (QMS).

A PEEM (see below) is set as the main microscopic technique used in chapter 3. In addition, the chamber is equipped with standard UHV surface science instruments such as low-energy electron diffraction (LEED) and Auger electron spectroscopy (AES).

The sample used in chapter 3 is a Pt(110) single crystal, 10 mm in diameter. A sample holder manipulator allows its controlled positioning inside the chamber, and electric stepper motors allow precise movements in the x, y, and the z directions, as well as radial and azimuthal turns. A halogen projector lamp is mounted inside the sample holder for heating the crystal directly from behind. The platinum sample was prepared by repeated cycles of argon ion sputtering, oxygen treatment, and annealing. Purified gases (Ar 5.0, CO 4.7, and O₂ 5.0) were supplied into the chamber by manually operated valves, and were used for the experiments as well as for the sample preparation. Besides that, to ensure stable partial pressures in the chamber, the supply of gases was regulated by means of electromagnetic valves that were automatically controlled by an electronic feedback system. In particular, the CO and oxygen partial pressures could be computer controlled and modified via Labview.

2.4.6.2 Photoemission Electron Microscope (PEEM)

The imaging instrument used in chapter 3 to study the spatiotemporal patterns that arise at CO oxidation on platinum is the PEEM. It allows the direct real-time visualization of adsorbates, and has been used extensively since the early 1990's to study heterogeneous catalysis [33, 34, 108, 119]. PEEM, schematically represented in Fig. 2.16, yields spatially resolved information based on the work function difference between adsorbates across the sample surface. PEEM is a vacuum instrument and can only work at pressures up to 10^{-6} mbar, therefore it is differentially pumped (as can be seen in Fig. 2.15), allowing a maximum pressure of 10^{-3} mbar at the sample.

The emission of photoelectrons from the sample is caused by photons originated from uniform illumination by a 200 W deuterium discharge ultraviolet lamp; the angle of light incidence is ~ 75 degrees to the surface normal. To capture the highest number of emitted photoelectrons, the sample is placed close to the objective (4 mm). The cloud of emitted electrons is accelerated by a 20 kV potential between the sample and the PEEM. A system of three lenses then magnifies the local electron distribution by a factor of $10^2 - 10^3$ by imaging the latter onto a channelplate of 4 cm in diameter [119].

The channelplate intensifies the local electron current by about 10^3 and is converted into a light intensity image by a phosphor screen. This image is recorded by a CCD camera at a rate of 25 frames per second, which means that this instrument has a reasonably good temporal resolution. The imaged areas have a diameter of $500\text{ }\mu\text{m}$ with a spatial resolution of $1\text{ }\mu\text{m}$.

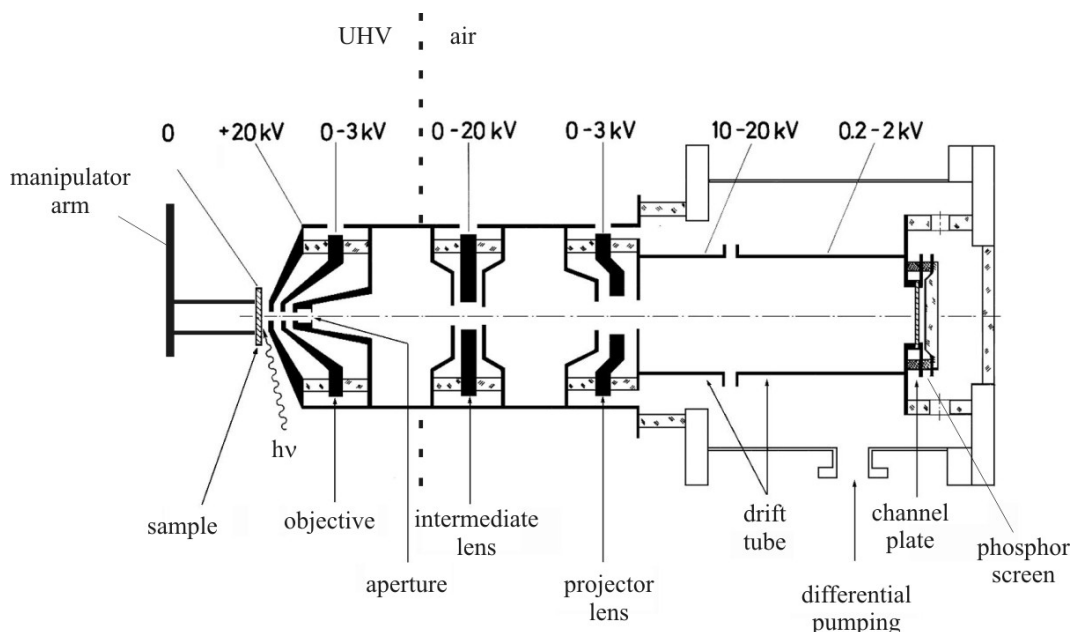


Figure 2.16: Section view of the PEEM [108].

In air, the absorption of oxygen limits the spectrum of the lamp towards high energies at around 6.8 eV, while the Pt electrons work function φ is $\sim 5.8 - 6.0$ eV. The work function of an oxygen covered platinum surface is higher than the clean surface ($\Delta\varphi = +0.8$ eV), causing a decrease in the emitted photoelectron and consequently also a decrease on the PEEM image intensity. The increase of the work function for CO covered areas is less than that of the oxygen covered platinum ($\Delta\varphi = +0.3$ eV) thereby increasing the number of emitted photoelectrons and the brightness of the image. This means that in the present work, dark PEEM images represent oxygen covered while bright ones represent CO covered platinum. Further information about Rotermund's group PEEM can be found in [120].

2.4.6.3 Michelson interferometer

Reaction thermal effects were observed at low pressure when the CO oxidation takes place on an ultrathin platinum substrate [68]: such thin films exhibited heat induced surface expansions. To quantify the latter, surface topography methods based on interferometry patterns turned out to be a suitable tool, and therefore an interferometer is used in chapter 4 to characterize a Pt thin foil during the processes of species adsorption and CO₂ production.

Interferometers are optical tools used for the high-precision measurement of wavelength, distance, index of refraction, and temporal coherence of optical beams. They are based on the superposition of waves with the same frequency and amplitude to detect differences between them, adding to each other when in-phase, and canceling each other out when in opposite phase. Applications are found in a large variety of fields, including astronomy, fiber optics, optical metrology, oceanography, seismology, quantum mechanics and plasma physics [121].

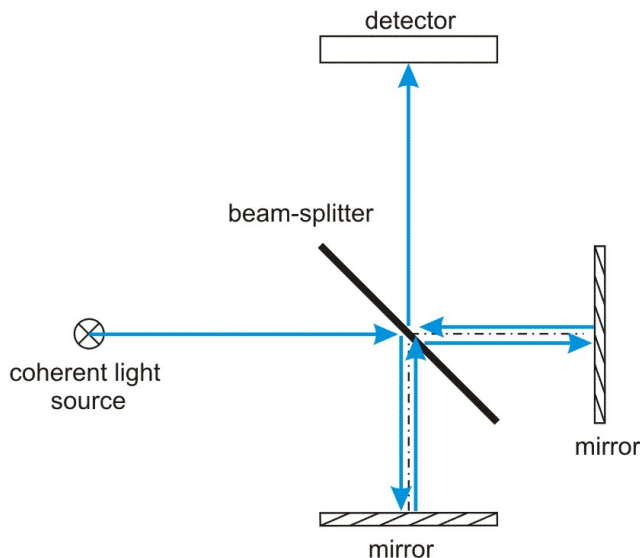


Figure 2.17: Simplified reproduction of a Michelson interferometer [42].

There is a number of known interferometer types, namely the Mach-Zehnder interferometer (used in integrated optical circuits), the Fabry-Perot interferometer (widely

used in telecommunications and spectroscopy), or the Sagnac interferometer (used in navigation) [121]. Besides that, a notable example is the Michelson interferometer, which is used in chapter 4 of this work to measure the temperature induced expansion of a platinum ultra-thin foil.

Albert Abraham Michelson developed the interferometer named after him in 1881, using it in collaboration with his colleague Edward Williams Morley in 1887 in the Michelson-Morley experiment in which this interferometer proved (against their own expectation) the non-existence of luminiferous ether [122]. The Michelson interferometer, schematically depicted in Fig. 2.17 consists of a source of coherent light, a beam splitter (a partially reflective mirror), two mirrors, and a light detector. Interference fringes are produced by splitting a beam of monochromatic light in the beam splitter, so that each beam strikes a mirror. When the reflected beams are brought back together at the detector, an interference pattern is formed based on the different light paths. If these two paths differ by a whole number (including 0) of wavelengths, there is constructive interference and a strong signal at the detector. If they differ by a whole number and a half wavelengths, destructive interference weakens the signal. The path difference may be the result of a relief or bulge on the surface of one of the reflecting mirrors. And that is the case in chapter 4, where a platinum sample plays the role of one of the mirrors, and the interference fringes carry information about the surface profile.

Let's consider one of the mirrors of a Michelson interferometer as fixed and perfectly perpendicular to its incident beam (reference mirror), while the other mirror has an adjustable position:

Mirror perpendicular to its incident laser beam A laser beam would illuminate a small spot, so the interference is hard to see. To spread out the light ray a lens can be placed between the laser and the beam splitter. This spreads out the beam and makes the interference easier to be seen. An interference pattern of dark and bright rings, or fringes, is seen on the viewing screen, as shown in Fig. 2.18 a). However, this spreading also means that only the central ray of the laser beam is still traveling on a straight line through the interferometer. All the surrounding rays are traveling at some angle, depending on how close to the center of the beam they are. Thus rays at different radii from the center of the laser beam travel a different total distance through the interferometer. This causes the interference pattern we see to look like a bullseye or

target shape, with concentric rings of bright and dark fringes. As the distance mirror-beam splitter is changed (d in Fig. 2.18 a)), the maxima and minima of the wave interference alternate, and dark or bright spots in the very center of the fringes can be seen.

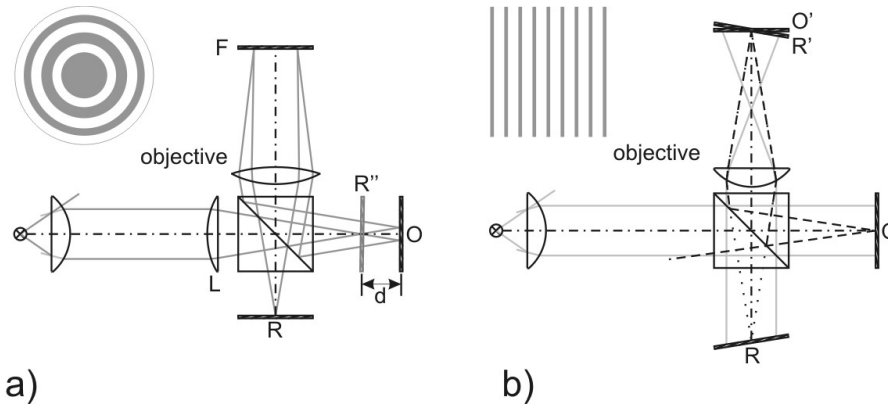


Figure 2.18: Representation of a Michelson interferometer with its corresponding interference pattern reconstructed at the detector. a) shows the two mirrors perpendicular to their incident laser beams. In b) the mirrors are slightly tilted. Reproduced from [42].

Mirror slightly tilted When one of the mirrors is tilted (even tenths of a degree), the maximal peak of interference is shifted out of the viewing screen (Fig. 2.18 b)) and the secondary maxima are imaged as parallel fringes. If in addition, one of the mirrors is not perfectly flat, the interference stripes would appear distorted. This is the kind of pattern that characterizes the topography of a thin Pt foil in chapter 4.

2.5 Pitting corrosion on stainless steel

As mentioned before, a part of the thesis has been focused on the nonlinear aspects of pitting corrosion on stainless steel. The following section will present a brief introduction into the vast field of corrosion.

Metallic corrosion is a physicochemical process which consists of the degradation of a metal exposed to a reactive environment. Pitting corrosion is a sort of localized corrosion of major practical importance [123]; it does not extend over the metal surface but penetrates into its interior, causing this way most of the failures of metallic structures. Pit growth usually starts on chemical impurities, inclusions, or, in the case of extremely pure metals, the vulnerable spots are dislocations and physical defects. While pits grow, the composition of the electrolyte changes locally due to the hydrolysis of metal ions. The aggressiveness of the medium increases close to the dissolution site leading to the acceleration of the corrosion process [124, 125]. This also yields a cooperative bistable behavior, where spreading fronts can be predicted [126] and experimentally observed [15]. That is, pitting corrosion is an autocatalytic process, strongly associated with threshold phenomena [127]. This section provides the electrochemical background in addition to the experimental information that complete chapter 5, where single pits are characterized.

2.5.1 Corrosion mechanism

The evolution of pitting corrosion of stainless steel when in contact with a chloride solution involves three distinct stages: nucleation, metastable growth, and stable growth [128]. Experimental results suggest that pit formation occurs at weak spots of the protective chromium oxide layer: inclusions, defects, scratches, metal dislocations, or areas in contact with an anion concentration (e.g. Cl^- ions) exceeding a critical value [124]. At that vulnerable spot, the electrolyte has direct access to the oxide-free metal surface, and causes the saturated solution of corrosion products within the initial cavity. The aggressiveness of the medium increases in and close to the dissolution site, leading to acceleration of the corrosion process [130]. Besides chlorides, other anions implicated in pitting include fluorides and iodides. Fig. 2.19 depicts the nucleation, growth, possible propagation, and passivation of a pit. Each pit produces a small spike in the electrical

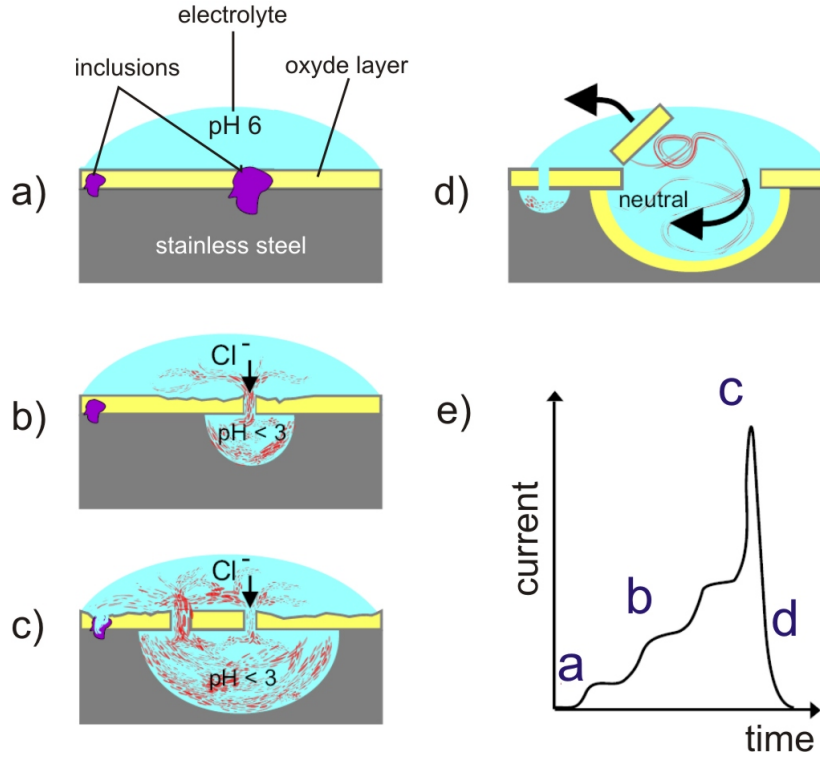
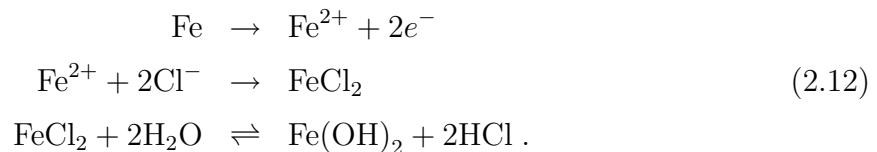


Figure 2.19: Schematic diagram of the pitting corrosion process, following Pastorius and Burstein [128]. b) onset of the corrosion in one of the inclusions shown in a). c) the pit grows while the aggressive anions start a new corrosion process in a close inclusion. d) passivation of the main site as the old surface oxide collapses and a new one forms. e) corresponding current through the metal during a), b), c), and d). Reproduced from [129].

current through the sample, indicating an anodic reaction that dies out in few seconds. Typically, the corrosion reaction implies the oxidation of iron, and the formation of iron hydroxide and hydrochloric acid as follows:



Pit growth is controlled by the material composition, the pit bottom potential, and the relative rate of metal dissolution and of ion transport in the liquid phase [124]. If the electrolyte becomes saturated, salt may precipitate on the pit wall leading to an abrupt cessation of the pit growth process. On the other hand, if the concentration of aggressive anions decreases significantly inside or in the vicinity of a dissolution site, the bare metal surface becomes prone to oxidation, passivating. *Unstable* pitting, involves an intermittent regime of *metastable* growth caused by temporary repassivation of previously active corrosion pits. With a lifetime on the order of seconds, metastable pits can form at potentials below the *pitting potential*, which is associated with the initiation of stable pits [127]. *Stable* pits happen when corrosion lasts indefinitely in time: a delicate balance must be maintained between the metal dissolution and the ion transport towards and away from the active surface. In other words, stable pits survive the metastable stage and continue to grow, whereas metastable pits repassivate and stop growing [127].

Unstable pitting is normally related with vertical and/or horizontal grain attack, and undercutting, while stable pit growth is prone to semispherical shapes (Fig. 2.20). In the pitting formation there is a set of critical potential values found [127]: the pitting potential (ϕ_p) and the repassivation potential (ϕ_r), which is lower than the former. Stable pits form above ϕ_p , and will grow at potentials above ϕ_r .

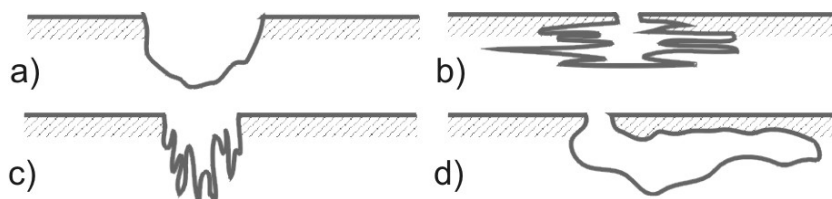


Figure 2.20: Schematic representation of different common pit shape: a) semispherical, b) horizontal grain attack, c) vertical grain attack, and d) undercutting. Reproduced from [131].

2.5.2 Experimental setup

This section offers a schematical introduction into the principles of the surface imaging techniques employed in chapter 5, as well as a description of stainless steel 316 and of the three electrode setup used for the electrolytic corrosion experiments.

2.5.2.1 Stainless steel: AISI 316

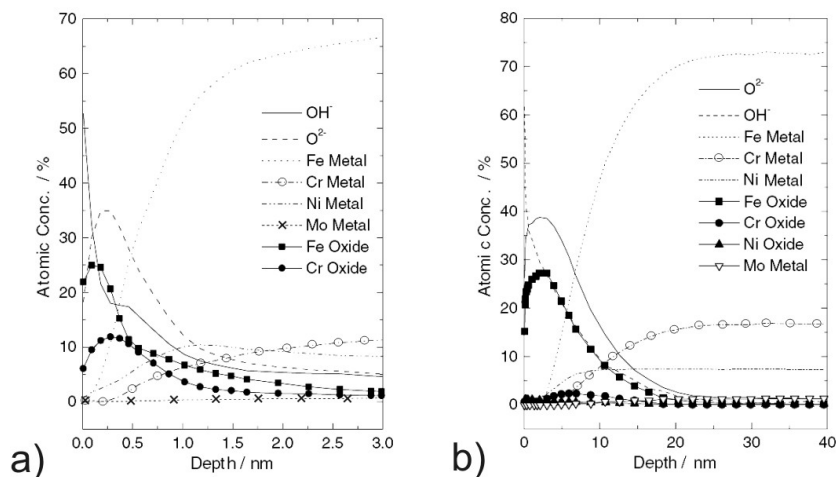


Figure 2.21: XPS depth profiles of the passivation films developed on AISI 316: a) film formed in air, and b) electrochemically formed film after eight potentiodynamic polarization cycles in 0.1 M NaOH solution. Reproduced from [132].

Stainless steels are iron based alloys containing chromium. They achieve their stainless characteristics through the formation of an invisible and adherent chromium rich oxide film: the chromium forms a passivation layer of chromium(III) oxide (Cr_2O_3) when exposed to oxygen; Fig. 2.21 shows in detail the composition of the passivation layer formed in air and in a NaOH solution [132]. As the passivation film requires oxygen to repair itself, stainless steels have poor corrosion resistance in low-oxygen and poor circulation environments (e.g. tunneled cavities). AISI 316 is a general purpose variety of commercial stainless steel (the second most common grade after 304). It belongs to

the group of the austenitic steels because it has a high nickel and chromium contents, which provide a superior level of corrosion resistance. This category is also known for its ductility and weldability as well as for its ability to withstand extremely low temperatures. 316 steel is used in the manufacture and handling of food and pharmaceutical products where it is often required in order to minimize metallic contamination. SS316 is also frequently found in nuclear reprocessing plants. Often referred to as “A4” in accordance with the International Organization for Standardization ISO 3506, its typical composition is 0.13 % C, 0.31 % Co, 18.18 % Cr, 0.38 % Cu, 1.75 % Mn, 2.40 % Mo, 12.25 % Ni, 0.016 % S, 0.35 % Si, and 64.23 % Fe (based on [14]).

2.5.2.2 Three electrode setup

The study of surface corrosion processes presented in the present work was performed using an electrolytic cell, where a chemical reaction is purposefully driven by an external supply of voltage (accelerated corrosion). An electrochemical cell can be made using a three electrode configuration, including working, counter, and reference electrodes (as seen in Fig. 2.22).

The aim is to control the potential drop across the interface at the surface of the *working electrode* (i.e., the stainless steel interfacial potential) while the pitting corrosion takes place. The electrode-solution interface is thought of as a sheet with positive or negative charge (the surface of the electrode) in contact with a sheet of the opposite charge next to it (the solution) that is called the *electrical double layer*. To control or to measure the interfacial potential between working electrode and solution, at least one more electrode is needed: the *counter electrode*. The interfacial potential of the counter electrode in a two electrode system does not remain constant, but varies as the current passes through the cell, and therefore the potential at the stainless steel cannot be independently measured. This problem is overcome by using a third electrode, the so called *reference electrode*. This ensures that the potential between the working and the reference electrodes is controlled. The current passing through the reference electrode can be further diminished by using a high-input-impedance operational amplifier for the reference electrode input.

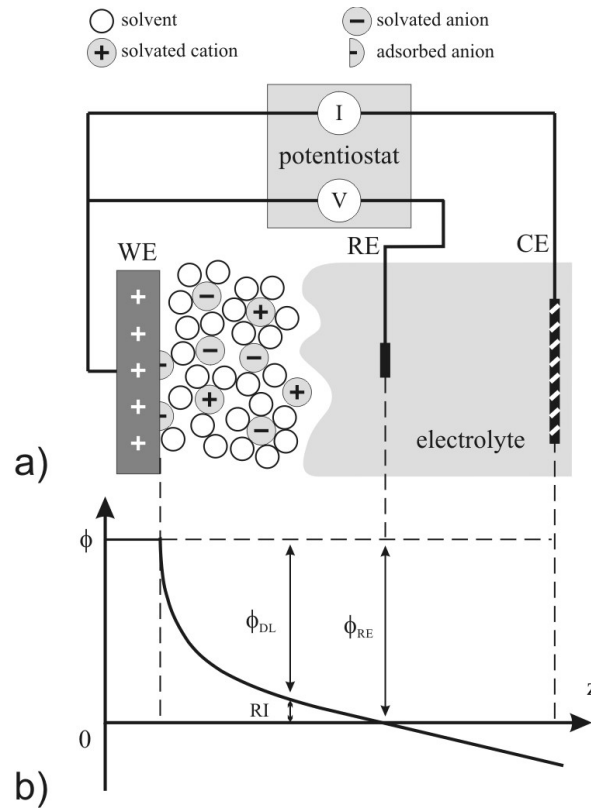


Figure 2.22: a) schematics of a three electrode cell: working electrode (WE), reference electrode (RE), and counter electrode (CE). b) the corresponding voltage drop across the system. R represents the electrolyte resistance, I the current measured, V the externally applied voltage, ϕ_{DL} the interfacial potential (DL stands for double layer), and ϕ_{RE} the WE-RE potential. Reproduced from [129].

2.5.2.3 Scanning Electron Microscopy (SEM) and Atomic Force Microscopy (AFM)

To gain high resolution information about created pits two scanning microscopies have been used, namely the SEM and the AFM; both will be discussed now.

SEM The earliest known work describing the concept of a SEM was published by M. Knoll (1935) [133] who, along with other pioneers in the field of electron optics, was working in Germany. Subsequently M. von Ardenne (1938) constructed a scanning transmission electron microscope (STEM) by adding scan coils to a transmission electron microscope. The instrument was further developed by Charles Oatley and first commercialized by Cambridge Instruments [134].

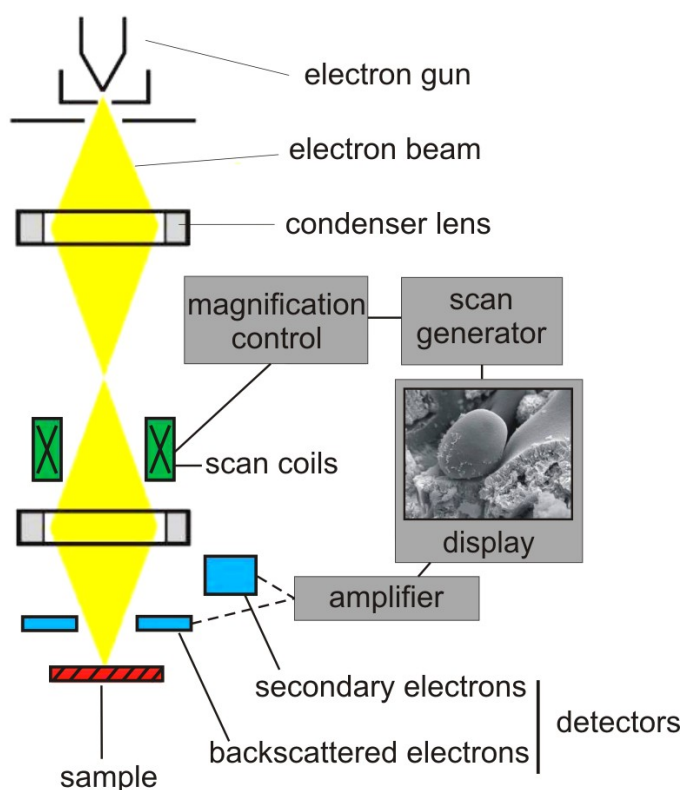


Figure 2.23: Sketch of a SEM.

Images in a SEM are generated by focusing a beam of high energy electrons onto the surface of a sample and detecting signals from the interaction of the incident electrons with the sample's surface (Fig. 2.23) [134, 135]. The gathered signals may be secondary electrons, back scattered electrons, and characteristic x-rays. In a SEM these signals come not only from the primary beam impinging upon the sample, but from other interactions within the sample near the surface. The SEM can operate with a resolution of 1 - 20 nm [135]. SEM images have great field depth that yields a characteristic three-

dimensional appearance that is very suggestive of a relief perspective, extremely helpful for understanding the surface structure of a sample.

AFM In 1986, Binnig, Quate, and Gerber first reported the invention of the AFM in their highly cited article [136]. Its precursor, the scanning tunneling microscope (STM) was developed in the early 1980s by Binnig and Rohrer [137]. AFM operates by measuring attractive or repulsive forces between a tip and the sample. The tip, generally monolithic silicon 15 - 20 μm height with a radius of curvature < 10 nm, is positioned at the end of a cantilever beam shaped much like a diving board. As the tip is repelled by or attracted to the surface, the cantilever beam deflects. Typically, the amplitude and phase of the deflection is measured using a laser spot reflected from the top of the cantilever into an array of photodiodes (Fig. 5.4). A plot of the laser deflection versus tip position on the sample surface provides the resolution of the hills and valleys that constitute the topography of the surface.

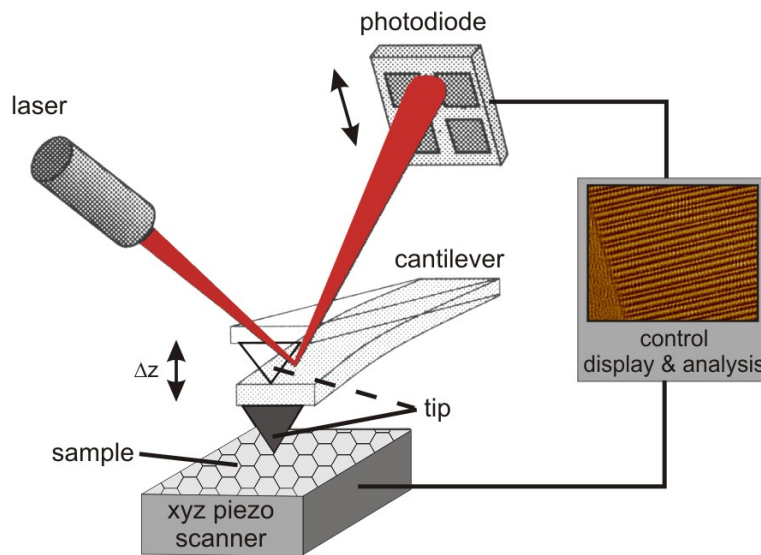


Figure 2.24: Sketch of an AFM.

One of the most common AFM operation modes is the *tapping mode*, involved in the pitting corrosion analysis of this work. The cantilever is made to oscillate with a piezo-element with a high amplitude (typically greater than 20 nm) when the tip is not in contact with the surface. The oscillating tip is then moved towards the surface until it begins to tap the surface lightly. During scanning, the vertically oscillating tip alternately contacts the surface and lifts off, generally at a frequency of 50,000 to 500,000 cycles per second. As the oscillating cantilever begins to intermittently contact the surface, its oscillation is necessarily reduced due to energy loss caused by the tip contacting the surface. The reduction in oscillation amplitude is used to identify and measure surface features, as good as atomic resolution. This technique can be used with samples in air or in a fluid, allowing *in situ* electrochemical experiments (as presented in chapter 5).

Chapter 3

Global control on the catalytic CO oxidation on Pt(110)

The knowledge of an extended system opens doors to the control of its dynamics, and the control of its dynamics can be used to test and support prediction models. The present chapter deals with control techniques applied to reaction-diffusion systems, mainly aiming at suppressing chemical turbulence. In particular, techniques for purposeful global modifications of the reaction parameters of the catalytic CO oxidation on Pt(110) are detailed. This chapter is divided into two large sections, each of them corresponding to a different global control technique:

- Resonant forcing
- Effect of noise

Both are based on CO partial pressure modulation in the reaction chamber (schematically shown in Fig. 3.1). The special experimental techniques and implementations for each section are described. The arising spatiotemporal patterns are observed with PEEM, analyzed, compared with numerical results, and discussed.

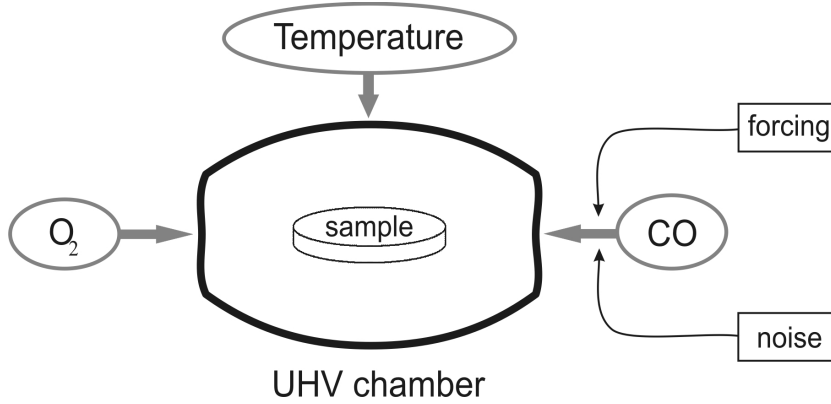


Figure 3.1: Experimental setup with external forcing and noise.

3.1 Resonant forcing

Periodic forcing can be understood as a global control technique, and it is a common phenomenon in nature too. It plays an important role in any system with a certain time regularity, for instance plankton production, the human heartbeat, tidal currents, pollution models, or circadian rhythm [106, 138, 139, 140]. Periodic forcing has attracted considerable interest in the last decades both in theory and practice [141, 142]. This section presents the particular case of spatially uniform resonant periodic forcing of the CO-Pt system. A preliminary approach precedes the setup implementations. Then, the experimental results for different forcing regimes are presented and commented on.

3.1.1 Preliminary approach

3.1.1.1 Single nonlinear oscillators

The temporal response of a single oscillator to a small stimulus (known as forcing), if periodic in time, can be either quasiperiodic (unlocked) or periodic (locked), depending upon the magnitude of two external determining parameters of that stimulus: the forcing amplitude γ and the forcing frequency ν_f [143]. In the frequency-locked state, the system may oscillate with a frequency different from its natural frequency ν , where the range

of detuning $\nu - \nu_0$ over which frequency locking can be observed expands for increasing forcing amplitude γ . This is reflected by tongue-shaped regions of resonance in the frequency-amplitude plane. Within these so-called Arnold tongues, the frequency of the forced oscillator is correlated by a definite mathematical relation with the frequency of the external force, $\nu_f/\nu = n/m$, where the general case of an $n:m$ resonance is denoted as sub-harmonic (super-harmonic) if $n > m$ ($n < m$). An example of such Arnold tongues is shown in Fig. 3.8 and will be discussed in section 3.1.3.

Periodic forcing and entrainment of single oscillators are both well understood, and have been investigated in the context of many different systems [144]. Ordinary differential equation models [145] and experimental approaches [146] have been used to study one-dimensional maps [147]. However, much less is known about the effect of a time-periodic stimulus on spatially extended oscillatory systems [143].

3.1.1.2 Extended systems of oscillators

The response of a spatially extended system of oscillators to periodic parameter modulation is more complicated than that of a single oscillator: the oscillation at different points in the continuum can vary in amplitude and phase. Besides frequency-locked uniform oscillations, the variation of frequency and amplitude of the external force can lead to a multiplicity of complex spatiotemporal phenomena in such systems. More specifically, the system can respond in such a way that the ratio of the frequency of the resulting oscillation to that of the perturbation (ν/ν_f) is a rational number (*entrainment*). It can also yield to a quasiperiodic, or even a chaotic behavior. In the particular case of $n:m$ resonance, different parts of the system can be locked to any of the n distinct phase states, and fronts will be observed that separate these different phase locked states.

An important group of oscillators extended system in which these phenomena can be investigated experimentally are chemical reaction-diffusion systems with oscillatory kinetics. Previous studies were mostly carried out using the periodically forced light-sensitive Belousov-Zhabotinsky (BZ) reaction [145]. Resonant pattern formation in this system has been systematically investigated as a function of the forcing parameters ν_f and γ [143, 148, 149]. A variety of space-time patterns could be stabilized, and detailed studies of resonant phase clusters [150] and front instabilities were performed [151].

In recent years, a number of heterogeneous catalytic reactions were established as model systems for the study of self-organization in nonlinear reaction-diffusion systems [59]. These are chemical reactions with high industrial relevance. When observed on well-defined single crystal surfaces, these systems are truly two-dimensional and individual reaction steps can be analyzed with surface science diagnostics under ultrahigh vacuum conditions. Thus, contrary to homogeneously catalyzed reactions in aqueous phase, their mechanisms are often simple and well understood. The oxidation of CO on Pt(110) under low-pressure condition was found to exhibit stable periodic oscillations of the CO₂ formation rate for particular conditions of partial pressures and temperature; since then, the CO-Pt system has been repeatedly used for the study of periodic forcing of a self-oscillating surface reaction [106].

By contrast to chaotic oscillators, the local oscillations in the CO oxidation extended system are prevalently periodic, disturbed only by the diffusive coupling between neighboring surface sites (as explained in chapter 2). The transition from homogeneous oscillations with a defined natural frequency to disordered turbulent patterns is smooth, and results in both a broadening and a small shift of the dominating frequency line.

3.1.1.3 The natural frequency of the system

The intrinsic or natural frequency of the CO-Pt system (ν_0) can be defined as the main frequency in the Fourier spectrum of the local PEEM image intensity. In other words, the frequency with the highest amplitude in the power spectrum of a local intensity time series. For a measurement of the natural frequency during the experiments, a section of the PEEM image with a size of 10×10 pixels is chosen, its mean intensity is calculated, and its time series Fourier transformed (Fig. 3.2 a) and b)); ν_0 is then determined from the maximum in the power spectrum. Even though the frequency analysis is performed locally, it is assumed to be valid for the whole sample. To check the correctness of this assumption, 2500 pixels, equally distributed over the region of interest (ROI, as seen in Fig. 3.3 b)), were chosen from the same experimental video sequence. The time series of one single pixel is shown in Fig. 3.2 c). For each pixel, a Fast Fourier Transform (FFT) of the time series was computed. Fig. 3.2 d) shows the result for a random pixel. Although the data are much noisier than in the spatially averaged analysis, the main frequency is the same as in Fig. 3.2 b).

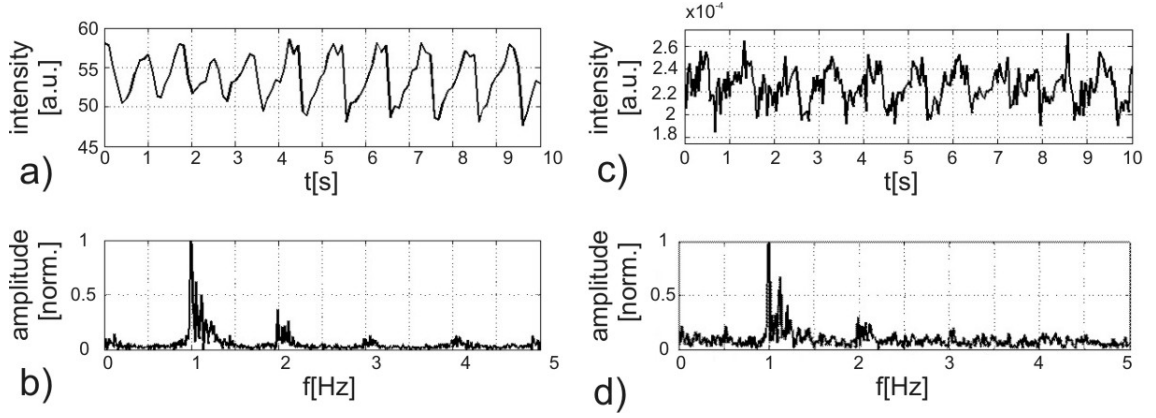


Figure 3.2: a) time series of the averaged image intensity in an area of 10×10 pixels, and b) power spectrum of the data. c) time series of the image intensity one single pixel, and d) corresponding power spectrum. The 1 Hz oscillations are clearly discernable in both the time series and the spectrum. The reaction parameters are $T = 515$ K, $p_{\text{oxygen}} = 1.5 \cdot 10^{-4}$ mbar, $p_{CO}^0 = 7.5 \cdot 10^{-5}$ mbar [113].

The system frequency mainly depends on the crystal temperature and the partial pressures of the reactants. However, on a time range of several minutes the natural frequency slowly decreases although the reaction parameters are kept constant (Fig. 3.3 a)). This effect is presumably caused by a faceting of the platinum surface, which is known to take place in the reaction conditions frame of this work [152]. This assumption is substantiated by LEED pictures taken before and after the experiments, showing a broadening of the diffraction spots after the experiments (data not shown).

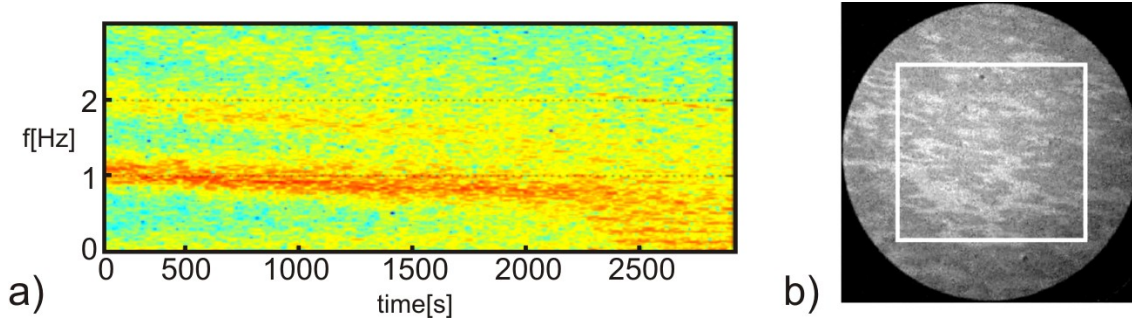


Figure 3.3: a) Fourier spectrogram showing the time evolution of the natural frequency of the system without forcing. For the analysis of each PEEM frame a window of 20.48 s (512 samples at 25 frames per second) is chosen. Initially, the frequency has a value of ≈ 1 Hz. During the first 30 minutes it drops by approximately 0.2 Hz. Also a broadening of the frequency line is observed, which indicates an increase in turbulence in the system. Temperature ($T = 515$ K), and partial pressures ($p_{\text{oxygen}} = 1.1 \times 10^{-4}$ mbar, $p_{\text{CO}} = 9.1 \times 10^{-5}$ mbar) were constant. b) PEEM image of the Pt(110) surface under reaction conditions without forcing. The region of interest (ROI), used for a global test of the Fourier method for determination of the natural frequency, is indicated by the square. Within the ROI 50×50 pixels were analyzed. The reaction parameters are $T = 515$ K, $p_{\text{oxygen}} = 1.5 \times 10^{-4}$ mbar, $p_{\text{CO}}^0 = 7.5 \times 10^{-5}$ mbar [113].

3.1.2 Experimental implementation

This section details how the experimental setup introduced in section 2.4.6 was used to externally force the oscillatory CO oxidation in a periodic way. Previous experimental efforts to study pattern formation of the driven CO oxidation were not focused on resonant frequencies, and they were more restricted in forcing speed (below twice the natural frequency of the system). The amplitude of partial pressure modulation in the reactor was limited by the finite pumping speed of the vacuum chamber [153]. In the present work, the frequency of the natural oscillations was carefully analyzed before every experiment. On the other hand, a new experimental setup is introduced to impose higher forcing frequencies to the CO oxidation reaction, while providing at the same time the means to image the spatiotemporal concentration patterns on the catalyst surface by PEEM. The resulting images were taken by a Sony CCD camera. The experimental parameters and the mean intensity of a 10 x 10 pixel region of the PEEM image were recorded with a computer at a sampling rate of 10 Hz.

All experiments (except those concerning a propagating pulse in section 3.1.6, where lower reactivity is needed) were performed within the following parameter range: temperature = 512 - 529 K, oxygen partial pressure $p_{O_2} = 1.0 - 1.5 \times 10^{-4}$ mbar, and carbon monoxide base pressure $p_{CO} = 7.2 - 9.3 \times 10^{-5}$ mbar. Under these conditions, the chemical reaction-diffusion system shows oscillatory behavior with a natural frequency of approximately $\nu_0 \approx 1$ Hz. For resonant forcing, the carbon monoxide pressure in the chamber was periodically modulated following the relation:

$$p_{CO}(t) = p_{CO}^0 [1 + \gamma \sin(2\pi \cdot \nu_f \cdot t)], \quad (3.1)$$

where γ is the forcing amplitude and $\nu_f \approx n \cdot \nu_0$ ($n \in N$) the forcing frequency. Temperature and p_{oxygen} were held constant during the experiment. The general procedure for all experiments was as follows:

- Preparation of the sample by Ar-ion sputtering and subsequent annealing at 950 K.
- Rough manual adjustment of T, p_{oxygen} and p_{CO} to reach a bistable, oscillatory, or excitable regime, monitored with PEEM.
- Manual fine tuning of the parameters until the uniform oscillations become spatially unstable and show turbulent behavior (except in section 3.21, where the aimed

pattern is a propagating pulse). The parameter changes are in the range of a degree for the temperature, and 10^{-5} mbar for the partial pressures.

- Measurement of the system's natural frequency (see section 3.1.1.3).
- Application of harmonic modulation of p_{CO} and measurement of the system response by means of the PEEM images.

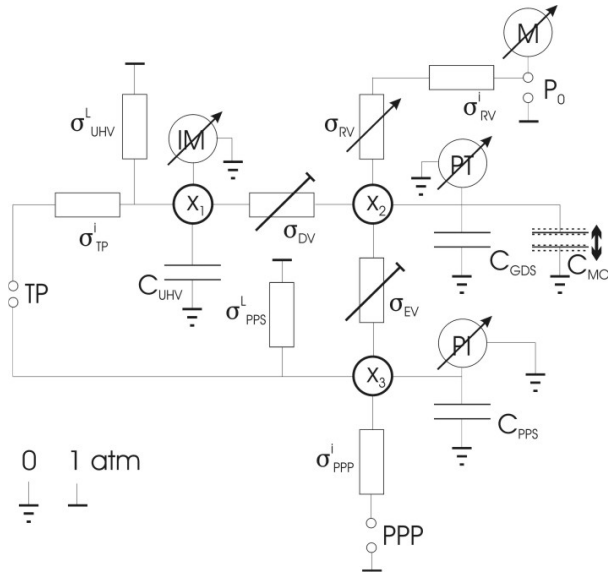


Figure 3.4: The CO pressure regulating system represented as an electric circuit. Symbols, abbreviations, and indices: σ = conductivity, C = capacity, x_1 = pressure in the UHV-chamber, x_2 = regulated CO pressure in the gas dosing system, x_3 = pressure in the pre-pressure system, DV = dosing valve, EV = exhaust valve, GDS = gas dosing system, i = inner, IM = ionization manometer, L = leakage, M = manometer, MOT = compressor, P_0 = pressure after manometer, PPP = pre-pressure pump, PPS = pre-pressure system, PI = Pirani pressure sensor, PT = pressure transducer, RV = regulating valve, TP = turbo pump, UHV = ultra high vacuum [113].

The forcing at frequencies $\nu_f \leq 2$ Hz was applied by controlling the CO flux with an electronic solenoid valve. The valve is connected to a computer and is regulated by an oscillating voltage signal generated by LabView. This setup allows for scanning a

predefined range of forcing amplitudes and frequencies to measure the system's response over a wide parameter range.

However, this setup fails for higher forcing frequencies because the forcing amplitude is strongly damped once the gas flux is dosed into the UHV chamber. Based on the analogy between electrical and pneumatic circuits [154] the UHV-chamber and the CO pressure regulating system were analyzed in detail. Even though this analogy neglects effects of chemical processes and the finite velocity of the gas stream, it reveals the intrinsic low-pass filtering characteristics of the system as can be inferred from the equivalent circuit diagram (Fig. 3.21).

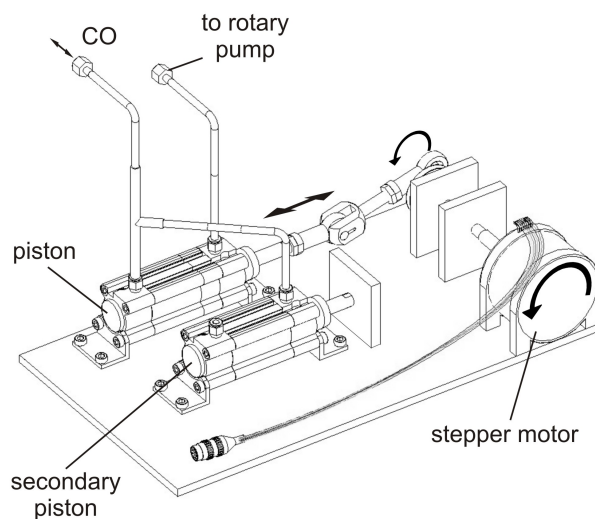


Figure 3.5: Scheme of the forcing compressor [113].

To overcome these experimental restrictions, a novel gas-regulating device was developed and implemented into the system to substitute the electronic valve. The core of the new device is a plunger, connected to the CO prepressure line with a branch connection (see Fig. 3.5). By periodically moving the main piston to and fro in the cylinder with the help of a stepper motor, the gas line volume is changed accordingly, resulting in a harmonic modulation of the CO pressure. The amplitude depends on the ratio between the plunger volume and the installed gas line volume, and can be regulated in a wide range by utilizing a secondary cylinder as an adjustable offset gas volume in the

dosing line. The forcing frequency is adjusted by the rotational frequency of the stepper motor driving the piston compressor. The other side of the piston is pumped by a rotary pump to ease the movement of the piston, since the CO pressure is normally operated between 50 - 100 mbar.

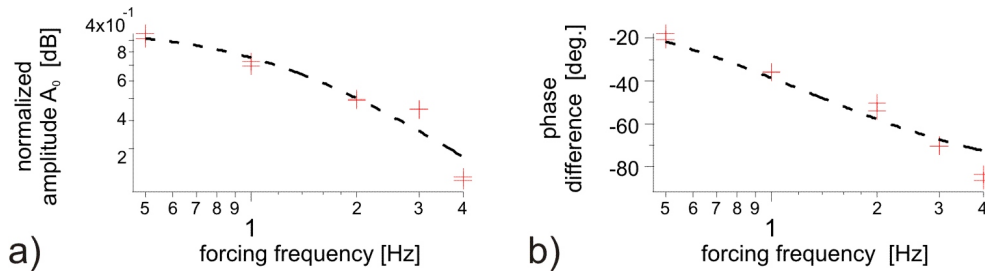


Figure 3.6: Characteristic Bode plots of the UHV-chamber showing the compressor forcing frequency vs. phase and amplitude of resulting oscillations inside the UHV-chamber. The experimental results are shown as crosses, while the dashed lines indicate approximation fits with a first order low-pass filter function [113].

This new device allowed us to apply periodic forcing at frequencies up to 4 Hz and well defined amplitudes. We have analyzed the frequency response inside the UHV-chamber to the generated pressure changes in the prepressure line and present the results in form of a Bode plot in Fig. 3.6. The measurement was performed at $p_{CO} = 2 \times 10^{-4}$ mbar using an ionization manometer (Leybold IM510 with VIG17-head) in linear scaling. The compressor turned out to be more efficient if connected to the gas line as close to the chamber as possible. The oscillation amplitude in the gas dosing system was around 20 %. At a frequency of 2 Hz, the effective pressure variation in the UHV chamber was estimated to be 10 %. This high value could only be achieved under optimal forcing conditions; the forcing strength is reduced by about one order of magnitude for less favorable conditions.

3.1.3 2:1 Resonant forcing

In this section, the experiments performed applying a resonant forcing to the CO oxidation system with values of ν_f close to $2\nu_0$ are presented. At sufficiently large forcing amplitudes the periodic forcing results in an entrained state in which the oscillation frequencies of the system and the forcing signal maintain a fixed ratio $m : n$ (m and n are natural numbers). An initial turbulent state is common to every experiment to follow in this section, which is set by adjusting the reaction temperature and the gases partial pressures.

First, a range of forcing frequencies close above $2\nu_0$ were scanned, while applying different γ values between 0 % and 0.36 % (Fig. 3.7). The corresponding frequency analysis reveals that for low frequency mismatch (detuning $(\nu_f/2) - \nu_0$), $\gamma = 0.06$ % is sufficient to entrain the system, while at larger frequency mismatch entrainment occurred only at $\gamma > 0.18$ %. In the measurement shown in Fig. 3.7, the system is 2:1 entrained, since it oscillates predominantly at a frequency close to half of the frequency of the external force, $\nu_f/2$. At larger mismatch, a period doubling occurs as can be seen from the appearance of sub-harmonic frequencies around $t = 5000$ s. This is in agreement with theoretical results obtained by Davidsen *et al.* [155] who also found a period doubling scenario in the corresponding Arnold tongue (Fig. 3.8).

A complementary experiment allows for a closer view of how the system oscillations transit from its natural frequency to a completely entrained regime. In this case, not a broad range of forcing frequencies was scanned, but only $2\nu_0$. In order not to induce abrupt changes in the oscillatory dynamics of the surface, the forcing amplitude was slowly increased in smaller $\Delta\gamma$ steps, until the system was completely locked to the driving force (at $\gamma = 0.7$ %). The resulting Fourier spectrogram (Fig. 3.9) shows how the main frequency bifurcates twice while gradually approaching the 2:1 locked state.

A third experiment also begins with the forcing frequency manually adjusted to $2\nu_0$. At this setting a forcing strength of 0.04 % was sufficient to suppress turbulent dynamics at least temporarily; intermittent turbulent regimes alternated with spatially coordinated patterns. An increase of the forcing strength resulted in shorter turbulent regimes. At $\gamma = 0.22$ % a phase locked regime with stable cluster patterns 2:1 entrained was observed (Fig. 3.10). The surface splits into large domains belonging to either of the two different phase-locked states. In this way, the population of oscillators was divided

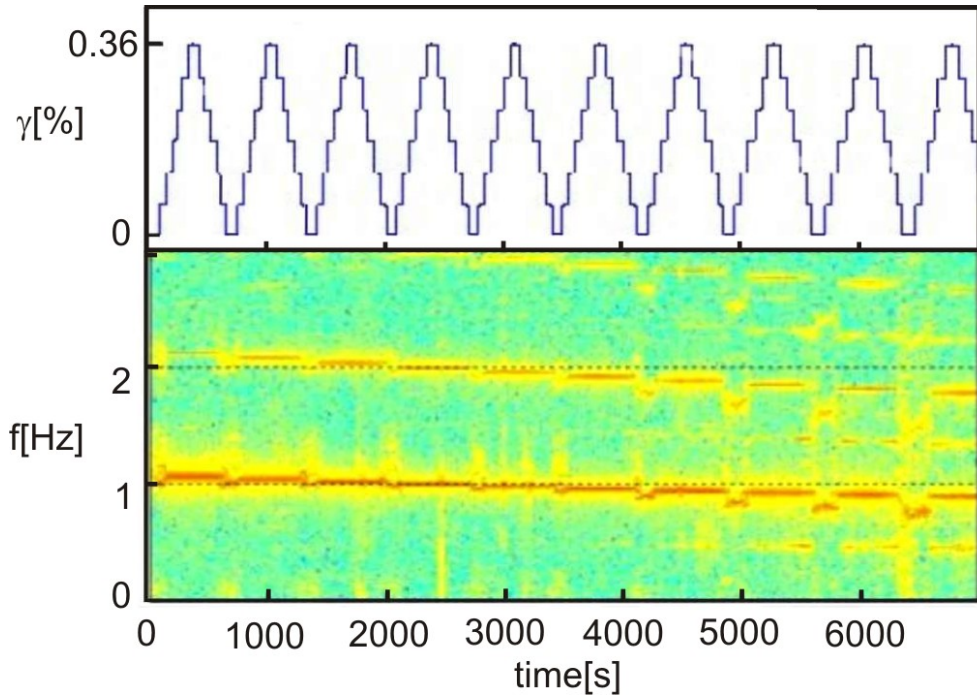


Figure 3.7: Fourier spectrogram showing 2:1 forcing with 2:1 entrainment for sufficiently high forcing amplitudes. Top: forcing amplitude as a function of time. Bottom: corresponding Fourier spectra from 20.48 s intervals. The forcing amplitude is increased in six steps to 0.36 % of the CO base pressure and then decreased in the same manner to zero again. In each of these amplitude sweeps a lower forcing frequency is used. The first sweep ($t = 0 - 750$ s) is performed at 2.12 Hz, the last proceeds at 1.92 Hz. During the experiment, the natural frequency decreases from around 1 - 0.8 Hz. The reaction parameters are $T = 512$ K, $p_{\text{oxygen}} = 1.5 \times 10^{-4}$ mbar, $p_{\text{CO}}^0 = 7.2 \times 10^{-5}$ mbar, and $\nu_0 \approx 1$ Hz [113].

into smaller subpopulations; all of them characterized by the same oscillation amplitude and frequency, but in different phases.

The arising spatiotemporal patterns exhibit a periodicity of four forcing cycles, which indicates that the system performs period doubled 2:1 entrained oscillations; this becomes particularly clear upon following, for instance, the brighter patches shown in the Fig. 3.10 b). The size of these phase domains is not fixed but changes in time, un-

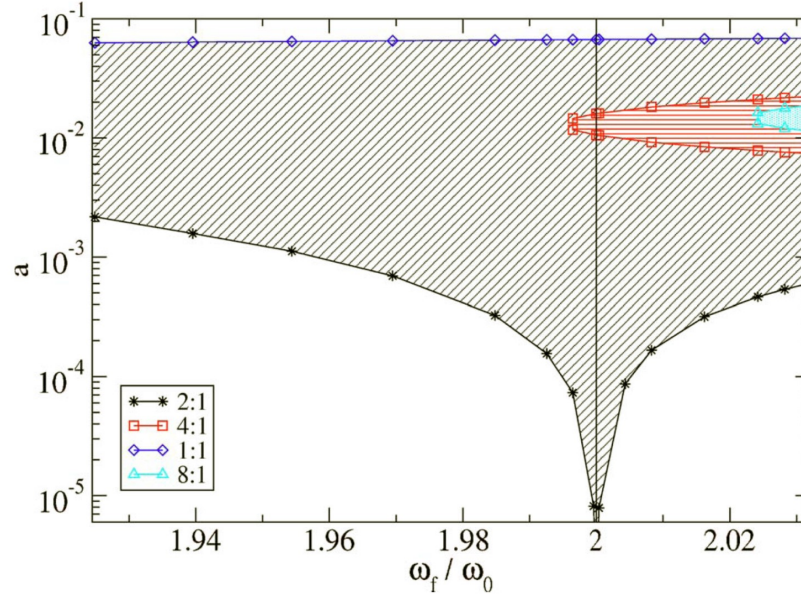


Figure 3.8: The 2:1 Arnold tongue obtained from numerical simulations with the KEE model [80]. The amplitude (a) of the forced oscillation is plotted as a function of the forcing frequency (normalized to the natural frequency of the system). A period-doubling cascade appears in a region below the overlapping 1:1 tongue. For $\nu_f/\nu_0 = 2$ only the first period doubling bifurcation is present. Its location matches that observed for a spatially extended system. Reproduced from [155].

dergoing enlargement-reduction (breathing-like) cycles. The species diffusion dynamics can explain the nature of these oscillations. CO diffuses from high to low concentration regions, which happens in CO-covered domains, enlarging the cluster area. After a forcing cycle the concentration locations are inverted and diffusion proceeds in the opposite direction. This “breathing” mode can be seen in Fig. 3.12, standing out the fact that the larger domain state always corresponds to the (1×1) surface structure. Although the front diffusive behavior changes direction every forcing cycle, the periodicity (with regard to the xt -pattern) is four forcing cycles. Similar front dynamics are found in other oscillatory bistable systems like the BZ reaction [149].

The temporal dynamics of each individual image pixel can be separated into phase and amplitude dynamics using a frequency demodulation technique. This is done by

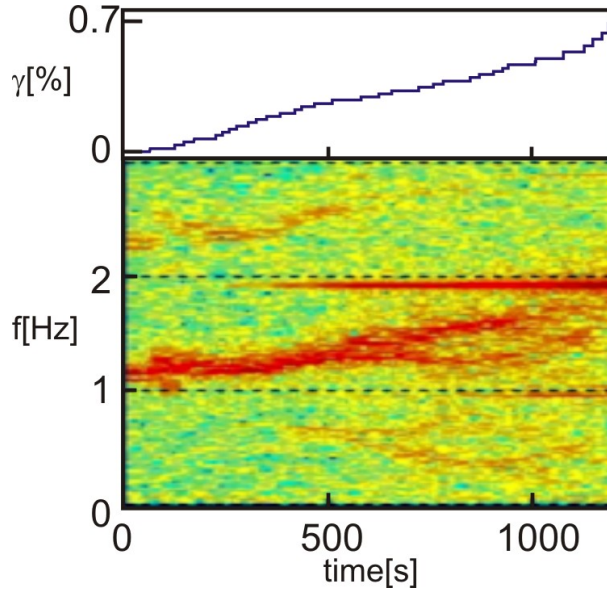


Figure 3.9: Fourier spectrogram showing 2:1 forcing with an increasing forcing amplitude from 0 to 0.7 % of p_{CO}^0 at $\nu_f = 2$ Hz. The reaction parameters are $T = 512$ K, $p_{oxygen} = 1.4 \times 10^{-4}$ mbar, $p_{CO}^0 = 5.9 \times 10^{-5}$ mbar, and $\nu_0 \approx 1$ Hz.

Fourier transformation and evaluation of the complex Fourier coefficients at $\nu_0/2$ within shifted time intervals of 5 seconds duration. In polar coordinates these Fourier coefficients directly give the phase and amplitude of the dominant mode of the local oscillations. The image pixels can now be colored in correspondence their respective phase and amplitude. The result is shown in Fig. 3.11 a) and b). Two different surface regions with opposite phase but identical amplitude can be clearly distinguished. A phase portrait of the system is obtained by plotting the phase and amplitude values of all image pixels in polar coordinates (Fig. 3.11 c)). In addition, a phase histogram was calculated (Fig. 3.11 d)). Two different clusters with a phase difference of π can be seen, while the link between them, corresponding to the bordering area where the oscillations have smaller amplitude, is close to the origin in the phase portrait. The existence of two stable entrained states differing by a phase shift of π is a feature of the 2:1 resonance regime, distinguishing it from that of 1:1 resonance [156].

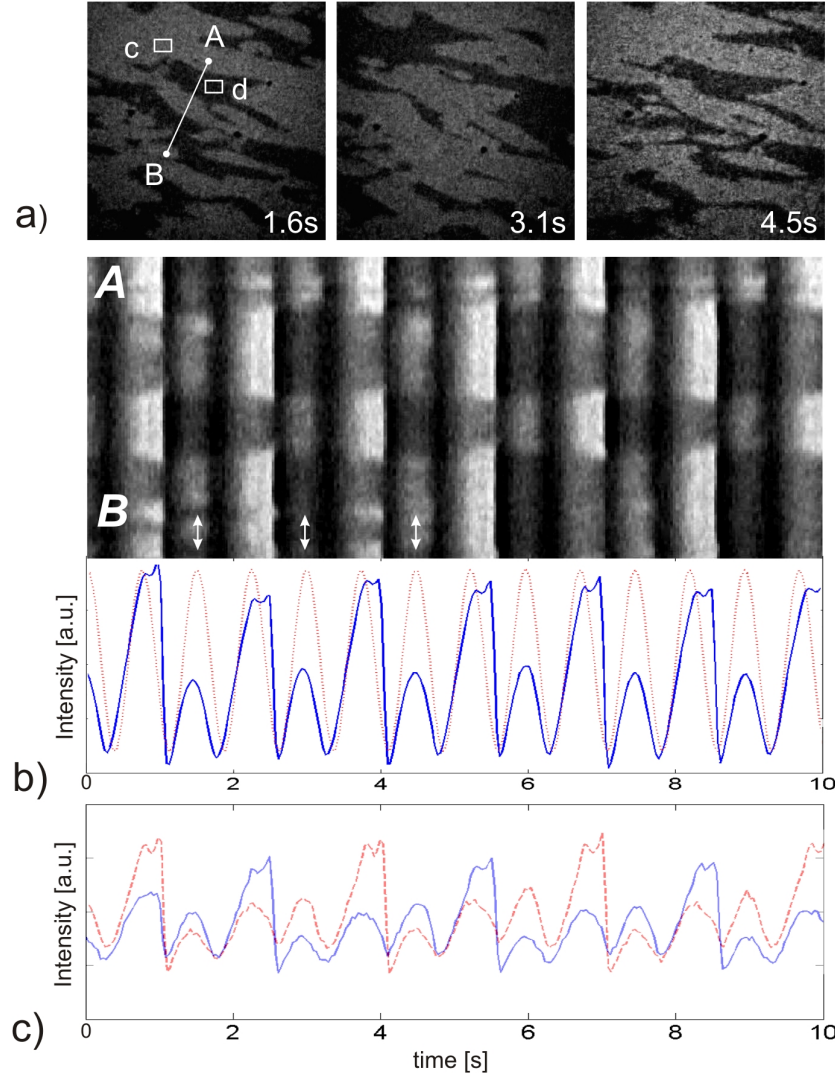


Figure 3.10: Oscillating clusters during the 2:1 forcing experiment. a) snapshots of $300 \times 300 \mu m^2$ PEEM images illustrating a phase locked regime. b) spacetime plot taken along the AB line (top), and the corresponding averaged overall intensity (bottom) of the PEEM image (continuous blue line) and the forcing signal (dotted red line). The white arrows indicate when the snapshots in a) were taken. c) local values of the intensity, calculated over rectangles c (dashed red line) and d (continuous blue line). The reaction parameters are $T = 529$ K, $p_{oxygen} = 1 \times 10^{-4}$ mbar, $p_{CO}^0 = 9.3 \times 10^{-5}$ mbar, γ is 0.22 % of the CO pressure base value. $\nu_0 = 0.7$ Hz, and $\nu_f = 1.4$ Hz [113].

Comparable phase clusters were already found by Bertram *et al.* [153] in the case of periodic low frequency forcing with high amplitude. The major difference is that the results presented in this section are obtained at 2:1 resonant frequency (1.4 Hz instead of 0.67 Hz), with forcing amplitudes more than one order of magnitude smaller; this is due to the fact that the effect of global forcing is maximal for resonant forcing frequencies.

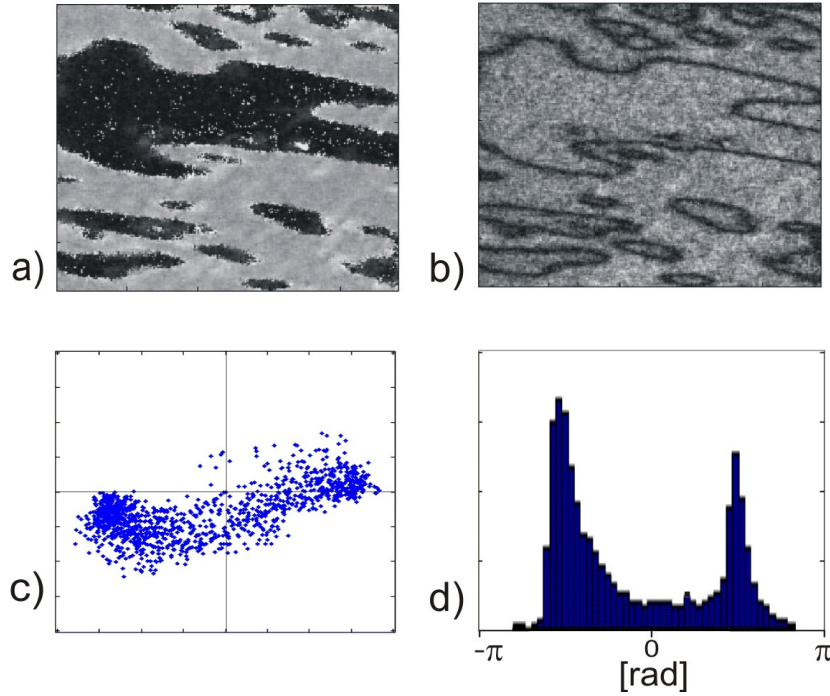


Figure 3.11: Phase and amplitude representation of a cropped region ($150 \times 150 \mu\text{m}^2$) of the cluster patterns shown in Fig. 3.10. a) phase pattern, b) amplitude pattern, c) phase portrait and d) phase histogram [113].

3.1.3.1 2:1 Bloch walls

The forcing of a spatially homogeneous assembly of oscillators, as shown above, may lead under particular conditions to stable inhomogeneous structures. The most simple of these structures are solutions which join two symmetrically equivalent states. In two dimensions (2D), the two stationary frequency locked solutions differ in phase by π . At

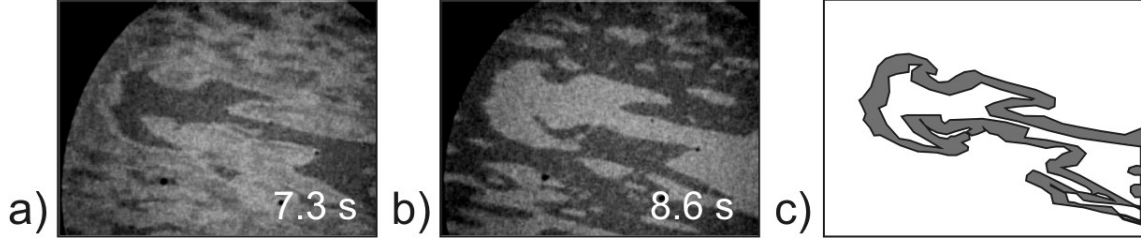


Figure 3.12: Cropped PEEM snapshots of the 2:1 clusters shown in Fig. 3.10 ($400 \times 300 \mu m^2$), representative of the enlargement-reduction cycles: phase domains swell and shrink periodically. a) minimal size domain (oxygen covered), and b) maximal size domain (CO covered), separated in time by two forcing cycles. c) Intersected area between the main domain on a) and on b).

the core of the kink, which connects the two solutions, the order parameter rotates in the complex plane and the oscillating amplitude is reduced [157]. The borders between domains of opposite phase in the arising structures are generally referred to as Bloch walls by analogy with those in corresponding structures in solid state physics.

In section 3.1.3 non-equilibrium Bloch walls were shown at the borders between two different entrained states differing in phase by π . They display traveling behavior and annihilate each other upon collision. To represent them, a stroboscopic xt -plot (Fig. 3.13) is used, so that the phase domains are compared at the same oscillatory state. The propagation speed of these Bloch Walls, also known as π -fronts, has a constant value of $0.35 \mu m s^{-1}$.

The relevant time unit in the observation of Bloch walls is the period of the oscillations. These π -fronts are better characterized if the dynamics of the forced clusters remain stable for a higher number of oscillations. The natural frequency drift exposed in section 3.1.1.3 implies a shortening of cluster stability in time, and is for this reason an obstacle in the Bloch wall analysis. An improvement in this direction is to use shorter cycles (faster forcing), and it will be tackled in section 3.1.4.1 together with a more detailed description of phase domains shape-related properties.

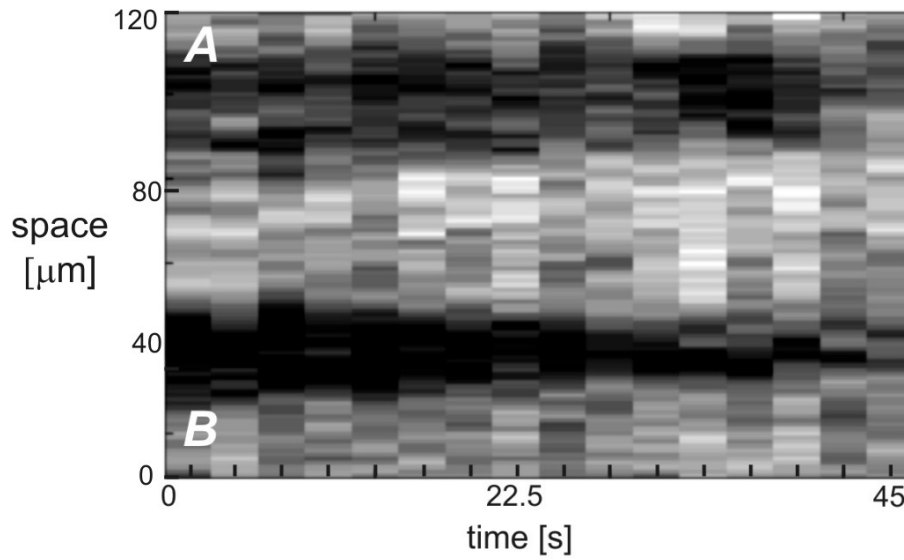


Figure 3.13: Space-time stroboscopic plot showing the pattern evolution along the same AB line of Fig. 3.10, showing one frame every 4 forcing cycles (2.84 seconds). Four Bloch walls separating different phase locked domains are identified; two of them approach each other at a constant speed of $0.35 \mu\text{m s}^{-1}$ [113].

3.1.4 3:1 Resonant forcing

Experiments similar to those presented in section 3.1.3 were carried out driving the system with three times its natural frequency ($\nu_f = 3 \nu_0$), where the gas-regulating device described in section 3.1.2 played a key role. Again, as seen in section 3.1.3, an initial state of chemical turbulence is set before applying any periodic modulation of the CO partial pressure. At a forcing strength of about 0.12 %, phase locked regimes were observed (Fig. 3.14). As can be seen in the corresponding xt -plot (Fig. 3.14 b)), the system performs oscillations with a frequency of $\nu = \nu_f / 2$ (2:1 entrainment).

An analysis of the local oscillations (Fig. 3.14 c)) reveals that —like in the case of 2:1 forcing —an additional shoulder appears during every oscillation cycle. However, it seems that for this amplitude of 3:1 forcing the system is not fully entrained. At $t = 5.5$ s the pattern inverts: in the xt -plot a large amplitude oscillation is not followed by a small shoulder but by another large amplitude oscillation. After this transition, the oscillations of the system are again 2:1 entrained.

The complex 3:1 dynamics are also apparent when phase and amplitude of the patterns are analyzed (Fig. 3.15). Two distinct clusters with sharp boundaries can be observed (Fig. 3.15 a) - b)). By contrast to 2:1 forcing, they have a different amplitude and are not contrasted by a phase difference of π (Fig. 3.15 c)). Moreover, the temporal evolution of the phase histogram (Fig. 3.15 d)) shows that the phase difference between the two clusters changes in the course of time. The two domains approach each other in phase space until a part of the cluster that lags behind skips half an oscillation cycle. This makes itself apparent at the transfer of a shoulder from one peak to another in the phase histogram and coincides with the inversion of the oscillation pattern in the xt -plot (Fig. 3.14): the alternation of dark to bright is broken at the 5th second of the sequence where a bright-bright event takes place. After this inter-cluster transfer, the phase difference recovers the value of π , to then resume shrinking again. The more complex behavior of the system is probably caused by the competition between the natural frequency and the enforced actual oscillation frequency which has a ratio of 2:3. This suggests that for higher values of γ the system may completely become 3 to 1 entrained. To test that, an enhancement on the amplitude modulation of the gas compressor is necessary; probably a larger secondary piston would be enough.

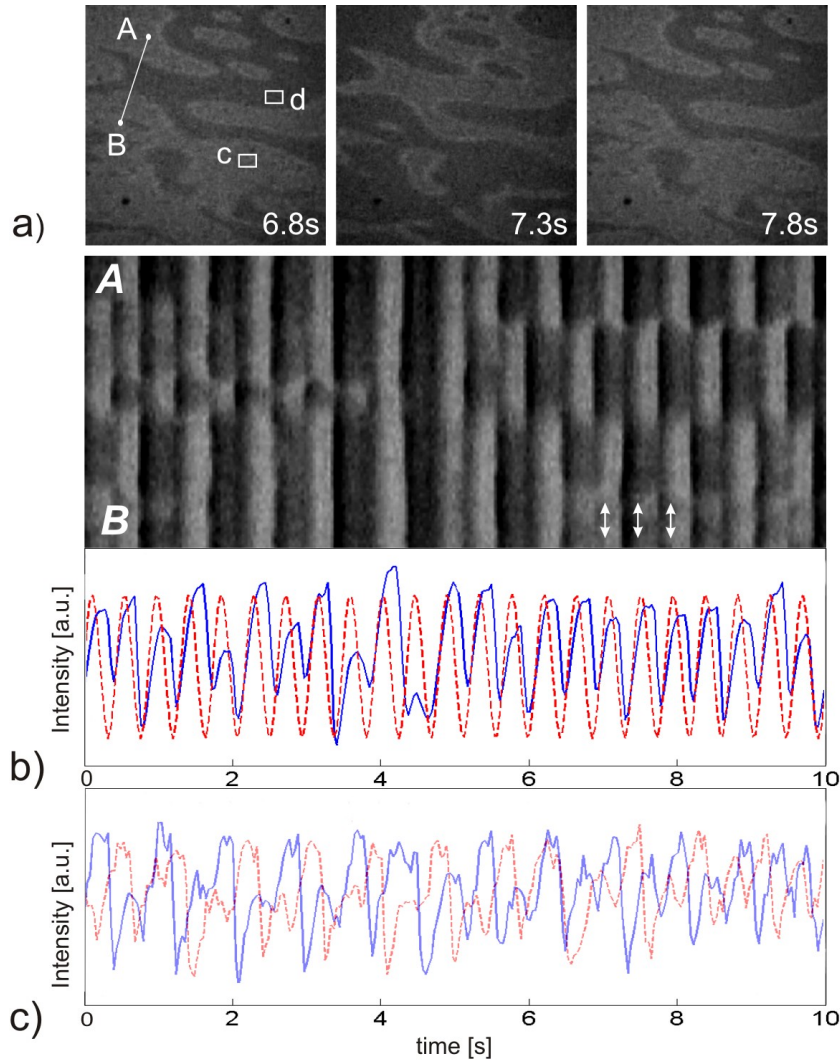


Figure 3.14: Oscillating clusters during the 3:1 forcing experiment with 2:1 entrainment. a) snapshots of $300 \times 300 \mu\text{m}^2$ PEEM images . b) space-time plots showing the pattern evolution along the AB line (top), and corresponding grayscale values (bottom) of the PEEM image (continuous blue line) averaged over the whole snapshot, and the applied forcing signal (dashed red line). The snapshots in a) are indicated with white arrows. c) local values of the intensity, calculated over rectangles c (continuous blue line) and d (dashed red line). The reaction parameters are $T = 526 \text{ K}$, $p_{\text{oxygen}} = 1.5 \times 10^{-4} \text{ mbar}$, $p_{\text{CO}}^0 = 6.9 \times 10^{-5} \text{ mbar}$, γ is 0.12 % of the CO pressure base value, $\nu_0 = 0.76 \text{ Hz}$, and $\nu_f = 2.3 \text{ Hz}$ [113].

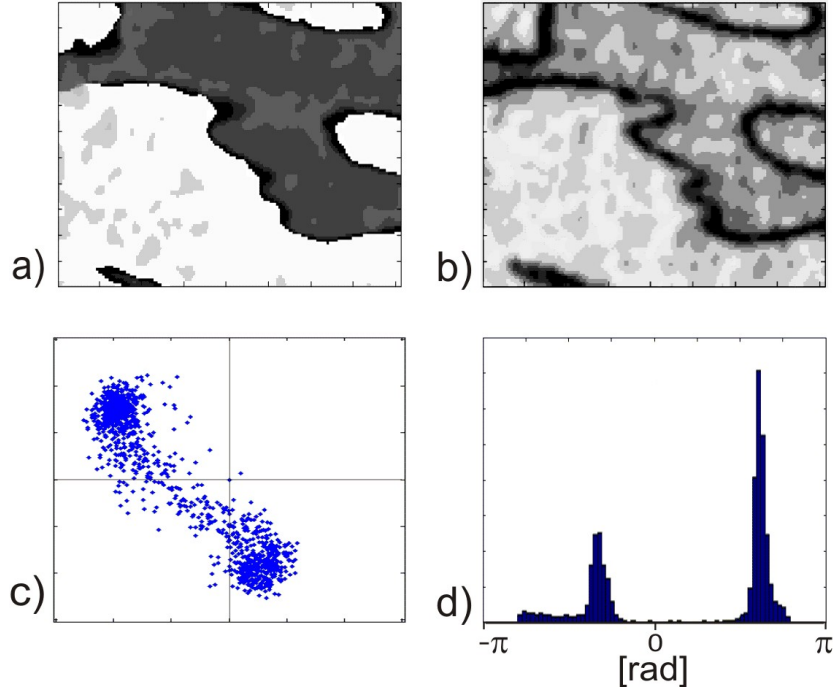


Figure 3.15: Phase and amplitude representation of a cropped region ($100 \times 100 \mu m^2$) of the cluster patterns shown in Fig. 3.14. a) phase pattern, b) amplitude pattern, c) phase portrait, and d) phase histogram [113].

As in section 3.1.3, CO diffusion plays a role in the size of the clusters formed, which undergo periodic changes, “breathing” every two forcing cycles, although less pronounced in this case as Fig. 3.16 shows: the intersecting area depicted is smaller than the one shown in Fig. 3.12 c).

3.1.4.1 3:1 Bloch walls

The resonant 3:1 forcing recorded in the PEEM sequence above (Fig. 3.14), shows well defined borders separating oscillating subpopulations, which are also seen in the corresponding amplitude and frequency map (Fig. 3.15). Nonetheless, the phase difference between domains is not always π (section 3.1.4), and therefore the name of “Bloch wall” has to be used with caution here, in awareness of the grammatical license. The behavior

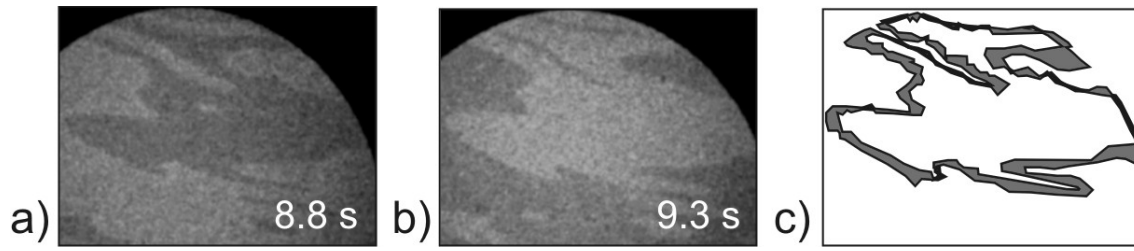


Figure 3.16: Cropped PEEM snapshots of the 3:1 clusters sequence shown in Fig. 3.14 ($400 \times 300 \mu m^2$), representative of the enlargement-reduction cycles. a) minimum size domain (oxygen covered), and b) maximum size domain (CO covered), separated in time by one forcing cycle. c) enhancement of the intersected area between the main domain in a) and that in b). The phase domains swell and shrink regularly, with a periodicity of two forcing cycles.

of the 3:1 Bloch walls is comparable with that of the 2:1 case. Both are characterized by a minimum in the oscillation amplitude (Fig. 3.15 b)) and move slowly (Fig. 3.17).

As mentioned in section 3.1.3.1, the relevant time unit of a Bloch wall is the number of oscillations. The 3:1 Bloch walls dynamics are faster and reach a higher number of oscillations in the same time period than 2:1 walls; this indexes them as better candidates for a more in-depth analysis. For this purpose, a numerical simulation of the CO 3:1 forced reaction was made by C. Punckt using the KEE model (introduced in section 2.4.4), and it is compared with the amplitude map of an experimental sequence in Fig. 3.18. Phase locked domains can also be considered as regions with a particular surface reconstruction surrounded by a different phase: Pt(110) 1×1 (1×2) reconstructed islands in a sea of 1×2 (1×1) surface structure. This interface (1×1 - 1×2) tends to minimize its length. As a result, rounded domains evolve into circles and shrink (even disappearing at times, specially the small ones), while almost straight walls undergo straightening. Representative examples, in close agreement between model and experiment, can be seen in Fig. 3.18.

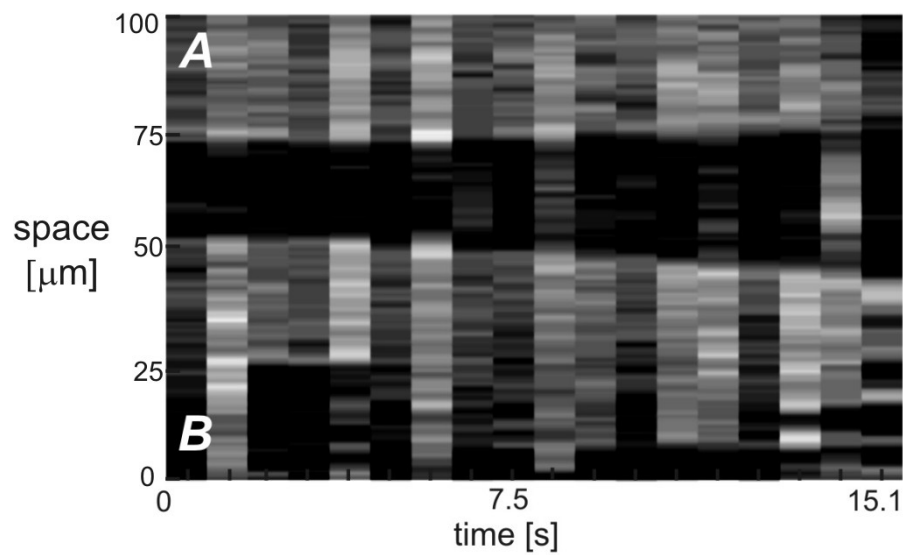


Figure 3.17: Space-time stroboscopic plot showing the pattern evolution along the same AB line of Fig. 3.14, choosing one frame every 2 forcing cycles (0.84 s). Cluster boundaries separating different phase locked domains move apart [113].

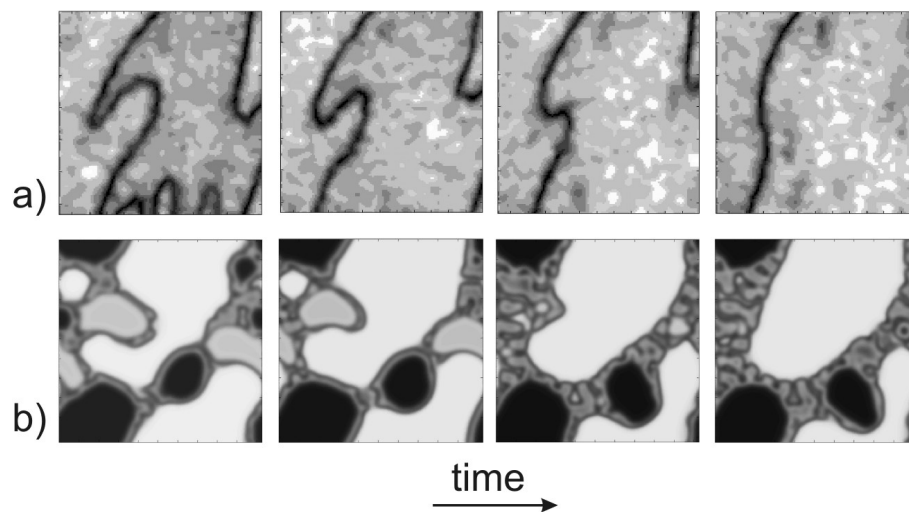


Figure 3.18: 3:1 forcing domain border dynamics compared: a) experimental amplitude map, b) numerical simulation (done by C. Punckt).

3.1.5 4:1 Resonant forcing

The compressor designed presented in section 3.1.2 and used in the 3:1 forcing experiments allows an even faster modulation of the CO partial pressure in the UHV chamber: $\nu_f = 4 \cdot \nu_0$, for $\nu_0 \approx 1\text{Hz}$. Once the crystal surface exhibits spiral turbulence, the stepper motor of the compressor is started to achieve global forcing of the catalytic reaction. For $\gamma = 0.1\%$ frequency locked four-phase clusters arise. Fig. 3.19 a) shows four snapshots of the PEEM sequence where the corresponding spatiotemporal patterns can be seen: structures that look similar to turbulence with abrupt interruptions every forcing cycle. The xt -plot shows a cascade pattern (Fig. 3.19 b)), in which domain borders are not stationary and yet a periodicity of four forcing cycles is evident. The plot of the PEEM image intensity in Fig. 3.19 b) shows oscillations fully entrained with the forcing signal. However, if this snapshot intensity plot is done locally (Fig. 3.19 c)), choosing a smaller area, a periodicity pattern of four forcing cycles can be distinguished, very similar to that plotted in Fig. 3.10 c).

Four different phase states are visible in the phase pattern in Fig. 3.20 a) as black, dark gray, gray, and light gray areas, while the amplitude pattern in Fig. 3.20 b) shows that the oscillation amplitude is strongly reduced in the interface between domains. Even though smaller than in the previous sections (2:1 and 3:1 clusters), the developed structures still consist of domains where the phase is locked. In the phase portrait in Fig. 3.20 c) four individual clusters can be distinguished, each with a phase difference of $\pi/2$ radians to its neighbors (Fig. 3.20 d)).

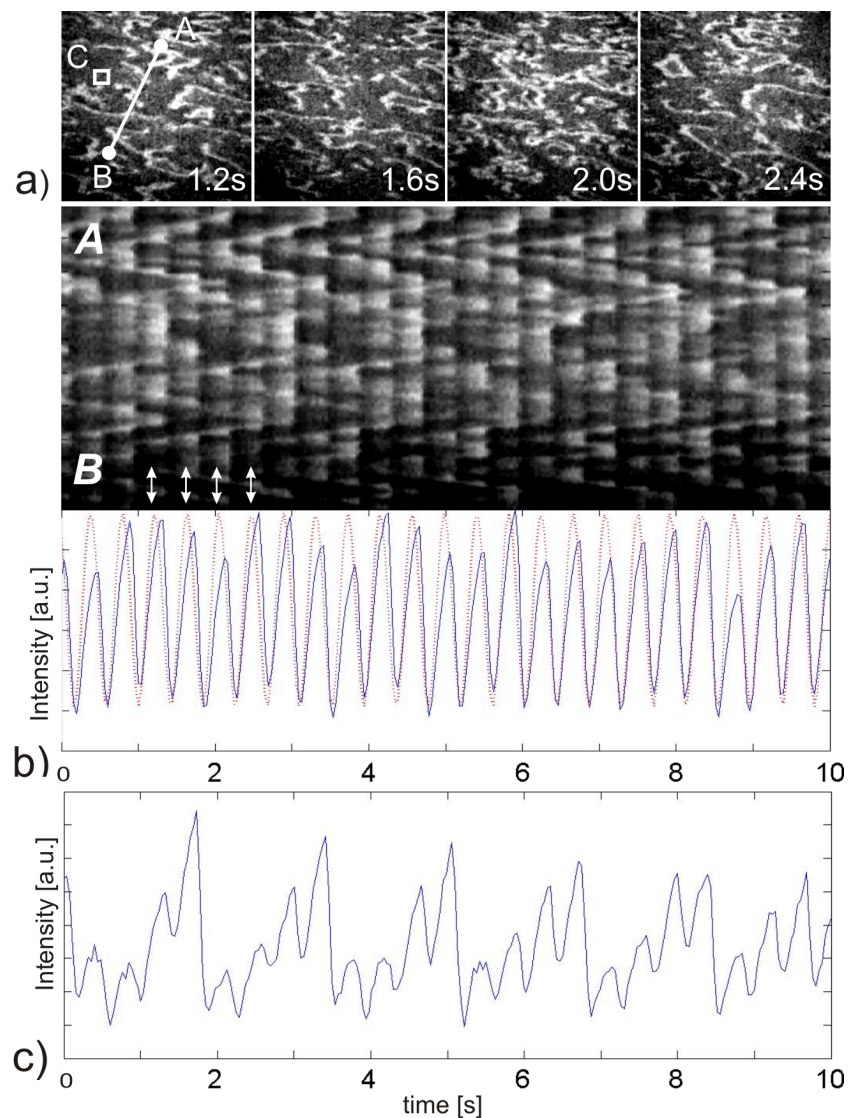


Figure 3.19: Four-phase traveling patterns during 4:1 forcing. a) snapshots of $300 \times 300 \mu\text{m}^2$ PEEM images. b) space-time plot showing a cascade shaped pattern evolution along the AB line (top), and corresponding grayscale values (bottom) of the PEEM image (continuous blue line) averaged over the whole snapshot, and the applied forcing signal (dashed red line). The white arrows indicate the time of the a) snapshots. c) PEEM intensity averaged over the whole image. The reaction parameters are $T = 543 \text{ K}$, $p_{\text{oxygen}} = 1.7 \times 10^{-4} \text{ mbar}$, $p_{\text{CO}}^0 = 5.9 \times 10^{-5} \text{ mbar}$, $\nu_0 = 0.65 \text{ Hz}$, $\nu_f = 2.6 \text{ Hz}$ and γ is 0.1 % of the CO base pressure value.

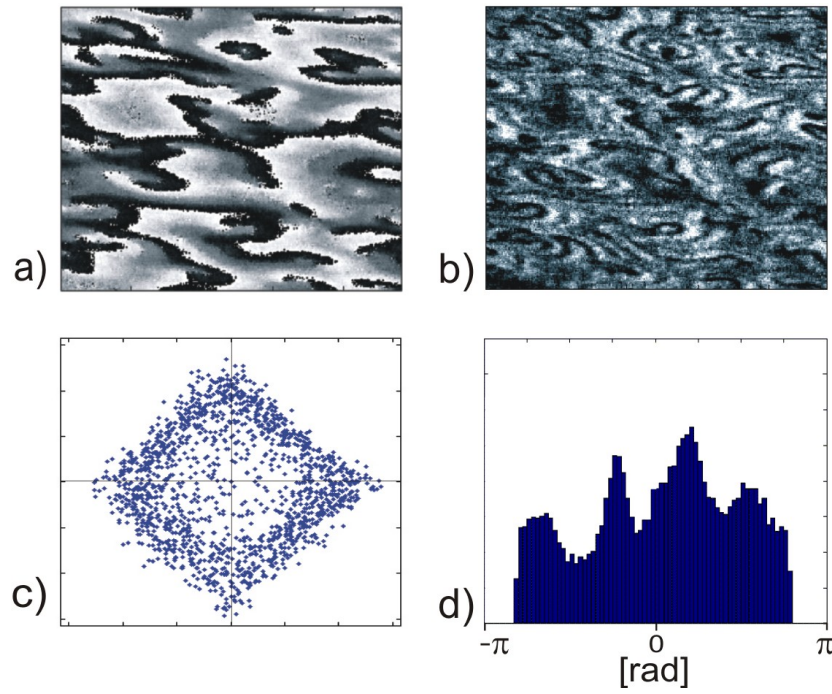


Figure 3.20: Phase and amplitude representation of a cropped region ($100 \times 100 \mu m^2$) of the cluster patterns shown in Fig. 3.19. a) phase pattern, b) amplitude pattern, c) phase portrait, and d) phase histogram.

3.1.6 Forcing effect on propagating pulses (1:1, 2:1, 3:1, 4:1)

The previous sections were focused on the suppression of chemical turbulence in the Pt-CO system, and the resulting spatiotemporal pattern formation. Global forcing techniques can also be applied to propagating pulses, which leads to interesting new patterns too, whereby different simultaneous reaction dynamics are affected in different ways by the same uniform partial pressure modification.

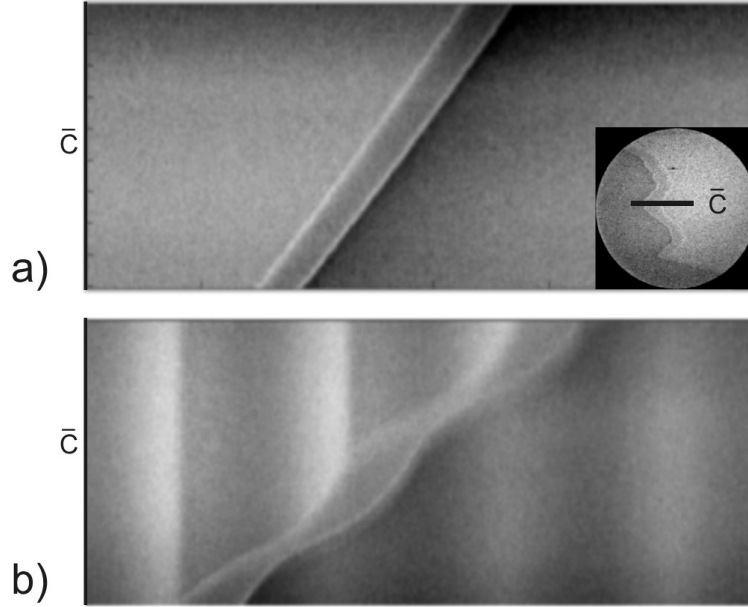


Figure 3.21: XT-plot of a propagating pulse along the line \bar{C} during 8 seconds: a) without forcing and b) under 2:1 forcing. The reaction parameters are $T = 504$ K, $p_{oxygen} = 1.4 \times 10^{-4}$ mbar, $p_{CO}^0 = 6.3 \times 10^{-5}$ mbar, $\nu_0 = 0.25$ Hz, $\nu_f = 0.5$ Hz and γ is 0.2 % of the CO base pressure value. The inset image in a) is a PEEM frame where the pulse with the cropped line \bar{C} can be seen.

A propagating pulse with constant velocity and with constant shape, like the one in Fig. 3.21 a), presents itself as a reaction wave moving across a medium that is otherwise at rest state. It can be either considered as an excitable phenomenon or as a bistable one. If resonant forcing is applied (as explained in section 3.1.2), two differentiated effects

can be seen, depending on the state of the medium. In the excited region, the width of the pulse is periodically modulated, increasing and decreasing its width. The front of the pulse and the rear approach and move apart with a periodicity that is completely entrained to the periodic forcing ν_f . The maximum pulse width is proportional to the forcing amplitude γ . This proportionality was found to hold for experimental results obtained at 1:1, 2:1, 3:1, and 4:1 resonant forcing.

At the same time, the remaining region of the medium (not occupy by the pulse) is affected by the forcing in a different manner: it exhibits homogeneous oscillations that are likewise entrained to ν_f . The combination of both effects delivers a remarkably vivid xt -plot that can be seen in Fig. 3.21 b).

3.1.7 Conclusions

The effect of periodic external global forcing on the catalytic CO oxidation on Pt(110) has been studied for chemical turbulence and propagating pulses, in particular the 2:1, 3:1, and 4:1 regimes. A compressor driven reactor was designed and built to allow experiments with such high forcing frequencies. The observed pattern formation is discussed in the context of present experimental results and previous theoretical studies.

For particular values of the amplitude under 2:1 and 3:1 forcing, the condition of the system adopted a regime dominated by phase locked cluster-domains. Phase fronts separating different homogeneous phase locked states were clearly observed during our experiments, in agreement with numerical simulations of the forced KEE model [155]. In addition, the latter theoretical work predicts front explosions for decaying forcing amplitudes: turbulent interfacial zones for 2:1 resonant forcing and labyrinth patterns for the 3:1 case. This could not be observed in our experiments, probably due to the high sensitivity of the system to parameter changes and present technical limitations in the application of soft changes in γ . Every parameter change in our set-up is followed by a short period of self-adjustment of the system, long enough to perturb the reaction dynamics significantly, and thus transition dynamics between different patterns could not be resolved. A gas forcing setup allowing a more gradual adjustment of ν_f might mean a relevant improvement for future experiments.

The nature of the clusters arising in the experiments with highest forcing ratio (4:1) reported here seem different from those in the rest of the experiments (2:1, 3:1). The reason why the size of these structures is notably reduced is not totally understood. It may be due to the different degree of border stability which does not allow larger stable domains, or that the forcing amplitude is not large enough at these frequencies. A gas dosing system able to dose larger amounts of gas (γ) into the reaction chamber could be helpful to complete the resonant forcing analysis.

Combining a broader range of forcing amplitudes for every forcing frequency with a finer variation of forcing parameters (γ and ν_f) would make possible, for instance, to experimentally reproduce detailed Arnold tongues in the 2:1, 3:1, and 4:1 regimes.

3.2 Effect of noise

Natural systems are inevitably subject to random fluctuations, caused by either environmental variability or thermal effects. In particular, noise-influenced reaction parameters are involved in any far from equilibrium system [19, 158, 159, 160]. Such fluctuations are known to interact with the nonlinearities of a system in ways that induce, enhance, or sustain ordered behavior [161]. For instance, waves sustained by artificial noise introduced in the Belousov-Zhabotinsky reaction [162, 163], and generation of pacemakers and spiral dynamics by noise have been reported [164, 165, 166]. A systematic study of the role of noise in these instances may help to better understand the behavior of an extended system under real-world conditions.

The present section is dedicated to the emergence of spatiotemporal structures in the CO oxidation on Pt while global noise is artificially introduced. Experiments are presented and compared with theoretical results obtained by S. Alonso using the KEE model (complementary information is given in section 2.4.4 and in the appendix at the end of this chapter). The first experiments in this section were done to scale fluctuations in the gas dosing system at given experimental parameters in terms of a “mild noise” to “strong noise” range. The former extreme is given when there is no reaction of the system at all, while the latter is noise of such intensity that the system is completely governed by it. Between these extremes one observes an interesting range of transient pattern formation, where noise interacts with the non linearities of the system. The reference values were obtained by imaging the evolution of chemical turbulence once different noise parameters were introduced in the reaction (3.2.2). Afterwards, in section 3.2.3, attention was paid to bistable transitions, and section 3.2.4 points out the possible use of noise to enhance reactivity. A discussion closes the whole chapter.

3.2.1 Experimental implementation

The experiments related with the noise induced effects were performed using the basic setup sketched in Fig. 3.1, and explained in a more general manner in section 2.4.6.1. A meaningful modulation of the CO partial pressure was introduced into the system as a computer controlled source of random fluctuations following:

$$p_{CO}(t_i) = p_{CO}^0(1 + rand_i \cdot \Delta N) \quad (3.2)$$

where *rand* is a random number between -1 and +1 that is regenerated by the computer in time intervals of Δt ($t_i - t_{i-1} = \Delta t$). ΔN is the percentage of CO partial pressure that is added to the base value. The combination of the parameters Δt and ΔN determines how fast and how much $p_{CO}(t)$ changes, or in other words, the magnitude of the multiplicative noise present in the reaction. The two parameters are input into the computer that controls the CO gas dosing valve. Due to this solenoid valve effective reaction time and the low-pass filtering between the dosing system and the chamber (described in section 3.1.2), the generated rectangular signal is integrated by the system, resulting in a gaussian wave in the solenoid valve and in the reaction chamber, as shown in Fig. 3.22. Hence, the CO partial pressure in the reaction environment has a fluctuating value between $p_{CO}^0 + \Delta N$ and $p_{CO}^0 - \Delta N$, homogeneous in space, characterized by a gaussian shape histogram like the one depicted in Fig. 3.22 b).

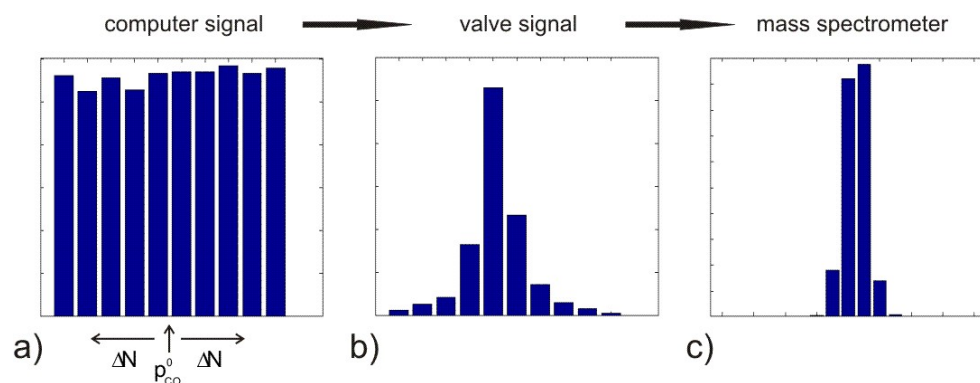


Figure 3.22: Histograms of the $p_{CO}(t)$: a) generated signal, b) signal in the dosing system, and c) mass spectrometer lecture of the reaction chamber.

Once again, PEEM (section 2.4.6.2) proves to be an excellent tool for tracking the adsorbates local density and the surface dynamics in real time.

3.2.2 Turbulence suppression by noise

Chemical turbulence on a platinum crystal surface can be effectively suppressed by a noisy modulation of the reactant supply, namely $p_{CO}(t)$. Fig. 3.23 represents the corresponding

spatiotemporal patterns seen when different noise intensities (different combinations of Δt and ΔN) are applied to a turbulent regime. In absence of external noise, spiral turbulence develops freely. As the noise intensity increases (left to right and/or bottom to top) the system is driven to a partially suppressed state featuring an alternation between asynchronized and homogeneous global oscillations. Remarkably, the frequency of such response is different than the characteristic frequency of the spiral turbulence. Finally, the noise reaches values that completely annihilate the reaction dynamics; the system then follows the noise signal oscillations.

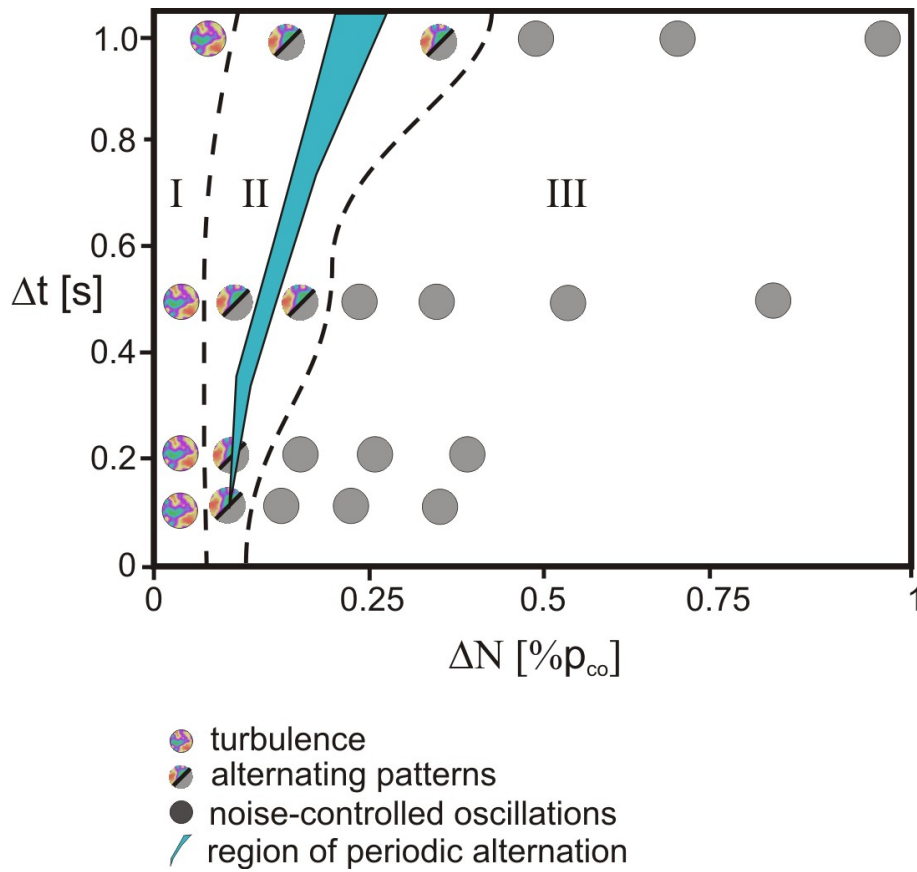


Figure 3.23: Spatiotemporal patterns corresponding to different noise parameter values (Δt and ΔN), applied on an initial turbulence state, with reaction parameters: $T = 540$ K, $p_{O_2} = 1.3 \times 10^{-4}$ mbar, and $p_{CO}^0 = 6.6 \times 10^{-5}$ mbar. Areas for four distinct regimes are pointed out.

The series of space-time plots depicted in Fig. 3.24 show the typical surface dynamics of each of the three regions (I, II, and III) of Fig. 3.23, and are compared with numerical simulations; one can see how well the plots based on the KEE model qualitatively agree with the experimental results.

Stronger or faster modulations than were used for Fig. 3.23 are not considered because of the limitations of the experimental setup (experiments showed strong disagreement between the computer values and the real state in the chamber for values $\Delta t < 0.1$ or $\Delta N > 3 \% p_{CO}^0$). Besides, this study project was specifically focussed on smallest fluctuations with a relevant impact.

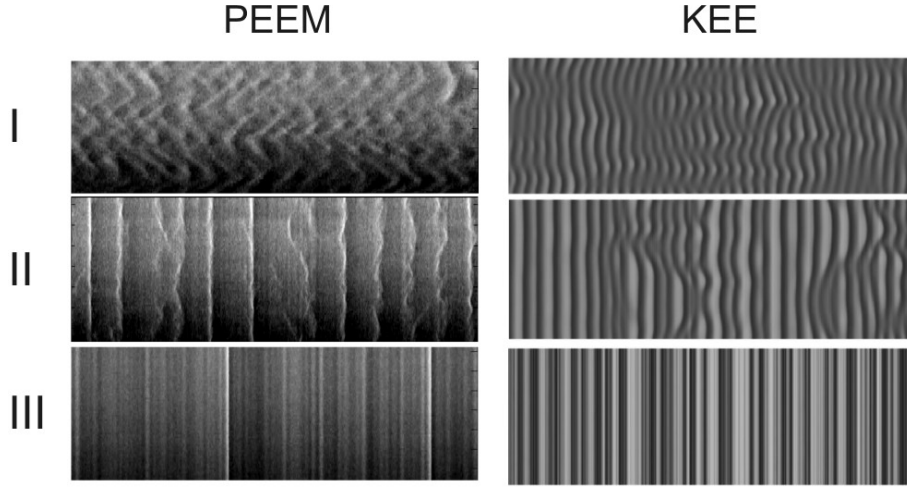


Figure 3.24: Space-time plots corresponding to the turbulence suppression map regions I, II, and III; experiments (PEEM) vs. numerical results (KEE).

3.2.2.1 System oscillation frequency

The oscillation frequency of the system is affected by the global noise that is artificially introduced. Fig. 3.25 shows how the periodicity of the local oscillations changes, and compares the initial spiral turbulence of region I (Fig. 3.23), the periodic induced patterns within region II, the noise controlled region III, and the spatiotemporal dynamics when Δt and ΔN are set back to zero and spiral turbulence reappears (shown in region IV). Typically, the local oscillations frequency decreases from region I to II,

slowing down for higher values of ΔN . Region III has no local periodicity whatsoever and reflects the imposed random oscillations. Region IV is characterized by spiral turbulence similar to that of region I, but with lower frequency ($\nu_0' < \nu_0$). This slow down of the dynamics is expected, being caused by structural changes on the crystal surface [113], and depends on the sample temperature (see section 2.4.2 and 3.1.1.3). The global noise not only couples the whole system but also reduces the frequency of the patterns. Space-time plots, PEEM image grayscale, and a set of values for particular cases are given in Fig. 3.25.

3.2.2.2 Periodic induced behavior

Region II of Fig. 3.23 encompasses the range of noise parameters in which the original spiral turbulence is not completely suppressed. Interaction with noise drives the active media through transient states, alternating between spatiotemporal chaos and a lack of patterns. Furthermore, for certain parameters these cycles may become regular. Fig. 3.25 region II a) shows the time evolution of a cropped line on the platinum surface: suppressed patterns alternate with re-activated turbulence in regular cycles of 4 seconds. The noise parameters corresponding to this induced behavior draw a narrow stripe in the turbulence suppression map (seen in Fig. 3.23). Along that stripe, the interplay between excitability, refractory time, noise, and diffusion results in time regularity.

3.2.3 Transitions anticipated by noise

Further experiments were focused on the bistable transition from a mainly oxygen covered Pt crystal to a mainly CO covered state. These experiments start with a certain amount of oxygen in the reaction chamber ($p_{O_2} = 1.1 \times 10^{-4}$ mbar) and no CO. When the surface is oxygen covered, the p_{O_2} is kept constant, and then the p_{CO} is increased. At sufficiently large value of the CO partial pressure all the adsorbed oxygen is reacted away releasing CO_2 , the sample ends up completely CO covered. The transition is clearly discernable in the PEEM images (Fig. 3.27 top): it is seen as the change from a uniformly dark expanse to a uniformly bright one through a number of growing bubbles. The KEE model forecasts similar transition patterns (Fig. 3.27 bottom).

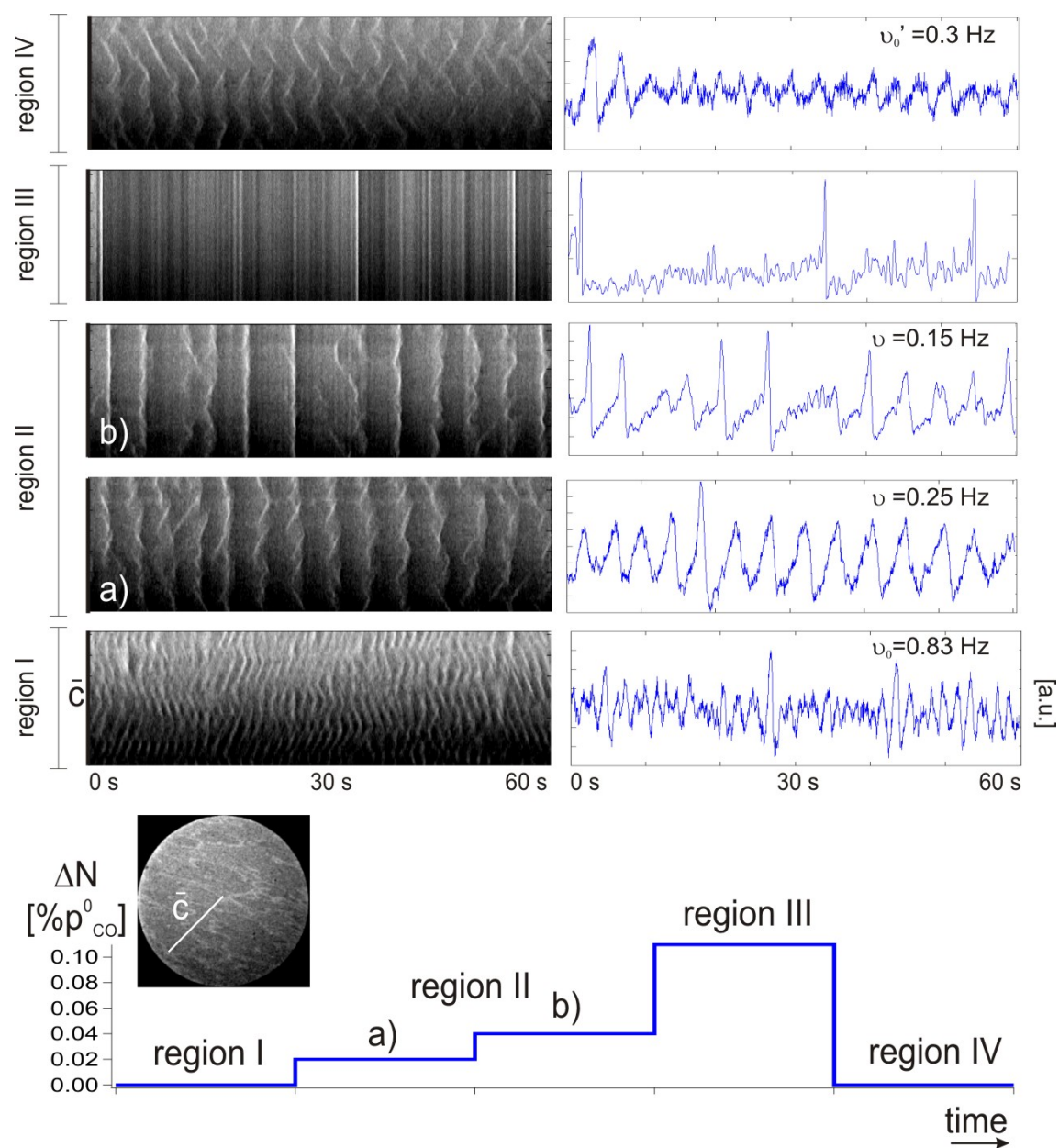


Figure 3.25: Space-time and grayscale plots of the PEEM imaged for different values of ΔN . Reaction parameters are $T = 540$ K, $p_{O_2} = 1.3 \times 10^{-4}$ mbar, $p_{CO}^0 = 6.6 \times 10^{-5}$ mbar, and $\Delta t = 0.05$ s.

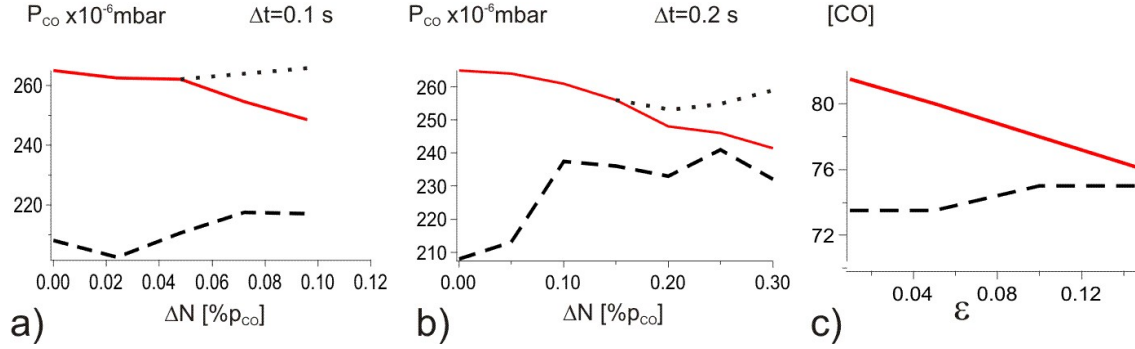


Figure 3.26: a) and b) show the critical p_{CO} of both transitions, from oxygen covered to CO covered (continuous red line) and from CO covered to oxygen covered platinum (black dashed line), for two different values of applied noise. The black dotted line delimits together with the red line the parameter region where patterns induced by defects take place. Reaction parameters are: $T = 509$ K, $p_{O_2} = 1.1 \times 10^{-4}$ mbar. c) represents the corresponding numerical simulation by S. Alonso, plotted in terms of the simulation parameter ε , related with the noise intensity (see section 3.2.6).

The same steps are followed backwards for the back-transition to the initial state. Nevertheless, the critical p_{CO} is lower in this case, which is explained by the asymmetric inhibition of the reaction: the poisoned CO covered surface does not behave in the same way as the oxygen covered platinum [59]. There is an inherent hysteresis loop in this bistable transition, as explained in chapter 2 (section 2.4.2) due to the asymmetry of the reaction. Fig. 3.26 describes how the mentioned hysteresis loop shrinks as the noise applied is larger. Right above the line that represents the transition to a CO covered surface in Fig. 3.26 a) and b), there is a triangle of p_{CO} values, between the continuous red line and the dotted black line, where defect-induced patterns appear (see also Fig. 3.27). Although the crystal is homogeneously covered, the role of defects on the surface becomes clear in its interplay with the sharp changes of one of the reaction parameters. Deep drops of the p_{CO} signal are followed by the initiation in some defects of spirals and target patterns. These sort of structures are rapidly suppressed in the next steps of the generated signal (lifetime between 0.5 - 15 seconds), and do not appear at all in the corresponding model simulation.

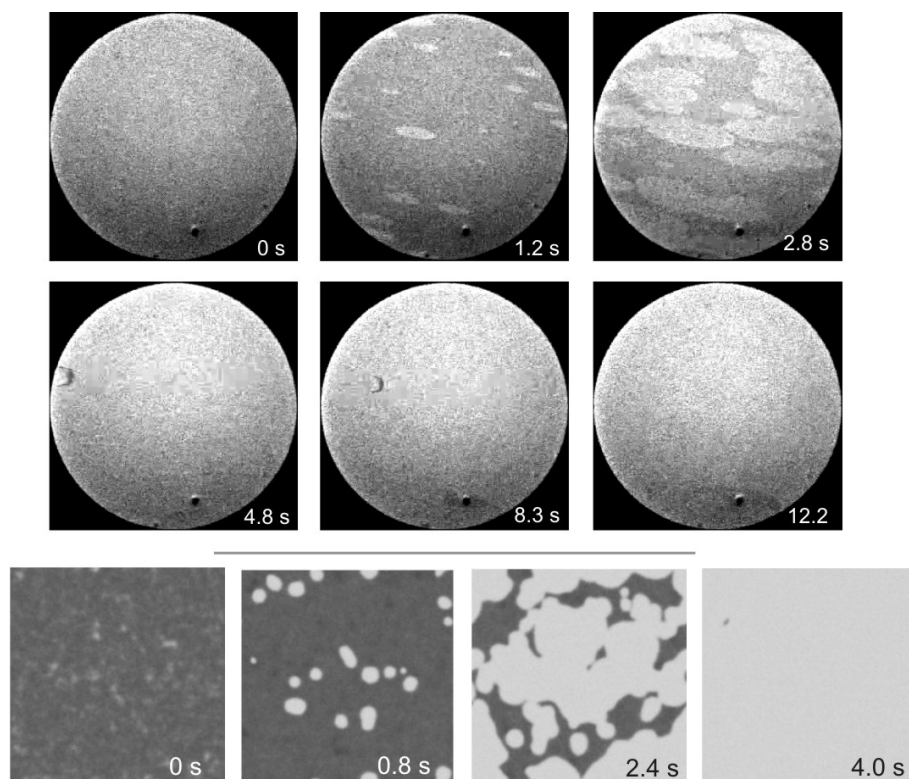


Figure 3.27: PEEM snapshots (top) compared with numerically generated images (bottom). Different stages of the bistable transition oxygen covered to CO covered can be seen, including defect-induced patterns once the transition is already fulfilled (see the last three PEEM frames). Experimental parameters are: $T = 509$ K, $p_{O_2} = 1.1 \times 10^{-4}$ mbar, $\Delta t = 0.25$ s, and $\Delta N = 0.5 \% p_{CO}^0$. Parameters used for the simulation: $p_{O_2} = 0.00045$, $p_{CO} = 0.0000908$, and internal noise $d = 0.005$.

3.2.4 CO₂ production increment

Besides the spatiotemporal noise-induced patterns, the experiments performed with noise also featured an increase in the resulting amount of CO₂ produced in the CO oxidation. A mass spectrometer measured the CO₂ present in the UHV chamber while chemical turbulence developed, with and without modulating the p_{CO} . For the same amount of reactants involved in the reaction, integrated in time, the carbon dioxide production rate was higher with a fluctuating carbon monoxide partial pressure. This augmentation is reflected in Fig. 3.28, where the productivity of CO₂ rapidly approaches a maximal value when $\Delta t=0.5$ and $\Delta N = 0.2 \% p_{CO}^0$, or $\Delta t=0.75$ and $\Delta N = 0.1 \% p_{CO}^0$.

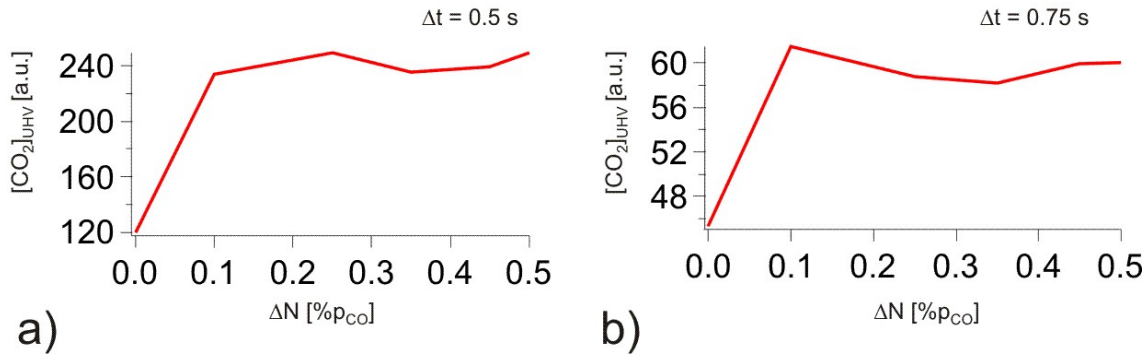


Figure 3.28: Increases in the CO₂ reaction rate due to the CO fluctuations. Reaction parameters for a) (and b)) are: $T = 526$ K, $p_{O_2} = 1.2 \times 10^{-4}$ mbar, and $p_{CO}^0 = 5.2 \times 10^{-5}$ mbar ($p_{O_2} = 1.07 \times 10^{-4}$ mbar, and $p_{CO}^0 = 4.4 \times 10^{-5}$ mbar).

3.2.5 Discussion

The role of random fluctuations in the CO catalytic reaction on Pt(110) has been presented. As mentioned at the beginning of the section, the interplay between excitability, noise, and diffusion may actually enhance regular behavior, as well as alter phase transitions.

The control of chemical turbulence is a problem tackled from a number of different angles [167]. In the CO-Pt system for instance, attempts have been made with feedback

techniques [82, 168], local control [117], and periodical global forcing [153]. The present work adds resonant periodic forcing and the use of noise to this list. The forcing amplitude needed to effectively suppress turbulent states in p_{CO}^0 percentage was reported to be 10 - 20 % for the periodically forced reaction [153]. Closer analysis of the initial turbulent dynamics, determining the natural frequency of the system, and performing periodical global forcing at a resonant frequency (as shown in sections 3.1.3, 3.1.4, 3.1.5, and in [113]) allows one to reduce the forcing amplitude by two orders of magnitude. The same order of magnitude (0.1 - 0.2 %) is enough for fast random modulations (section 3.2.2) to reach total entrainment. It is remarkable that the latter is independent from our previous knowledge of the system, which means that no estimation of the natural frequency of the system is needed. In addition, it was shown how global noise influences the reaction, coordinating the whole system and reducing the characteristic frequency of the patterns.

When the CO-Pt system shows developed spiral turbulence and global noise is introduced, noise behaves as an overall coordinating factor that gives a certain spatial coherence to otherwise discoordinated oscillations. In this way, chemical turbulence can be suppressed. Fig. 3.23 indicates that the introduced noise has a stronger influence in the reaction dynamics (less percentage of p_{CO}^0 needed to suppress turbulences) for fast modulations (small Δt); that is it, when the system has shorter time to assimilate the reaction parameters. The cases of intermittent turbulence suggest that the global coordination is not absolute, and the time needed for the active medium to recover its excitability plays a role in the alternation periodicity.

The fluctuations also had an influence on the transition between two stable states, anticipating a bistable transition of the system and shortening the intrinsic hysteresis loop. Using a mechanics heuristic model, the bistable transition anticipation is conceptually equivalent to the motion of a particle in a double-well potential [169], in which external noise gives energy to the system to save the barrier in that double-well potential. For moderate noise has been shown that the reaction mechanism of the system jumps more easily the barrier that separates the two steady regimes. For extremely large noise, that jump would become so small that the system is indifferently at one of the two local minima of the potential, or transiting between them.

Defect-induced fronts were experimentally observed during the anticipated bistable transitions. When the transitions were completed and the crystal surface showed a full

CO coverage, deep drops of the p_{CO} signal led to the emergence of spirals and target patterns at some defects. These oxygen structures propagated along the surface for short time before they disappeared. This is a very rare phenomenon because the reaction mechanism of the CO oxidation favors the formation of CO structures rather than oxygen structures.

A production increase of CO_2 was also observed but not totally understood, and its explanation remains as a future task. A proposed partial answer using the same heuristic model as above is that the system somehow is able to focus the energy introduced by the noise into jumping over the reaction energy barrier, and therefore it increases the production. That parameter fluctuation enhances productivity has already been reported for other systems, namely the ozone production in atmospheres of urban areas [169]. This fact raises the question of a possible catalytic effect of noise, which could also be relevant for increasing productivity in other chemical systems.

In the context of such real-world systems like marine ecosystems [170, 171] or the ozone production [169], in which stochasticity processes combine with periodic annual or daily cycles, it seems worthwhile for the future to combine the two global modifications examined in the present chapter: periodic and noisy modulations of the CO oxidation reaction parameters.

3.2.6 Appendix: reaction model

The numerical simulations presented in section 3.2 were performed by S. Alonso using the KEE model (see section 2.4.4). The values of the parameters that were employed are shown in table 3.1. These parameters basically correspond to previous numerical studies of the same experimental system [65, 172]. In order to simulate the experimental conditions of random external pressure of the partial pressure of CO, a stochastic variable was added to the pressure:

$$p_{CO} = p_{CO}^0 (1 + \xi_e(t)) \quad (3.3)$$

where the variable $\xi_e(t)$ is a gaussian white noise with null mean $\langle \xi_e(t) \rangle = 0$ and variance $\langle \xi_e(t)\xi_e(t') \rangle = 2\epsilon\delta(t - t')$, and ϵ is the intensity of the noise. This noise is completely uniform and it has no spatial structure.

Heterogeneities are known to occur on real crystal surfaces, qualitatively affecting the dynamics of surface waves; to consider these internal irregularities, together with additional defects and variables, we introduce an additive noise $\xi_i(x, t)$ in the first equation of the model (section 2.4.4). This is a gaussian white noise distributed in space with null mean $\langle \xi_i(x, t) \rangle = 0$ and variance $\langle \xi_i(x, t)\xi_i(x', t') \rangle = 2\epsilon_i\delta(x, x')\delta(t - t')$, where ϵ_i is the intensity of the noise. The intensity of this noise will be kept constant for all the numerical simulations to be presented here, as we will not be undertaking a systematic study of these internal sources of fluctuation.

Due to the particularities of the stochastic partial differential equations, we integrate the three equations of the model using the Heun method [173]. Two-dimensional numerical simulations are carried out using finite difference approximation, with a spatial and temporal discretization of $\Delta x = 2 \mu m$ and $\Delta t = 0.001$ s respectively. Periodic boundary conditions were always considered.

Table 3.1: Parameters of the reaction model.

Parameter	Value	Meaning
k_1	$3.14 \times 10^5 \text{ mbar}^{-1}$	Impingement rate of CO
k_2	10.21 s^{-1}	CO desorption rate
k_3	283.8 s^{-1}	CO reaction rate
k_4	$5.86 \times 10^5 \text{ s}^{-1} \text{ mbar}^{-1}$	Impingement rate of O_2
k_5	1.61 s^{-1}	Phase transition rate
s_{CO}	1.0	CO sticking coefficient
s_O	0.6	Oxygen sticking coefficient on the 1×1 phase
s_O	0.4	Oxygen sticking coefficient on the 1×2 phase
$u_0, \delta u$	0.35, 0.05	Parameters for the structural phase transition
D	$40 \text{ } \mu\text{m}^2 \text{ s}^{-1}$	CO diffusion coefficient
u_{ref}	0.3358	Reference CO coverage

Chapter 4

Ultra-thin Platinum foil

A temperature increase ensuing from an exothermic reaction may dominate the course of a heterogeneous catalysis experiment, even if performed in a controlled environment at atmospheric pressures. This is especially relevant in the case of nonlinear chemical systems that exhibit oscillatory behavior, where the reaction conditions play a delicate role in the system dynamics (as shown in chapters 2 and 3). The indicated temperature effects can determine the spatiotemporal pattern formation observed in the surface reactions [103, 174, 175, 176, 177]. The problem of distinguishing whether temperature changes were due to nonlinear effects or to intrinsic features of the reaction mechanism gained the attention of G. Ertl and co-workers; for their investigations they used the well known CO-oxidation on single crystal surfaces under isothermal conditions and low partial pressures [104]. A number of surface patterns have been discovered under these well defined reaction conditions for the CO-Pt system (section 2.1). To accurately infer whether these patterns and their evolution stem from minor temperature changes, we need a method independent of the reactant pressures, that allows a precise measure of the adsorption and reaction heat. The present chapter seeks to explain why the use of an ultra-thin platinum foil can be a solution to this problem, and how the foil can be used as a micro-calorimetric technique.

An ultra-thin self-supporting platinum foil, 300 nm thick and 4 mm in diameter, has a heat capacity of only $10 \mu\text{J/K}$. It does not have enough mass to dissipate the reaction heat generated at its surface; even small amounts of heat deposited within the thin metal foil

cause a significant temperature increase. The resulting thermo-elastic stress in the metal leads to macroscopic deformations of the foil. A quantification of these deflections was achieved with a Michelson interferometer, and a topographical reconstruction algorithm, as will be shown in sections 4.1 and 4.7.

Samples with extremely low heat capacities were first used in the micro-calorimetric determination of the heat of adsorption of different gases on Ni and Pt single crystal surfaces in 1994 [78, 178, 179]. In addition, macroscopic oscillating deformations of an ultra-thin foil under reaction conditions at moderate pressures of 10^{-2} mbar, have been reported in [68, 180].

4.1 The sample and the setup

The key element of this chapter is the particular platinum sample used: a 300 nm thick Pt(110) single crystal foil, schematically shown in Fig. 4.1. The crystal sample was prepared by J. Chevallier at the Aarhus University, Denmark. It was grown epitaxially by evaporation onto the polished crystal surface of a radiation-hardened NaCl single crystal, previously annealed at ~ 800 K, at growth rates of $10 - 20 \text{ \AA} \cdot \text{s}^{-1}$ and at a substrate temperature of $600 - 700$ K. The NaCl was subsequently dissolved in water to leave the metal crystal floating on the water, supported by surface tension. A polycrystalline Pt support ring with a 4 mm inner diameter, etched in a hot acid mixture to remove any surface oxide, and then rinsed clean in distilled water, was used to lift the crystal off the water. Finally, gentle pressure was applied to expel the water from between crystal and ring and pull the thin film taut and flat, resulting in a permanent cold weld giving good mechanical support and electrical contact [79].

A Michelson interferometer enables us to characterize the topography of the foil after deformation through heat deposition. The corresponding interferogram fringes are recorded by a 2048×2048 pixels, 16 bit digital CCD camera at a maximum rate of 10 video frames per second (fps) and stored on a Sun workstation. A spatial linear-carrier method is then used to obtain the surface profile of the Pt foil, as explained in section 4.7 and [181, 182].

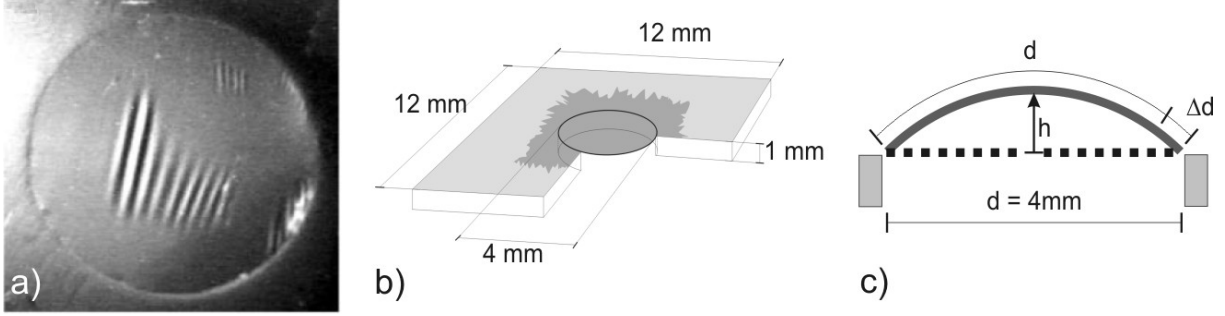


Figure 4.1: a) photo [68] and b) sketch of the ultra-thin Pt foil [69]. c) schematical representation of the foil expansion [42].

The sample is placed in a UHV chamber very similar to the one presented in section 2.4.6.1. It has a base pressure of 10^{-10} mbar and is also equipped with an Ar-ion sputterer for sample preparation and LEED for surface analysis. A dosing system allows for precise dosing of CO and oxygen, and the sample holder can be heated by a halogen lamp. Besides that, two laser beams (continuous and chopped) are used to heat the Pt foil independently. A sketch of the setup is shown in Fig. 4.2.

Fig. 4.3 a) displays a typical interferogram of the Pt foil obtained with this setup. The so-called contour line interferogram does not provide the complete information necessary for reconstruction of the topography. Therefore, the reference mirror of our setup is tilted horizontally by about two tenths of a degree, which results in an interferogram like the one shown in Fig. 4.3 b). A regular pattern of slightly distorted vertical stripes is then observed. Variation in sample topography changes the distortion of the stripe pattern shown in (Fig. 4.3 c)). The distortion can be analyzed with the help of a computer program and the surface profile can be reconstructed (Fig. 4.3 d) to e)). As a measure of the deformation of the sample, the expansion of the Pt foil perpendicular to the buckling in Fig. 4.3 is calculated from the change of the arc length of the curve shown in Fig. 4.3 e) compared to the length of the curve for a plain surface. Computational analysis of the fringes becomes problematic at extreme deformations, and it is consequently not possible to measure foil expansions above a critical value (see Fig. 4.4).

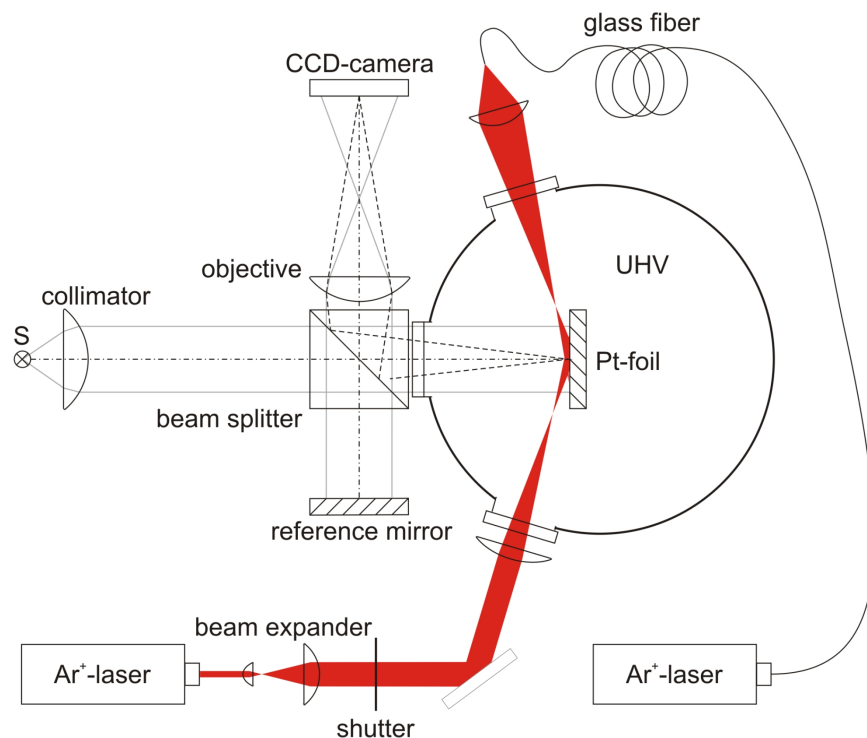


Figure 4.2: Sketch of the experimental mounting: essentially a Michelson interferometer [69].

The mechanical pre-strain on the Pt foil caused by a temperature difference between the foil and the substrate [68] has to be taken into account in the experiments with this setup. Due to thermal radiation, the Pt foil permanently exchanges heat with its environment. At elevated temperatures this leads to a temperature difference between the foil and the substrate, because the radiative heat losses of the foil cannot be compensated by heat conduction from the foil boundaries, and temperature equilibrium cannot be achieved through the gas phase. Thus, the temperature in the center of the foil decreases and the thermal expansion is smaller than that of the substrate, tightening up the foil. This pre-strain restrains the mechanical response of the Pt foil to any heat effect and should therefore be reduced to make the effects induced by adsorption and reaction of CO and oxygen visible. This is achieved by continuously focusing laser light onto the Pt foil. As a result, the temperature of the foil is increased, the foil expands, and the strain is reduced. Furthermore, the pre-strain exhibits a strong anisotropy caused by the heterogeneity of ring fixation of the Pt foil. This is the origin of the rather complicated

topography of the buckled surfaces. The sample does not deform homogeneously but shows ripples which are oriented parallel to the strongest strain (Fig. 4.1 a) and 4.3 d)). This was already observed and analyzed in earlier studies [68]. Generally, the sensitivity of this setup is the highest in the case of a homogeneous deformation (see section 4.7). However, the method of analysis is independent of the respective buckling mode and also works when applied to complicated patterns.

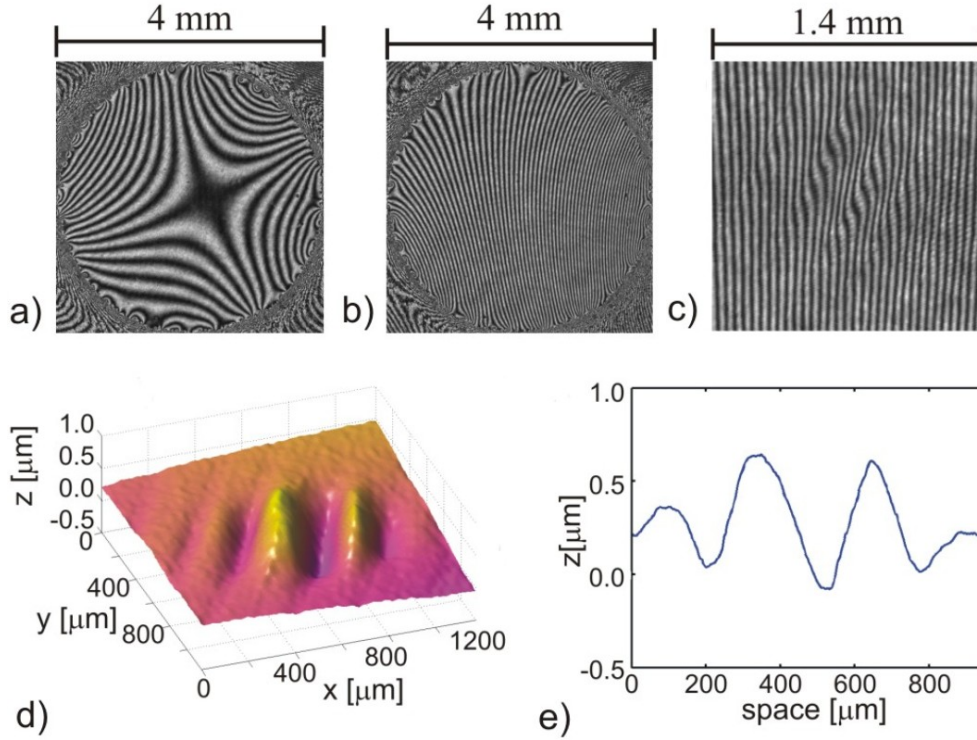


Figure 4.3: Interferogram fringe patterns and calculated surface profile. a) contour line interferogram, b) interferogram of the flat Pt foil with tilted reference mirror, c) magnified interferogram of a buckled Pt foil being irradiated by laser light with a power of 4.91 mW ($T_{UHV} = 419$ K), d) reconstructed topography from c), and e) cut perpendicular to the wrinkles shown in d) [69].

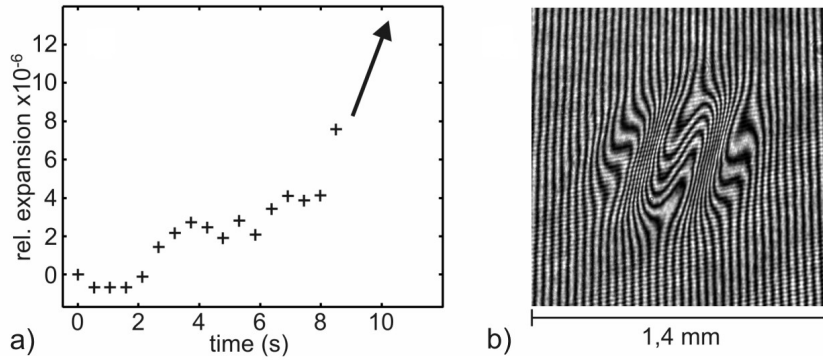


Figure 4.4: a) foil expansion out of measure range. b) corresponding fringes pattern: too distorted for the topographic reconstruction method [42].

4.2 Calibration

To quantitatively characterize the thermal effect on the sample and to properly relate the corresponding foil deformation with the adsorbed heat, the system has to be calibrated. The strategy followed is to match the foil expansion with known amounts of heat released on it by a laser light; this idea was already used in the groups of King [79] and Campbell [183, 184, 185]. However, in the first attempts to measure the sample expansion under reaction conditions, a proper calibration had not been performed. For this reason the experimental results presented in the following are still of a qualitative character.

Using solely the continuous laser beam to change the temperature of the Pt foil produces changes in the topography (as shown in Fig. 4.1 or 4.3). No deformation of the foil is observed until a certain laser power is reached. The magnitude of this threshold power depends on the substrate temperature, hence, on the pre-strain of the foil. At a substrate temperature of $T = 419$ K (512 K) deformation started at a laser power of 3.8 mW (4.55 mW). These data reveal the temperature dependence of the pre-strain that conditions the foil's thermal expansion.

As *ex situ* measurements with our Pt foils have shown [42], a fraction of 36 % of the laser radiation is absorbed by the Pt foil. Thus, a laser power of 3.8 mW (4.55 mW) corresponds to an absorbed power of 1.35 mW (1.62 mW). A further increase of the laser power (both for $T = 419$ K and $T = 512$ K) of 0.05 mW (18 μ W absorbed) results in a

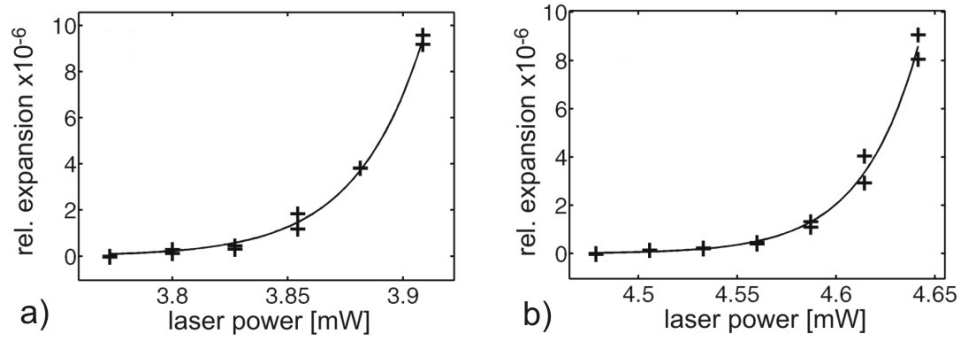


Figure 4.5: Relative expansion of the Pt foil as a function of the incident laser power. a) $T = 419$ K, b) $T = 512$ K [69].

relative expansion of around 10^{-6} . When this state is reached, an increase of yet another 0.05 mW causes an expansion in the order of 10^{-5} . Thus, a surface reaction that releases 18 μ W of heat into the Pt foil, will cause some sample deformation. This is the same amount of heat that is released when CO is oxidized on top of the Pt foil at a reaction rate of 0.5 ML/s (9×10^{-11} mol/s) [78]. For all subsequent experiments, the sample is illuminated by continuous laser light with a power slightly below the deformation threshold, so that even small amounts of additional heat can produce a detectable deformation of the foil.

To further improve the calibration, a short, well defined laser pulse is applied. Its duration is controlled by the shutter shown in Fig. 4.2. Consequently, an expansion of the foil corresponding to a short temperature increase can be measured. Fig. 4.6 a) to e) show the heat induced expansion for different shutter times. During the measurement presented in 4.6 a) about 15 μ J of heat are released within a time interval of 1/15 seconds. For pulses longer than 0.5 seconds a saturation of the change in topography can be observed. The same behavior is arrived at in numerical simulations of the thermal properties of our Pt foil (Fig. 4.6 f)).

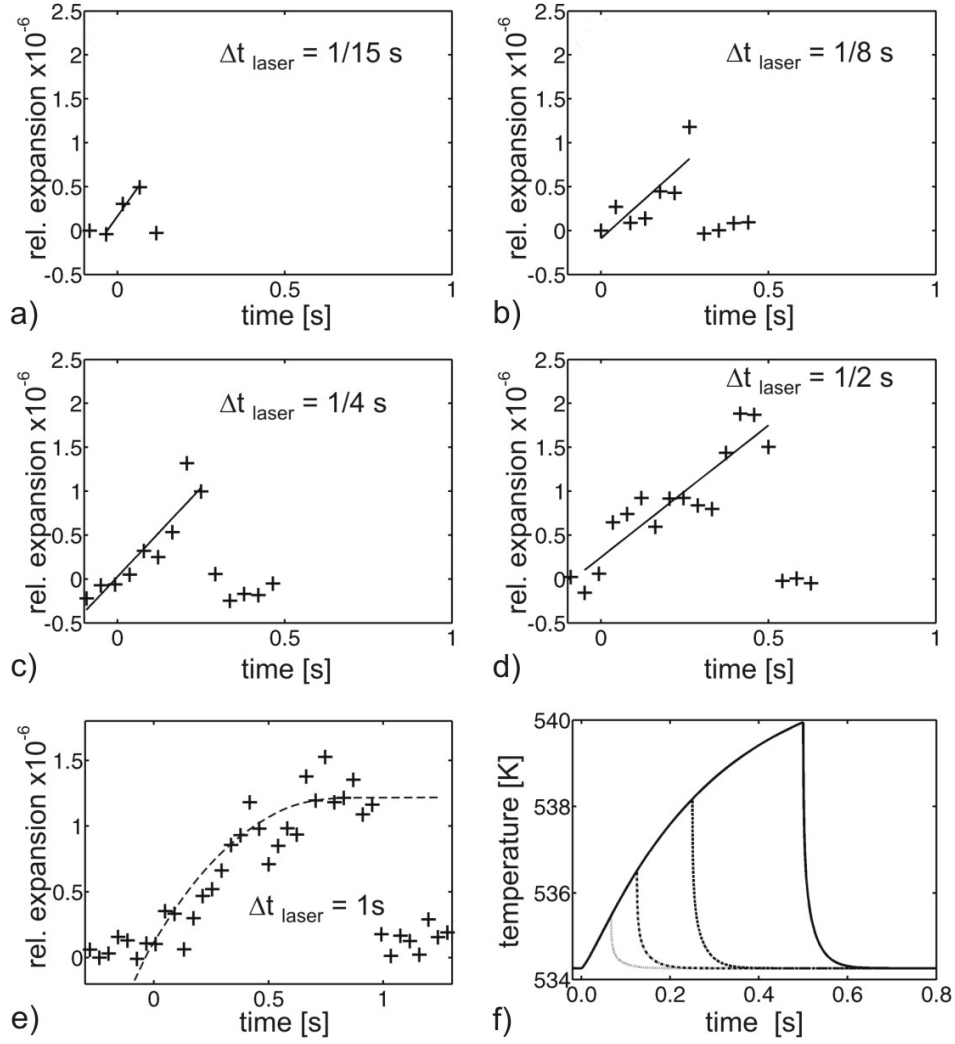


Figure 4.6: Relative expansion of the Pt foil due to the irradiation with a chopped laser light. $P_{\text{laser-pulse}} = 0.61 \text{ mW}$, $T = 478 \text{ K}$. a) to e) experimental data, f) numerical simulation of the temperature response [69].

4.3 Titration experiments

The experimental setup and the topographic methods have already been presented in previous sections. Now, the CO₂ formation comes into play and two particular cases of titration on a catalytic surface are presented.

4.3.1 Reaction of oxygen with preadsorbed CO

The titration experiment illustrated in Fig. 4.7 was performed as follows: first, the sample was exposed to a CO pressure of 10^{-5} mbar for about 60 seconds. The sample heating by continuous laser light was adjusted in such a way that the foil rested slightly below the buckling threshold (corresponding, for example, to 4.5 mW laser power in Fig. 4.7 b)). Then the CO valve was closed, leaving a CO covered Pt crystal in the UHV chamber, and the oxygen valve was opened ($t = 0$ s in Fig. 4.7 a)). This procedure leads to a clear mechanical response of the foil: initially the relative deformation of the Pt foil is zero, but after approximately 3 s the deformation abruptly increases, to decay 2 s later down to a constant value of about 0.5×10^{-6} . This mechanical behavior of the foil is due to the chemical exothermic processes taking place on its surface. After the oxygen valve has been opened, the catalytic reaction cannot start immediately because the Pt surface is poisoned with CO [13]. Three seconds later, the reaction starts up. Oxygen is adsorbed and reacts with the adsorbed CO molecules. This process releases heat which is partly absorbed by the catalyst. The resulting small temperature increase causes thermo-elastic stress which leads to the deformation of the foil (Fig. 4.7 c) and f)). In the end, the Pt foil is covered with oxygen. The deformation does not vanish completely but remains at a small and fixed value (Fig. 4.7 d) and g)). The reason is that the optical properties of the oxygen covered platinum surface differ from the properties of the CO covered crystal.

To summarize, two mechanisms determine the mechanical response of the Pt foil. First, the catalytic reaction increases the sample temperature because reaction heat is released. And second, due to adsorption of oxygen, the absorption coefficient of the Pt foil increases (about 2 %). More laser light is absorbed and therefore the sample temperature raises.

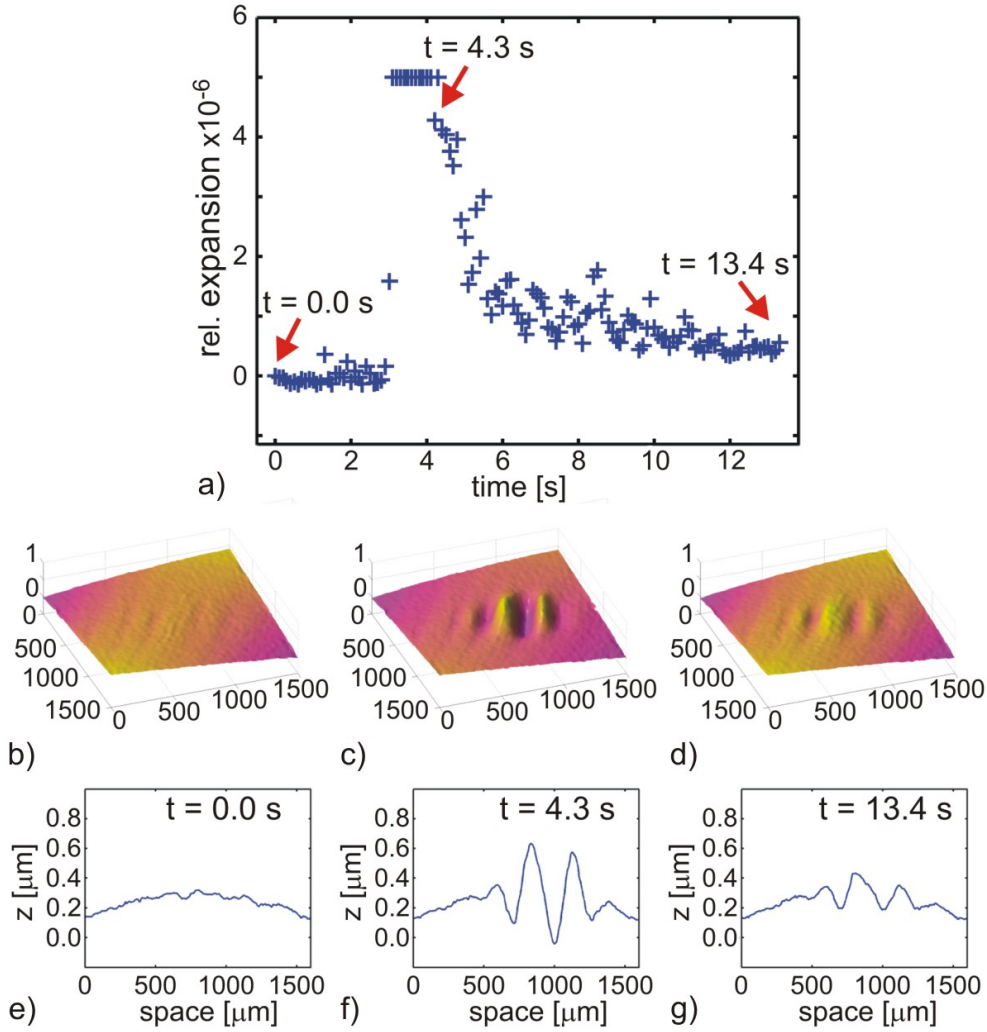


Figure 4.7: Titration experiment. $T = 482 \text{ K}$, $P_{\text{laser-pulse}} = 4.5 \text{ mW}$. At $t = 0 \text{ s}$ the crystal surface was CO covered and the oxygen valve is opened, $p_{\text{O}_2} = 10^{-3} \text{ mbar}$. a) relative expansion, b) to d) snapshots of the reconstruction of the surface profile at the time moments indicated in a). e) to g) are cuts through b) to d). A relative expansion larger than 5×10^{-6} at around 3 - 4 s could not be analyzed with the used algorithm. In this case the algorithm did not produce reasonable results and a fixed value of 5×10^{-6} was assigned to images with larger expansion [69].

4.3.2 Reaction of CO with preadsorbed oxygen

In this case, the resulting deformation happens on a shorter time scale because the Pt surface is not poisoned and the reaction starts immediately when the oxygen covered sample is exposed to CO. The transition from a buckled to an unbuckled surface can be observed in Fig 4.8. The reaction speed is higher than the sampling rate, which makes visible no sign of the exothermic reaction.

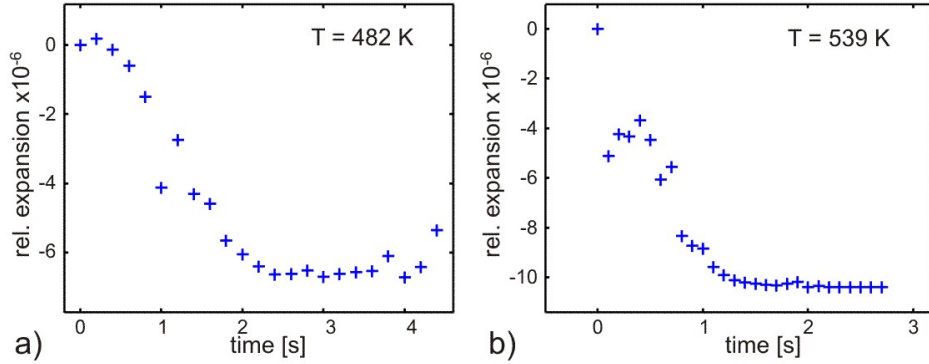


Figure 4.8: Titration experiment. a) $P_{laser-pulse} = 4.5$ (4.69) mW and b) $P_{laser-pulse} = 5.14$ (5.46) mW. At $t = 0$ s the crystal surface was oxygen covered and the CO valve is opened, $p_{CO} = 10^{-5}$ mbar [42].

4.3.3 Parameter dependence of the titration

Fig. 4.9 and 4.10 show how the contributions of the two mechanisms above explained changes when the reaction parameters are modified. At high oxygen pressure during titration of CO, the reaction heat dominates the mechanical response of the catalytic foil and a fast pronounced deformation peak is observed (Fig. 4.9 a)). With decreasing pressure, the deformation peak becomes broader (note the different time scales in the plots) and smaller in comparison to the permanent deformation induced by the laser heating (Fig. 4.9 b) to d)). When the same experiment is performed at higher temperature (Fig. 4.10), the result is qualitatively the same. If Fig. 4.9 and 4.10 are compared,

it can be seen that the permanent relative deformation of the oxygen covered foil differs because the power of the heating laser is not the same; indicated in the figure caption, different laser power was used in order to optimize the visibility of the reaction topographic effects.

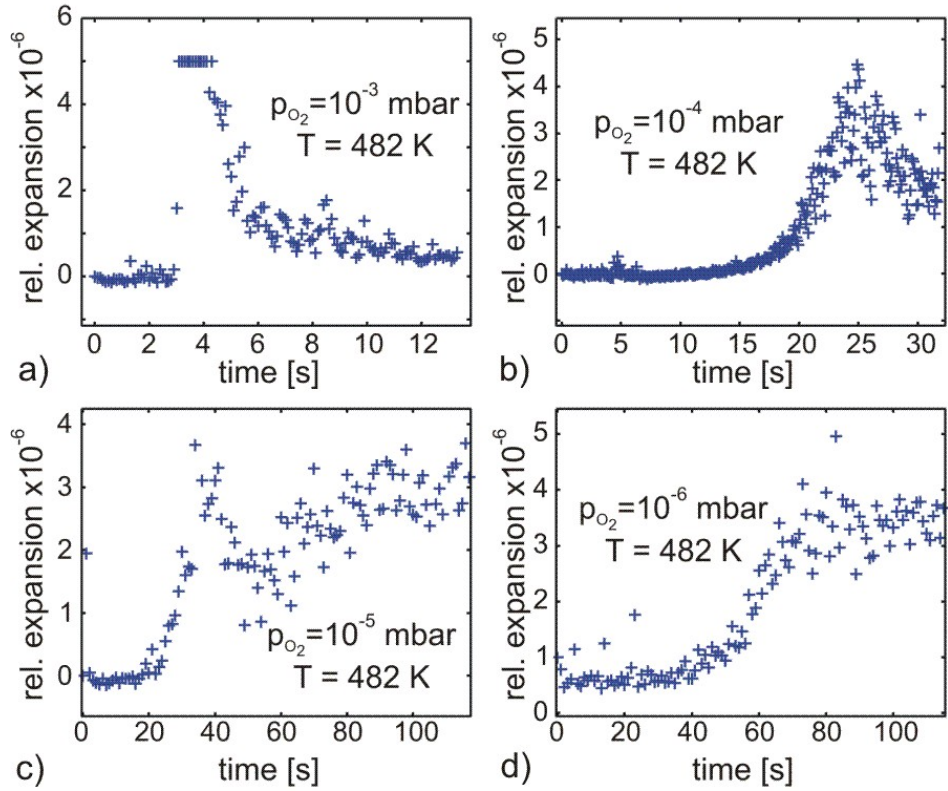


Figure 4.9: Relative expansion of the foil during titration of CO. a) $P_{laser} = 4.37$ (4.49) mW. b) $P_{laser} = 4.49$ (4.63) mW. c) $P_{laser} = 4.51$ (4.69) mW. d) $P_{laser} = 4.69$ (4.80) mW. The power of the heating laser is adjusted to a value slightly below the buckling threshold (value in brackets) [69].

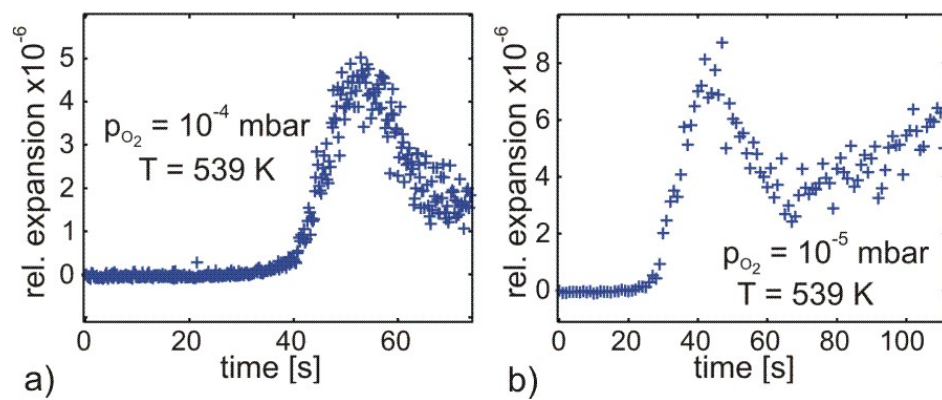


Figure 4.10: Relative expansion of the foil during titration of CO. a) $P_{laser} = 5.14$ (5.37) mW. b) $P_{laser} = 5.14$ (5.46) mW. The power of the heating laser is adjusted to a value slightly below the buckling threshold (value in brackets) [69].

4.4 Pattern formation

During the titration of CO with oxygen, spatiotemporal patterns in the sample topography were observed at temperatures below 512 K. The effect is weak (deformations of few tens of nanometers), so that a background subtraction is needed to visualize the surface profile changes. For this, the first image of a sequence of surface profiles was stored in the computer and subtracted from all the following images. Consequently, the topography of the unperturbed Pt foil appears perfectly flat. Fig. 4.11 shows the propagation of a deformation front corresponding to the measurement shown in Fig. 4.9 b). The effect is visible as a small peak in the relative expansion around $t = 5$ s, and is shown in detail in Fig. 4.12. For lower temperature and lower oxygen partial pressure a deformation pulse can be seen (Fig. 4.13).

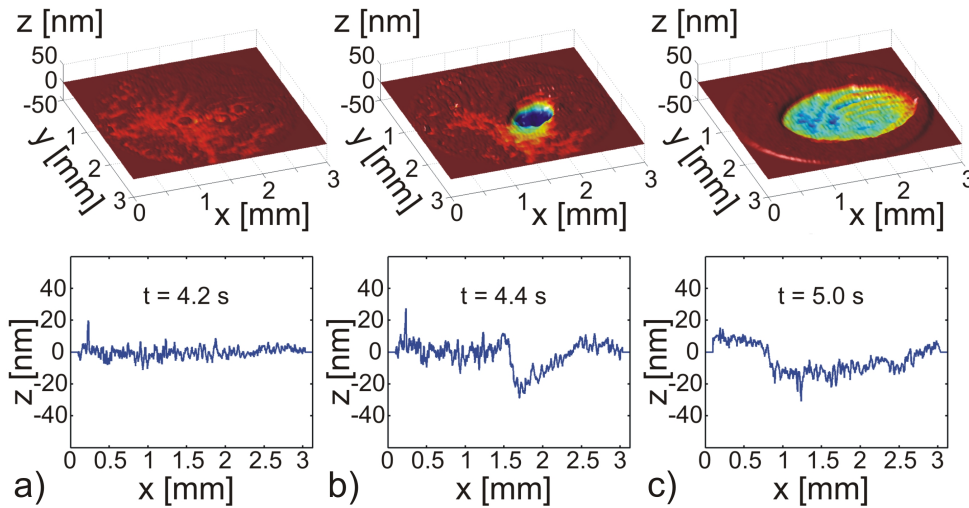


Figure 4.11: Propagation of deformation fronts. a) to c) representation of subsequent surface profiles reconstruction and the corresponding cuts at $T = 482$ K and $p_{O_2} = 10^{-3}$ mbar. The power of the heating laser is adjusted to a value slightly below the buckling threshold [69].

To explain the formation of patterns on the Pt surface, the following mechanism can be proposed: when the reaction starts, heat is released into the foil and the temperature increases locally. Heat is transported via heat conduction within the foil. This means

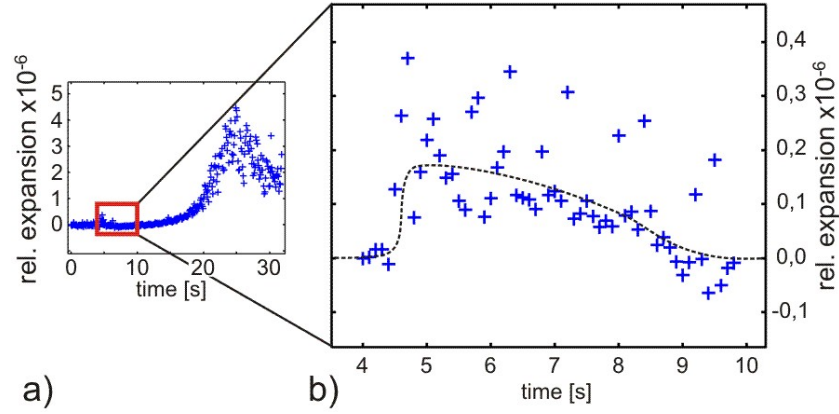


Figure 4.12: Detail of the relative expansion shown in Fig. 4.9 b), corresponding to the propagating front shown in Fig. 4.11 [42].

that the temperature also increases in the immediate surroundings of the nucleation site, so that the reaction is more likely to start there too. As a consequence, the reaction propagates, together with a pulse-shaped temperature heterogeneity, from the center of the foil to its boundary. Depending on the reaction conditions this process leads to a front-like or a pulse-like deformation, where the propagation velocity is determined by heat conduction and the reaction rate. At higher temperature and higher O_2 pressure (for instance $T = 482$ K and $p_{O_2} = 10^{-3}$ mbar), the reaction rate is higher and the front moves with a velocity of around 1.2 mm/s. At lower temperature and lower pressure (for instance $T = 420$ K and $p_{O_2} = 10^{-6}$ mbar), the propagation velocity of the pulse is lower. It is plausible that the patterns shape is also a parameter dependent feature. For slow temperature propagation, the spot origin of the reaction is more likely to release enough heat and recover its shape before the mechanical pulse reaches the border of the foil (giving a pulse like shape to the pattern), than if the temperature propagation is faster (remaining as a front).

In both cases (pulse and front) a coupling between the reaction dynamics and temperature heterogeneities may occur. In addition, the patterns always emerge in the center of the Pt foil. The reason might be that the intensity of the heating laser beam is at its maximum there, or because that is the spot where the foil has less structural tension, or most likely a combination of both.

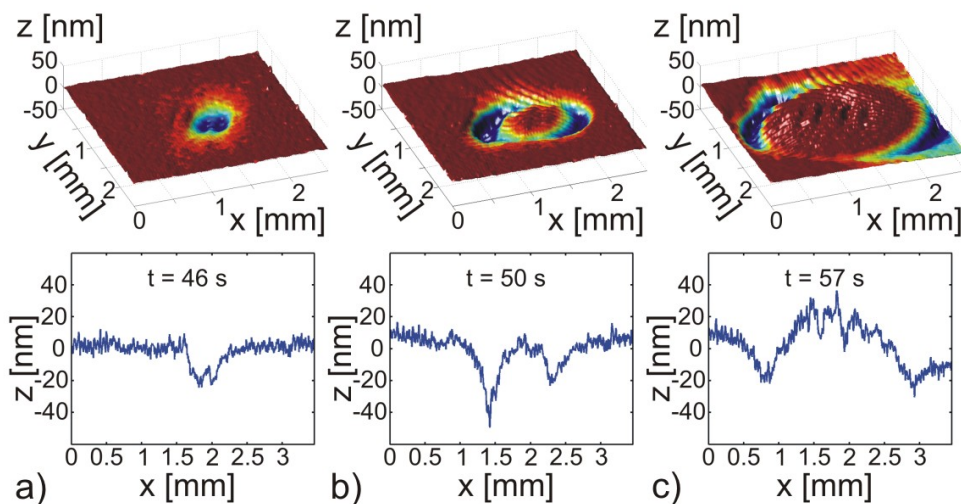


Figure 4.13: Propagation of deformation pulses. $T = 420$ K and $p_{O_2} = 10^{-6}$ mbar. The power of the heating laser is again adjusted to a value slightly below the buckling threshold [69].

4.5 Sensitivity of the method

The calorimetric method for direct measurement presented in this chapter can be properly described in terms of featured sensitivity. Let's first consider the geometry of the Pt foil as quasi one-dimensional with, for the sake of simplicity, a rectangular shape (as in Fig. 4.16). The thermal expansion of the sample results in a rippling of the foil: the ratio of the *arc* lengths of cuts through the ripple and the flat foil $(d + \Delta d)/d$ is the relative expansion of the crystal (Fig. 4.1 c) and 4.16 b)). Neglecting any cooling effects via heat conduction into the substrate, the relative expansion is proportional to the temperature increase of the Pt foil, with this proportionality factor given by the thermal expansion coefficient. Therefore, the relative expansion $(d + \Delta d)/d$ is used here for the graphical representation of the sample response.

The height of the ripple h (buckling amplitude) is a function of the thermal expansion of the Pt crystal, and thus, of the adsorbed energy which is released into the foil during the species adsorption or during titration. The dependence can be summarized in the

following two equations:

$$\Delta E = \frac{mc_p}{\alpha} \left(\frac{\varphi}{\sin \varphi} - 1 \right) \quad (4.1)$$

with

$$\varphi = 2 \arctan\left(\frac{2h}{d}\right). \quad (4.2)$$

Here, m is the mass of the self-supporting part of the foil, c_p is the Pt heat capacitance, α stands for the thermal expansion coefficient, and h and d are defined according to Fig. 4.1 c). The term $(\varphi/\sin \varphi - 1)$ is the relative expansion $(d + \Delta d)/d$. Using these equations, the amount of energy ΔE which has been released into the foil and has caused the thermal expansion, can be calculated from the value of h . In this approach, any thermomechanical transmission is neglected and temperature rise as well as mechanical deformation are assumed to occur instantaneously. Also, cooling via heat conduction into the substrate is not taken into account. The dependence of h on ΔE at room temperature is shown in Fig. 4.14 a) for a rectangular sample 4 mm x 2 mm x 0.5 μm .

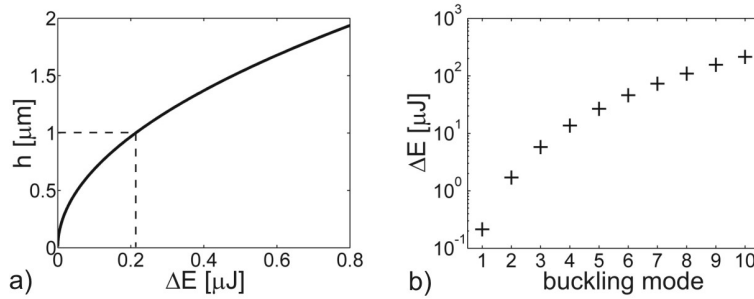


Figure 4.14: Theoretical sensitivity for a 4 mm x 2 mm x 0.5 μm sample. a) buckling amplitude as a function of the dosed energy. b) sensitivity for different buckling modes (see text). Energy necessary to cause a buckling amplitude h (see Fig. 4.1 c)) of 1 μm as a function of the mode number. The value of the first mode corresponds to the dashed lines in a). Thermal expansion coefficient $\alpha = 8.92 \times 10^{-6}$, heat capacity $c_p = 133 \text{ J kg}^{-1} \text{ K}^{-1}$ and density $\rho = 21.45 \text{ g/cm}$ [69].

Using an interferometer, buckling amplitudes (h) of 1 μm can be measured. To generate a buckling amplitude of 1 μm , 0.21 μJ of heat has to be absorbed by the foil

(dashed lines in 4.14 a)). This amount of heat is released, when 720×10^9 molecules of CO adsorb on the Pt surface instantaneously (adsorption enthalpy $H_{CO} = 175$ kJ/mol [76]. As one monolayer (ML) of CO on the Pt(110) single crystal surface (8 mm^2) consists of about 74×10^{12} molecules, the calculated amount of $0.21 \text{ } \mu\text{J}$ of heat would be released by an instantaneous adsorption of 1×10^{-2} ML of CO. A buckling amplitude of, let's say, 100 nm (i.e., 2.1 nJ absorbed energy) will be caused by adsorption of only 1×10^{-4} ML of CO. This detection limit for coverage could be improved by at least one order of magnitude with the use of a state-of-the-art interferometry [186] and thinner Pt foils.

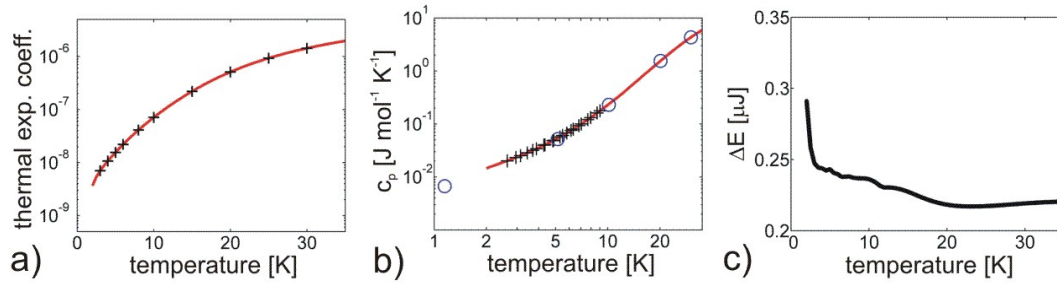


Figure 4.15: Theoretical sensitivity at low temperatures for a sample geometry shown in Fig. 4.16. a) thermal expansion coefficient of platinum as a function of temperature, after [187]. b) molar heat capacity as a function of temperature, “O” data after [188], “+” data after [189]. The red lines indicate spline fits to the experimental data used for further calculations. c) energy necessary for a buckling amplitude of $1 \text{ } \mu\text{m}$ calculated from the fitted red curves in a) and b) using the equations in appendix 4.7, foil dimensions $4 \text{ mm} \times 2 \text{ mm} \times 0.5 \text{ } \mu\text{m}$ [69].

So far, the Pt foil was assumed to buckle homogeneously, as indicated in Fig. 4.1 c). What happens if higher deformation modes are present? Like in the case of guitar strings, the wavelength of the buckling can be any integer fraction of the foil length d . If we number the buckling modes like the harmonics of a tone, and calculate the amount of energy necessary to produce a buckling amplitude of $1 \text{ } \mu\text{m}$ in the respective mode, we get the diagram shown in Fig. 4.14 b), in which the sensitivity is maximum for the first buckling mode and then decreases.

4.6 Discussion

In this chapter a new method for direct calorimetric measurement of adsorption energies is presented, which has clear advantages over “conventional” techniques. Traditional methods are indirect and rely on desorption, e.g., thermal desorption spectroscopy or measuring isosteric heat. Although these techniques have proven to be effective for many traditional reversible adsorption systems, they are only useful if the adsorbates do not form another high-temperature phase at the desorption temperature, namely the adsorbates dissociate, form clusters, diffuse into the bulk or react with co-adsorbates [190]. Direct calorimetric measurements of adsorption heat evade this limitation. Of course, the present work [69] is still only a feasibility study, as it has not yet been fully calibrated for use in differential calorimetry. However, this should be straightforward using the techniques developed by King and Campbell. Even without calibration, the technique can be used to measure relative reaction rates. Combined with the spatially resolving topographic detector, this may ultimately prove to be useful for spatially resolving relative reaction rates on heterogeneous samples or even as a detector in combinatorial chemistry [191].

This setup is based on the interferometric determination of topographical changes of an ultra-thin reflective foil. Sample thicknesses between 0.1 and 5 μm may be used. The theoretical detection limit of our setup as applied to CO coverage (energy) lies in the order of 10^{-5} ML (2 nJ) (section 4.5).

The method can be applied to experiments in a broad range of parameters. The sample can be annealed at high temperatures, since no heat-sensitive components are used in. The system theoretically operates at temperatures down to 2 K without loss of sensitivity (see Fig. 4.15). Between room temperature and 3 K the sensitivity does not change significantly and only decreases rapidly at temperatures below 2 K. By contrast to Campbell’s method [183, 184, 185], where the signal is dependent on the time derivative of the sample temperature, this setup allows for measuring constant reaction rates, since the output signal (mechanical deformation) is directly dependent on the sample temperature. Furthermore, it is not restricted to UHV conditions.

Table 4.1 provides a general comparison of the exposed interferometric approach with methods based on infrared detection (King and co-workers [79]) and methods based on the pyroelectric effect (Campbell *et al.* [183, 184, 185]).

Table 4.1: Properties of the method proposed in this work (first column) compared with the methods used by Campbell [183, 184, 185] and King [79].

Method	Interferometry	Pyroelectric detection (Campbell)	IR detection (King)
Detection limit (energy)	$< 2 \text{ nJ}$ (calculated)	$< 100 \text{ nJ}$	$< 100 \text{ nJ}$
Working temperature range (theoretical)	$> 2 \text{ K}$	2 K- 400 K	$> 100 \text{ K}$
Sample thickness	0.1-5 μm	0.1-10 μm	$\approx 0.2 \mu\text{m}$
Annealing at high temperatures	Yes	Yes	No
Dependence on temperature	$\propto \Delta T$	$\propto d(\Delta T)/dt$	$\propto \Delta T$

The detection limit of our interferometric approach is only a rough theoretical estimate, while the values of the other two methods are deduced from experimental results. Reproduced from [69].

Some improvements of the design are still needed to develop this method into a quantitative tool for reaction rate and calorimetric measurements. Both, resolution and working range could be increased if a more complex setup together with a more sophisticated algorithm was used. The coverage of the surface with oxygen or CO could not be measured during the interferometric experiments because the space in front of the sample was occupied by the laser used for heating and the interferometer. Since laser heating is only necessary because of the mechanical pre-strain of the sample, a removal of the mechanical pre-strain would make the heating laser redundant. In that case, there would be space for additional surface analysis, like ellipsomicroscopy, and the mechanical response of the foil would no longer be influenced by the change of the optical properties due to adsorption of the reaction products. The latter can also be achieved by heating with laser radiation from the back of the sample, using a coated foil with optical properties independent of the coverage on the illuminated side.

Using quantitative ellipsometry and a molecular beam, the absolute coverage of the Pt crystal could in principle be measured directly and used for accurate system calibration. To perform this measurement with sufficient accuracy, a flat sample would be needed, because the angle of incidence has to be defined with an accuracy of at least a few tenths of a degree. A possible way would be adsorbing a fraction of a monolayer using a molecular beam. The surface would buckle due to the released reaction heat, and would again unbuckle when the crystal foil has cooled down via heat conduction into the substrate. If no thermal desorption of the adsorbed species occurs at the given conditions, the coverage could then be measured, matching buckling amplitude with coverage and released heat.

An alternative sample setup (Fig. 4.16) has also been proposed [69]. The Pt foil is evaporated on a piezo-crystal with a trench filled with sodium chloride or a lacquer. After evaporation of platinum the substance filling the trench is dissolved, and a self-supporting Pt film remains. Any pre-strain occurring during the experiment can now be compensated by applying an appropriate voltage to the piezo-crystal. Thus, no laser illumination during adsorption experiments is needed, and the change of the optical properties of the Pt foil due to adsorbed species could be compensated. In combination with a molecular beam, this setup should have a sensitivity of a few nJ. Furthermore, it is possible to use polycrystalline samples selected according to the investigated reaction, which paves the way for inexpensive practical applications.

A faster image processing CCD camera would also mean a better characterization of the fast titration experiments, allowing a more precise time profile of the foil topography changes. The reconstruction algorithm also has some limitations, related in particular to the strong distortion of the interferogram fringes. The combination of two algorithms, one for small expansions (the actual one) and another for large expansions, could be a solution.

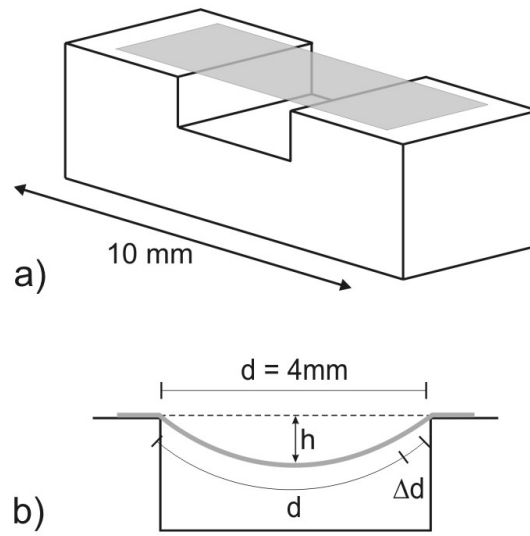


Figure 4.16: Proposed setup and sample geometry. a) the Pt foil is mounted on a piezo-support. b) thermal expansion causes a deformation of the sample; the ratio $(d + \Delta d)/d$ is the relative expansion of the foil, while h is the buckling amplitude.

4.7 Appendix: algorithm for the topography reconstruction

The algorithm used for the reconstruction of the sample topography was first proposed by Takeda *et al.* in 1982 [181]. Fig. 4.17 illustrates the basic principles of the method, which extracts the phase information encoded into the interferogram in form of bending of the fringes. The uniform spacing between parallel fringes is lost when the fringes are deformed, generating localized areas of compressed and expanded fringe spacing. Scanning across these areas would reveal changes in the fringe frequency corresponding to the change in fringe spacing. By extracting this fringe frequency from the dominant carrier frequency the phase information is isolated; this is achieved using a Fourier transform.

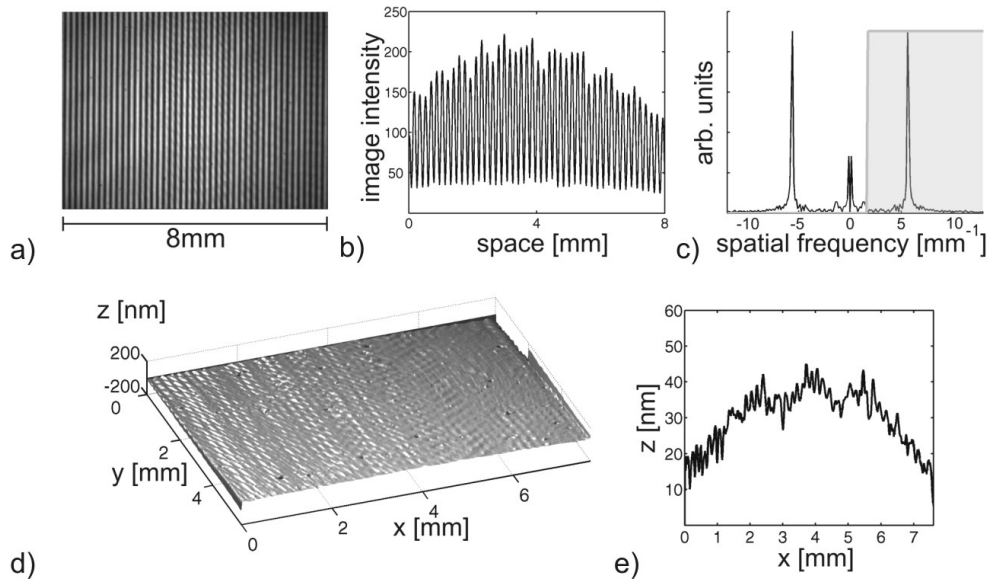


Figure 4.17: Reconstruction of the surface profile of a plane mirror. a) interferogram, b) horizontal cut through a), c) spatial frequency spectrum of b) where the shaded area represents the chosen frame of the spectrum used for the reconstruction of the topography. d) shape of the mirror surface and e) a cut through d).

The two dimensional intensity distribution $g(x,y)$ of an interferometric image can generally be written in the following form:

$$g(x, y) = a(x, y) + b(x, y) \cos \phi(x, y) . \quad (4.3)$$

Here, $a(x,y)$ denotes an (undesired) background intensity, $b(x,y)$ represents the space dependent amplitude of the interference pattern and $\phi(x,y)$ stands for the phase difference between the object wave (reflected by the Pt foil) and the reference wave (reflected by the plane mirror). The phase difference carries the information about the topography of the foil. But without knowledge of $a(x,y)$ and $b(x,y)$ the reconstruction of the phase from only one interferogram is impossible. This is why phase stepping techniques are usually applied. In our experiment this is not possible, because the surface profile changes too quickly; we have to reconstruct the topography from only one image. In their 1982 paper [181] Takeda *et al.* suggest to tilt the reference mirror with respect to one axis of the image in order to solve this problem (see Fig. 4.3). When this is done, the intensity in the interferometric image can be written as

$$g(x, y) = a(x, y) + b(x, y) \cos (2\pi f_0 x + \phi(x, y)) \quad (4.4)$$

where f_0 is the mean spatial frequency of the interference stripes caused by tilting the mirror. The interferometric image of a plane mirror (instead of the Pt foil) using a tilted reference mirror is shown in Fig. 4.17 a). The horizontal cut through the image is visible in Fig. 4.17 b). Since the mirror is flat, the stripe pattern is regular, but the amplitude of the interference pattern is not homogeneous and decays towards the boundaries of the image. The tilt introduces a carrier frequency for the information about the surface topography. Thus, the shape of the sample is now encoded in a frequency modulated form in the sequence of the interference stripes in the image. This becomes more obvious when we rewrite the above formula in a complex notation and perform a Fourier-transformation with respect to the tilted x-axis:

$$g(x, y) = a(x, y) + c(x, y) \exp (2\pi i f_0 x) + c^*(x, y) \exp (-2\pi i f_0 x) \quad (4.5)$$

where

$$c(x, y) = \frac{1}{2} b(x, y) \exp (i \phi(x, y)) . \quad (4.6)$$

And after the Fourier transformation:

$$G(f, y) = A(f, y) + C(f - f_0, y) + C^*(f + f_0, y) . \quad (4.7)$$

The spectrum of the intensity distribution is divided into three parts: the Fourier transform of the background intensity $A(f,y)$ and the Fourier transforms of $c(x,y)$ and $c^*(x,y)$ with one shifted to $+f_0$ and the other to $-f_0$ in the frequency domain. This can be seen in Fig. 4.17 c) where C and C^* correspond to the two peaks located at $\pm 5.75 \text{ mm}^{-1}$. The information about the topography of our sample is completely contained in the term $C(f-f_0,y)$. It follows that $G(f,y)$ can now be filtered without loss of (desired) information by subtracting $A(f,y)$ and $C^*(f+f_0,y)$ and shifting $C(f-f_0,y)$ back to zero:

$$\tilde{G}(f,y) = C(f,y). \quad (4.8)$$

This is done numerically by setting all stored values of G outside a given window around $+f_0$ to zero and shifting the resulting array by $-f_0$. The window used for the reconstruction of the topography in our example is indicated by the light gray shading in Fig. 4.17 c). In practice there is an overlap between the different parts of the Fourier spectrum. This restricts the spatial resolution of this method. The separability increases with larger tilt of the mirror (i.e., higher value of f_0), but is limited by the resolution of the CCD-camera because the interference stripes have to be sampled with sufficient accuracy. From $\tilde{G}(f,y)$ the surface profile $z(x,y)$ can be calculated:

$$\begin{aligned} \tilde{g}(x,y) &= \frac{1}{2}b(x,y) \exp(i\phi(x,y)) \\ \ln(\tilde{g}(x,y)) &= \ln\left(\frac{1}{2}b(x,y)\right) + i\phi(x,y) \\ \Rightarrow \phi(x,y) &= \Im\left\{\ln(\tilde{g}(x,y))\right\}. \end{aligned} \quad (4.9)$$

Now the information about the surface profile is no longer affected by interfering background heterogeneities and amplitude variations.

Chapter 5

Pitting corrosion on stainless steel

Already introduced in section 2.5, pitting corrosion on stainless steel is a particularly interesting and very common kind of metal corrosion. Apart from the localized loss of metal thickness, corrosion pits can also be stress raisers and the cause of a great deal of damage; huge losses every year are attributed to the pitting corrosion, and not just economic (*) but also human losses (**). Pitting is considered to be more dangerous than uniform corrosion because it is more difficult to detect, predict, and design against; for this purposes, surface imaging plays a prominent role [192], specially those techniques that are able to provide real-time information about an on-going process [14].

The nucleation of individual pits is strongly dependent on the state of the protective metal oxide layer, with inclusions, defects, and grain boundaries as the weak spots where the reactions normally begin. It is also well known that pits have a destructive influence on their vicinities through the release of aggressive ions, which enables the use of stochastic reaction-diffusion models [193] to approach pitting behavior. Numerical simulations based on an autocatalytic reproduction of pitting sites anticipated a spreading of the corrosion process as a cooperative wave [21], and this pattern has been confirmed experimentally [15].

The importance of the pit morphology in spreading corrosion processes has been generally recognized. A number of two-dimensional statistical models have been developed to describe the morphological aspects of pitting corrosion, and it has been reliably established that the shaping of the holes has a close relation with the corrosion activity

[194, 195, 196, 197]. Also relevant is the current density, as it may enlarge the active surface in a fractal way [197, 198]. Although some work has been done, especially with aluminum [124, 199], there is still a lack of precise experimental data on pit morphology, required for the development and testing of more elaborated models. The present chapter is dedicated to a three dimensional characterization of pits involved in the stainless steel degradation process, combining AFM *in situ* experiments with SEM microscopy.

(*) *The NACE (National Association of Corrosion Engineers) estimated that for 1998, the total annual direct cost of corrosion in the U.S. was approximately \$276 billion (3.1 % of the US gross domestic product).*

(**) *For instance, in April 1992, a corroded gasoline pipeline caused a sewer explosion that killed 215 people and injured 1,500 more in Guadalajara, Mexico [131].*

5.1 AFM *in situ* experiments

An electrochemical cell is used to study the metal corrosion under controlled conditions: a stainless steel sample is immersed in a 0.05 M NaCl solution and a potentiostat establishes a potential difference between electrodes, while the current through the working electrode is monitored. The cell is a three electrode set up (see section 2.5.2) adapted for AFM microscopy (see section 2.5.2.3).

5.1.1 Electrochemical unit

Designed to perform electrochemical experiments with simultaneous AFM imaging, the *in situ* unit is a small teflon container that contains the electrolyte and the electrodes (Fig. 5.1). The working electrode is built by attaching the stainless steel sample to a copper disc with silver paste, which guaranties good conductance through the two pieces. The disc has an electrical connection from the bottom of the unit. The edge of the sample is covered with nail varnish and the copper disc is isolated with parafilm, so that once the teflon basin is filled with the solution only the top face of the stainless steel is left in contact with the liquid. A silver gauze in the form of half cylinder centered in the sample is used as counter electrode. The reference electrode is a coating-free tip of an

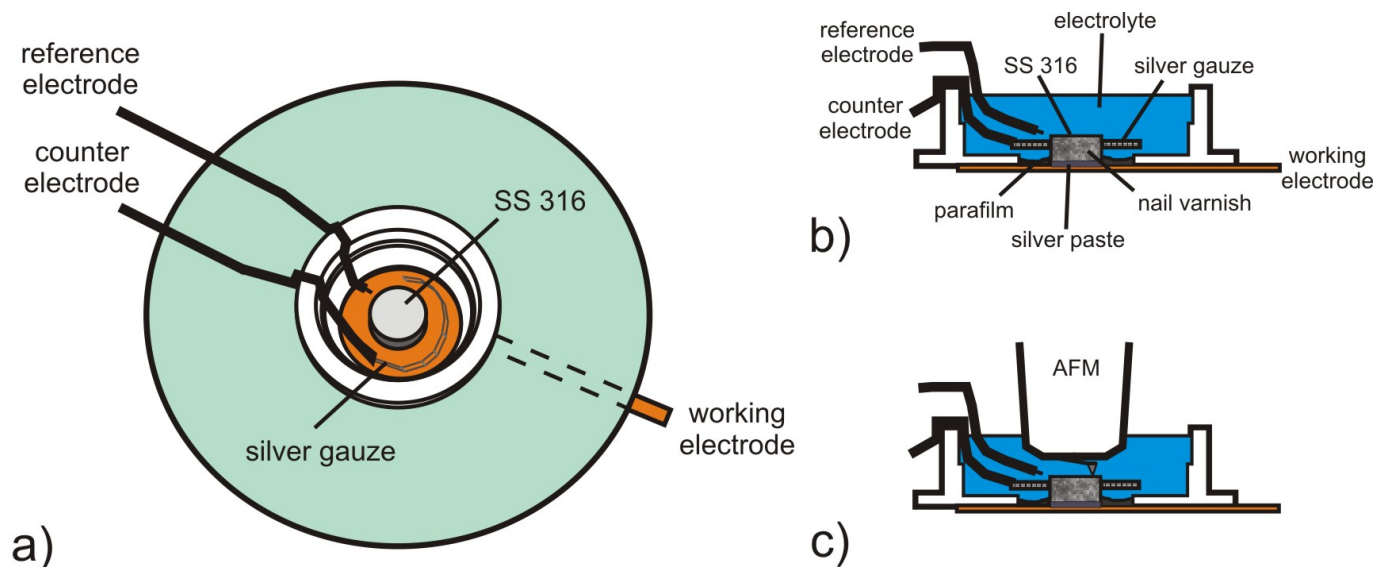


Figure 5.1: AFM *in situ* electrochemical cell.

enameled Cu (0.315 mm) wire placed close to the sample surface. The whole unit fits into the microscope, and after careful calibration of the cantilever in the fluid, the tip can scan the surface while the potentiostat controls the current through the system.

The mapping of the surface was performed in alternating cycles of electrochemical activity and an AFM scans (60 - 90 seconds per image). After every cycle the potentiostat would apply a higher potential for short time. For instance, the sequence corresponding to the experiments shown in section 5.2.1 is: surface scan, 0.1 V applied for 3 seconds, surface scan, 0.2 V applied for 3 seconds,... up to 0.8 V. These successive steps make it possible to follow the pit growth.

Events like the nucleation and growth of metastable pits can be identified in a current vs. time plot. Peaks and stepwise increase of the current are the result of partial ruptures of the protective cover, or the formation of new holes, assuming that the number and size of the holes must increase with time during pit growth [128, 200]. Fig. 5.2 compares the corresponding curves of a potential kept constant and of a constantly increasing potential applied to the cell.

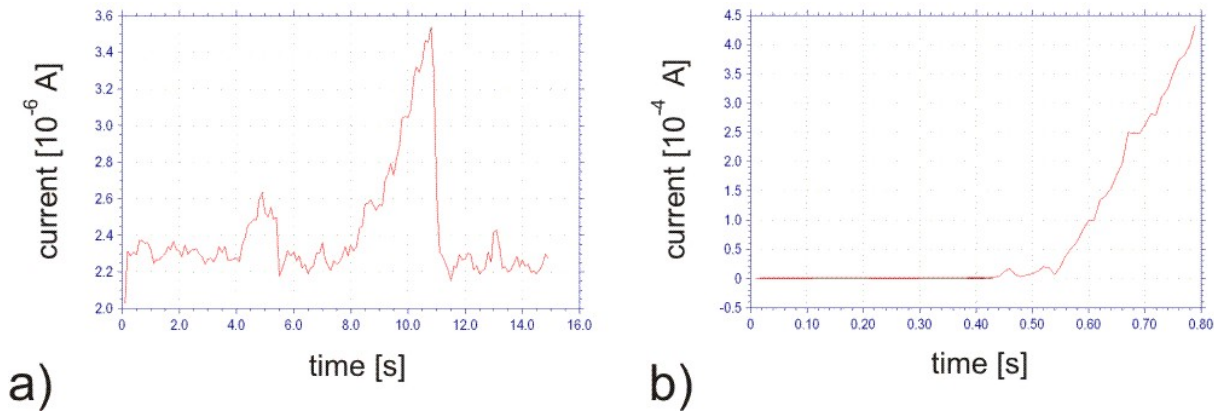


Figure 5.2: Current vs. time plots corresponding to electrochemical experiments on stainless steel AISI 316. The applied voltage to the electrochemical cell is: a) constant of 0.5 V, b) a linear sweep from 0.0 to 0.8 V.

5.1.2 Sample preparation

The alloy composition and microstructure can have a strong effect on its tendency to allow corrosion processes [125]. Aiming the pitting analysis as close to real life conditions as possible, a very common high quality grade of stainless steel is chosen: AISI 316 (see section 2.5.2). Samples are cut into a cylindrical disc of 4 mm height and 1 cm diameter. Also, two different polishing techniques were used: mechanical polishing, and electropolishing.

5.1.2.1 Mechanical polishing

The AISI 316 samples were always mechanically polished. First, using sandpaper, and then with different grades of polishing Al powder down to 0.05 microns. A serie of ultrasonic baths followed: in acetone, in isopropanol, in methanol, and in distilled water.

5.1.2.2 Electropolishing

An additional electrochemical polishing treatment was carried out in the preparation of some of the samples. Electropolishing uses a combination of rectified current and a blended chemical electrolyte bath to remove substrate material from the surface of a metal, diminishing scratches, burrs, or unwanted sharp edges. The steel sample is immersed in a temperature controlled bath of electrolyte and connected to the anode of a power supply, the negative terminal being attached to an auxiliary electrode. An ionic current flows from the anode (metal oxidizes) to the cathode (where reduction takes place). During this process, the protruding parts of the surface profile typically dissolve faster than the recesses, which is called *anodic leveling*. For the metal preparation a voltage of 50 volts was applied for 5 minutes. The choice of applied voltage and time was optimized after a comparison of optical microscope images (not shown) of different samples prepared under different conditions. The particular electrolyte used for this stage of the sample preparation is a solution of 133 ml glacial acetic acid and 25 g chromium trioxide in 7 ml of water.

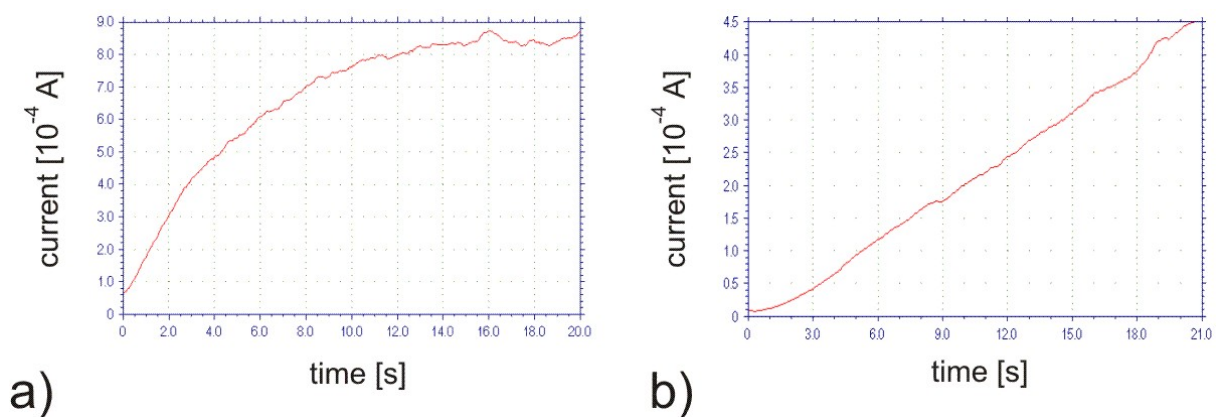


Figure 5.3: Current vs. time plots corresponding to electrochemical experiments with a constant potential applied of 0.7 V. a) mechanically and b) electrochemically polished stainless steel 316.

The resulting metal has fewer vulnerable spots and is significantly less prone to initiation of corrosion processes, as can be seen in Fig. 5.3. During the same electrochemical experiment, the current through the electropolished metal stays always below 50 % of the non electropolished one, indicating a smaller cover damage; especially significant is the difference during the initial stretch of the plot.

5.2 Results

5.2.1 AFM

Section 2.5.2.3 and 5.1 introduce the experimental techniques used to map the surface of SS 316 during its electrochemical corrosion. The present section shows six consecutive AFM scans where the nucleation and growth of a pit can be followed, and the corresponding profile plot, giving additional depth information (Fig. 5.4). The scans made after Fig. 5.4 f) (data not shown) indicate that the pit passivated and did not grow anymore. A small bump seems to precede the pit nucleations (as in Fig. 5.4 b)), maybe a fracture on the oxide cover. Another bump is often found at the bottom of the growing hole (Fig. 5.4 c), d), and e)), of which the nature is unclear: it could be a piece of the cover, it could belong to the pit walls, or it could be the result of uneven erosion dynamics within the hole due to convection patterns arising from hydrogen bubbles during the reaction [201]. 3D images corresponding to the first and last surface maps can be seen in Fig. 5.5.

This preliminary analysis showed that the profile of big flat pits can be better imaged with AFM, and that it is clearly an incompatible technique for the proper characterization of holes with horizontal grain attack or undercutting growth (Fig. 2.20). The respective SEM images may provide additional useful information from the pits contour-edge lines, the walls consistency, or bodies found at the bottom.

Although the temperature was controlled before and after each experiment to be sure that no significant changes may have altered the reaction environment, a constant temperature control while surface mapping is still a desired improvement for the setup.

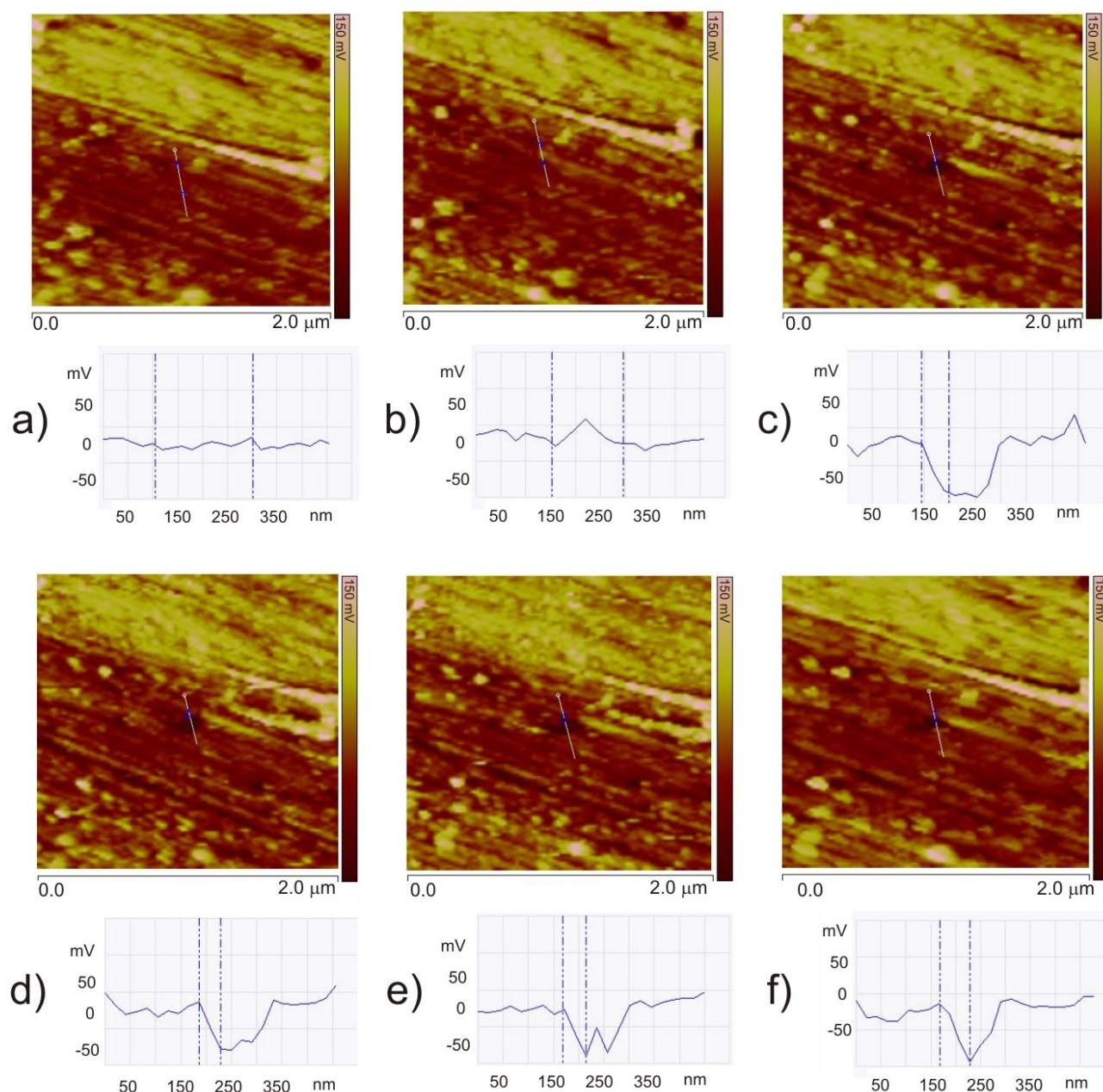


Figure 5.4: Subsequent AFM deflection images. After every scan, a voltage is applied for 3 seconds between the working electrode and the reference electrode: 0.1 V after a), 0.2 V after b), 0.3 V after c), 0.4 V after d), 0.5 V after e). Surface distance between reference bars indicate the pit depth evolution: c) $0.075 \mu\text{m}$, d) $0.076 \mu\text{m}$, e) $0.076 \mu\text{m}$, and f) $0.102 \mu\text{m}$.

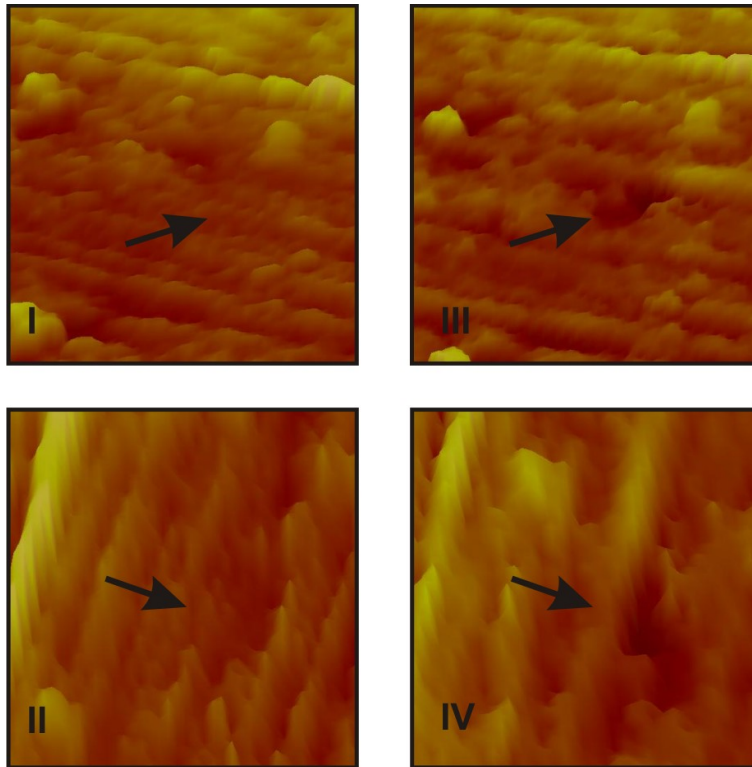


Figure 5.5: Three dimensional representation of the AFM scans above. I and II correspond to Fig. 5.4 a), III and IV show the hole seen in Fig. 5.4 f).

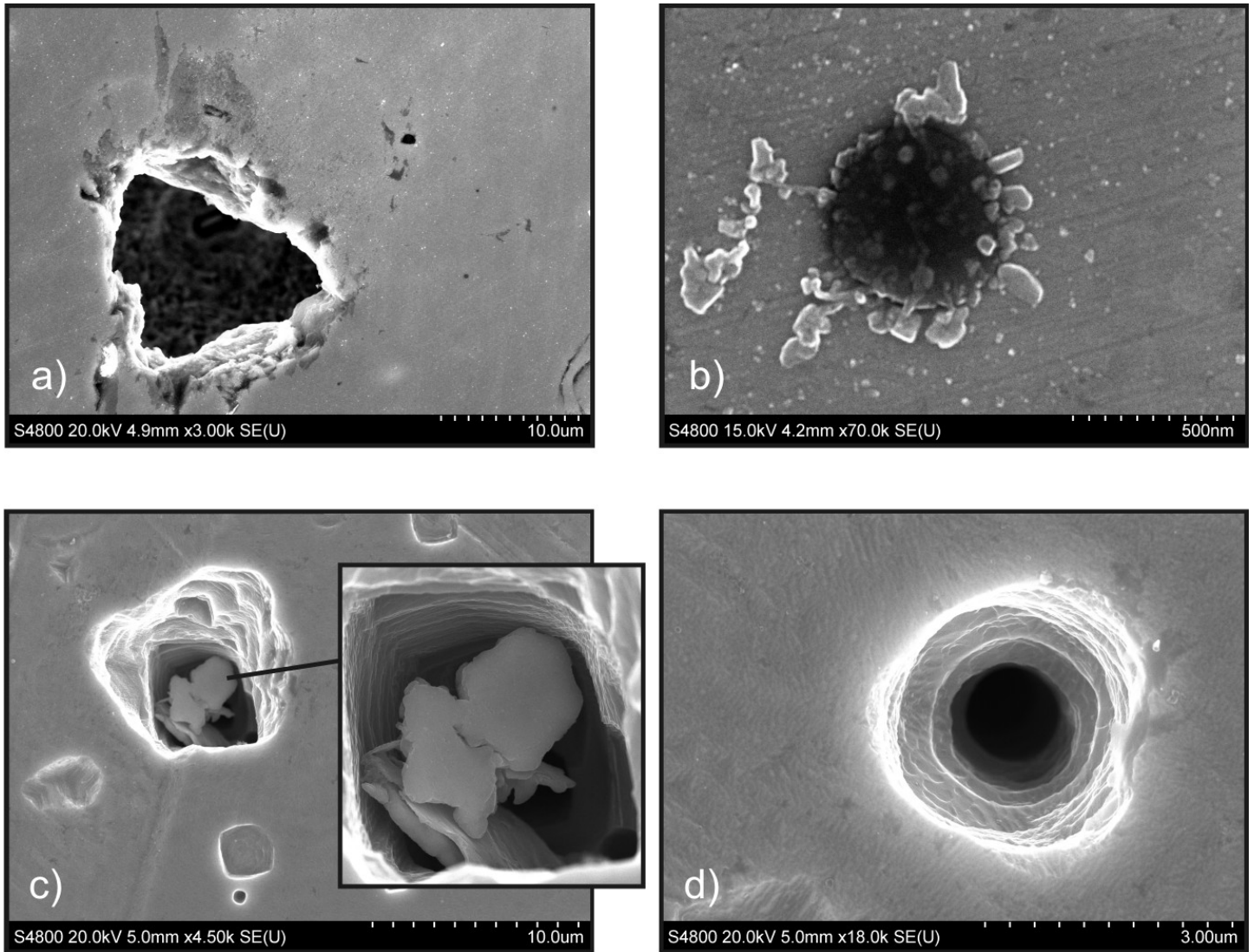


Figure 5.6: a) and b) SEM images of corrosion pits generated during the experiment shown in Fig. 5.4, using a mechanically polished sample. c) and d) corrosion pits generated during a similar experiment with an electro-polished sample.

5.2.2 SEM

After the *in situ* surface experiments presented in the previous sections, stainless steel samples were also analyzed with a SEM (see section 2.5.2.3) to further characterize the corrosion holes morphology, complementing the information obtained with AFM. Unfortunately, localizing and visualizing the very same pit with both techniques could not be achieved yet.

The images presented here (Fig. 5.6) give a general idea of the kinds of pit profiles that were generated, and show the difference between the results of the two sample polishing methods used. The (typically) abrupt walls of the mechanically polished sample of Fig. 5.6 a) contrast with the (typically) round edges of the electropolished metal (Fig. 5.6 c) and d)). The collapse of either the oxide covering layer or internal material that came off during the corrosion surrounds the pit in Fig. 5.6 b). Fig. 5.6 c) shows in detail a protruding body at the bottom of a hole, such as is also visible in the AFM profile of Fig. 5.4 d) and e).

5.3 Conclusions and future work

A morphological approach to the autocatalytic process of pitting corrosion for prevention, detection, and materials testing knowledge has been presented in a preliminary state. Three dimensional data has been obtained combining AFM and SEM, allowing resolve size, growing rate, and profile nature of single pits.

It is accepted that stable corrosion conditions normally lead to smooth surfaces having a characteristic hemispherical profile. On the other hand, pits grown under unstable conditions normally show rugged surfaces with pronounced crystallographic edges [197]. In other words, a morphological characterization of a corroded surface may give information about the prior reaction conditions.

After electropolishing, stainless steel is more effectively resistant against the onset and development of pitting corrosion. Not only is more aggressive electrolyte needed to nucleate pits (Fig. 5.3), but the morphology of the nucleated holes is less detrimental, less

likely to tunnel into the metal and to erode internal cavities where the ion concentration is always higher and the pits keep growing.

Implementing a pit identification technique, perhaps a lithographic marking of the surface, would help in tracking pits on the metal and allow both AFM and SEM to locate the same surface spot. With this improvement, the combined imaging techniques may lead to a test protocol to detect metal resistance towards pitting corrosion in its very first stage, most critical for preventive measures.

The corrosion pit sizes found in this work range from hundreds of nanometers to tens of micrometers. However, how big or how small they can be is not yet defined, although it might be relevant to determining unknown corrosion factors, specially if dimensions can be related to hole profiles. With more experience and larger probes, the AFM-SEM combination may cast new light on these issues.

Still preliminary in its results, a future goal of this morphological approach is to support and/or contrast mathematical models used to describe the pitting formation and growth process [194, 195, 196, 197, 198].

The present work is framed within a bigger project led by H. H. Rotermund, in which the already developed EMSI plus optical microscopy setup [14], is combined with in-line holography [202] to advance in the knowledge and prevention of corrosion. The morphological analysis of pitting corrosion gains relevance in the context of the mentioned techniques and is expected to generate a great deal of further practical information about metal corrosion.

Chapter 6

Summary

The number of spatiotemporal structures that chemical systems far from equilibrium can exhibit is remarkable. This thesis is aimed at exploring surface reactions under well defined conditions and attempts to control and manipulate the corresponding reaction-diffusion dynamics. Its approach is dominated by the use of visual techniques and image processing. The summary is divided into two sections, one for each of the systems studied.

6.1 CO oxidation on Pt(110)

The heterogeneous catalysis of CO oxidation on platinum was controlled by modulating the partial pressure of the CO involved in this self-oscillating reaction. Two different approaches were followed: resonant periodic forcing and introduction of artificial noise. Furthermore, the particular dynamics of the reactions taking place on an ultra-thin Pt foil were studied.

The first approach was intended to drive the system to resonant forcing regimes, periodically regulating the CO dosed into the chamber with a frequency chosen to be an integer number times the intrinsic natural frequency of the system. The experimental parameters were set in such a way that the reaction exhibits chemical turbulence in the absence of forcing. The experiments performed in the 2:1 and 3:1 forcing cases showed the formation of clusters in agreement with previous theoretical results, and were further discussed. The concept of Bloch walls were introduced, and their shape and

time evolution were characterized. The implementation of a gas compressor allowed, for the first time, to reach the 3:1 regime, and even the 4:1. Not seen before, the complex spatiotemporal structures arising from 4:1 forcing also present phase locked domains, but with significantly different sizes than previously seen in the CO-Pt system. In all cases, turbulence could be suppressed effectively with resonant forcing, yielding phase-locked structures. Previous work was done on periodic forcing of the same system, but it was not focused on resonant effects; the forcing amplitude then needed to suppress turbulences was two orders of magnitude higher than in the present experiments, underlying the sensitivity of the system in the resonant regime. In addition, the effect of periodic forcing on a propagating pulse is presented, where two different reactions to the stimulus can be observed simultaneously.

The analysis of the experimental results is based on the processing of PEEM images taken from the Pt single crystal, space-time plots, and Fourier spectrograms as well as a phase and amplitude representation of the results.

Even though the presented setup has successfully reached the 2:1, 3:1, and 4:1 resonant regimes, a better understanding of these complex scenarios could be achieved with an improved periodic gas compressor: smooth and progressive adjustments of the forcing speed and amplitude are desirable features, needed for instance for clusters front explosions (as predicted by models), or to complete the plot of experimental Arnold tongues.

The second approach showed the effect of global noise applied to one of the reaction parameters via a random modulation of the amount of CO in the reaction chamber. As above, PEEM was the imaging technique used. The dynamics temporal behavior was analyzed with the help of space-time plots.

The effect of noise on the bistable CO-to-oxygen transitions was studied: a shrinking of the corresponding hysteresis loop and a decrease in the reactivity needed to achieve the transitions was found. Also defect induced patterns arising in an otherwise homogeneously CO-covered surface was reported. The goal of some of the experiments was again to suppress developed chemical turbulence. The forcing amplitude needed to reach total entrainment with the noise signal is comparable to the value that periodic forcing needs in the resonant regime. Remarkably, for certain noise parameters, regular structures were sustained. While artificial noise was introduced, the system presented a CO₂ production

increase. This means that noise can raise the reactivity, which in other systems might be relevant as a production enhancer. Experiments were contrasted with KEE model results, with particularly good agreement for the bistable transitions and the space-time plots generated during the experiments of turbulence control.

An ultra-thin platinum (110) foil was used as a catalytic surface to characterize the reaction heat as well as the species' adsorption heat. Due to the low heat capacity of the sample, small amounts of heat can increase the temperature and induce a detectable surface expansion. A direct calorimetric approach to the reaction kinetics was supported by the topographic reconstruction of the Pt foil profile. An adapted Michelson interferometer was used for this reconstruction. The setup and its calibration were introduced, and then CO and oxygen adsorption energies, as well as titration experiments (CO to oxygen and vice versa), were characterized.

The surface reflectivity change induced by the adsorbates was confirmed by the comparison of the surface profiles for a clean surface, a CO covered surface, and an oxygen covered one. Pattern formation due to thermal coupling could also be seen. This innovative topographic/calorimetric approach was compared in terms of detection limit and operating environment conditions with different direct calorimetric techniques. Further improvements concerning a more versatile topographic reconstruction algorithm were proposed, that would be able to handle large and small deformations alike. An alternative setup that combines the sample with a piezo to relieve surface pre-strain was also introduced, which would permit removing one of the laser beams.

6.2 Pitting corrosion on stainless steel

Pitting corrosion is a degradation process affecting metals that have a stable passivating layer. Originating at weak spots of that layer, pits go through a state of metastability that may end in stable pitting. The activity alternations (active-passive) of these generated pits, together with the concentration of a given species within them determine their shape. Through the release of aggressive ions pits influence their surroundings, where new events are more likely to happen, turning the spreading of corrosion into a reaction-diffusion phenomenon. The profile of each pit and its growing dynamics is a consequence

of the surface composition, the concentration of aggressive species in contact with it, and also its own shape.

The autocatalytic growth and propagation of corrosion pits on stainless steel were studied from a morphological point of view. AFM and SEM microscopy techniques were combined to characterize the depth and profile of pits generated in a three electrode electrochemical cell. *In situ* experiments were performed in a NaCl electrolytic solution. Images and profiles of the growing process of pits, from nucleation to passivation were discussed. Two different sample preparations were used to provide comparative information of the metal resistance against corrosion. Future work will be focused on contrasting the morphology of pits in a wide range of reaction parameters and different sample preparations. An expected improvement will be the use of a pit recognition system to allow imaging the same pit with both atomic force and scanning electron microscopes.

Bibliography

- [1] J. D. Murray. How the leopard gets its spots. *Scientific American* **258** (1988) 80.
- [2] J. D. Murray. *Mathematical Biology*. Berlin (1989).
- [3] A. M. Turing. The chemical basis of morphogenesis. *Philosophical Transactions of the Royal Society of London Series B-Biological Sciences* **237** (1952) 37.
- [4] J. Tyson. *The Belousov-Zhabotinsky reaction*. Springer-Verlag, Heidelberg (1976).
- [5] I. Prigogine and R. Lefever. Symmetry breaking instabilities in dissipative systems. *Journal of Chemical Physics* **48** (1968) 1695.
- [6] I. Prigogine and R. Stengers. *Order out of Chaos*. Heinemann, London (1983).
- [7] J. Poincare. *Les Methodes Nouvelles de la Mecanique Celeste*. Gauthier-Villars, Paris (1892-1899).
- [8] Y. Kuznetsov. *Elements of applied bifurcation theory*. Springer, New York (1995).
- [9] <http://nobelprize.org>.
- [10] M. Eiswirth and G. Ertl. Kinetic oscillations in the catalytic CO oxidation on a Pt(110) surface. *Surf. Sci.* **177** (1986) 90.
- [11] G. Ertl. Oscillatory kinetics and spatiotemporal self-organization in reactions at solid-surfaces. *Science* **254** (1991) 1750.
- [12] W. Engel. Ph.D. thesis, Freie Universitaet Berlin (1968).
- [13] H. H. Rotermund. Imaging of dynamic processes on surfaces by light. *Surf. Sci. Rep.* **29** (1997) 267.

- [14] C. Punckt, M. Boelscher, H. H. Rotermund, A. S. Mikhailov, L. Organ, N. Budiansky, J. R. Scully, and J. L. Hudson. Sudden onset of pitting corrosion on stainless steel as a critical phenomenon. *Science* **305** (2004) 1133.
- [15] M. Dornhege, C. Punckt, J. L. Hudson, and H. H. Rotermund. Spreading of corrosion on stainless steel simultaneous observation of metastable pits and oxide film. *Journal of the Electrochemical Society* **154** (2007) C24.
- [16] <http://www.popmath.org.uk>.
- [17] R. Hoyle. *Pattern formation, an introduction to methods*. Cambridge University Press, Cambridge (2006).
- [18] W. Ashby. Principles of the self-organizing dynamic system. *Journal of General Psychology* **37** (1947) 125.
- [19] H. Haken. *Series in Synergetics*. Springer, Berlin (1977-2006).
- [20] M. Dornhege, C. Punckt, and H. H. Rotermund. *Analysis and Control of Complex Nonlinear Processes*. World Scientific Lecture Notes in Complex Systems (2007).
- [21] L. Organ, J. R. Scully, A. Mikhailov, and J. L. Hudson. A spatiotemporal model of interactions among metastable pits and the transition to pitting corrosion. *Electrochim. Acta* (2005) .
- [22] P. Glendinning. *Stability, instability and chaos: an introduction to the theory of nonlinear differential equations*. Cambridge University Press, Cambridge (1994).
- [23] G. a. Holmes. *Nonlinear Oscillations, Dynamical Systems and Bifurcations of Vector Fields*. New York (1983).
- [24] A. S. Mikhailov. *Foundations of Synergetics I. Distributed Active Systems*. Springer-Verlag, Berlin – Heidelberg – New York, 2 edn. (1994).
- [25] J. Walleczek. *Self-organized biological dynamics and nonlinear control*. Cambridge University Press, Cambridge (2000).
- [26] G. Li, Q. Ouyang, V. Petrov, and H. Swinney. Transition from simple rotating chemical spirals to meandering and travelling spirals. *Phys. Rev. Lett.* **77** (1996) 10.
- [27] W. C. Sandstede B, Scheel A. Bifurcations and dynamics of spiral waves. *Journal of Nonlinear Science* **9** (1999) 439.

- [28] M. Baer and M. Eiswirth. Turbulence due to spiral breakup in a continuous excitable medium. *Phys. Rev. E* **48** (1993) R1635.
- [29] S. Alonso, F. Sagues, and A. S. Mikhailov. Taming Winfree turbulence of scroll waves in excitable media. *Science* **299** (2003) 1722.
- [30] Y. Kuramoto. *Chemical oscillations, waves and turbulence*. Springer-Verlag, Berlin – Heidelberg – New York (1984).
- [31] A. T. Winfree. Biological rhythms and behavior of populations of coupled oscillators. *Journal of Theoretical Biology* **16** (1967) 15.
- [32] C. Beta, A. S. Mikhailov, H. H. Rotermund, and G. Ertl. Defect-mediated turbulence in a catalytic surface reaction. *Europhysics Letters* **75** (2006) 868.
- [33] S. Jakubith, H. H. Rotermund, W. Engel, A. von Oertzen, and G. Ertl. Spatiotemporal concentration patterns in a surface-reaction: Propagating and standing waves, rotating spirals, and turbulence. *Phys. Rev. Lett.* **65** (1990) 3013.
- [34] H. H. Rotermund, W. Engel, M. Kordesch, and G. Ertl. Imaging of spatiotemporal pattern evolution during carbon-monoxide oxidation on platinum. *Nature* **343** (1990) 355.
- [35] T. E. Jackman, J. A. Davies, D. P. Jackson, W. N. Unertl, and P. R. Norton. The Pt(110) phase-transitions: A study by rutherford backscattering, nuclear microanalysis, LEED and thermal-desorption spectroscopy. *Surf. Sci.* **120** (1982) 389.
- [36] H. Niehus. Analysis of the Pt(110)-(1 × 2) surface reconstruction. *Surf. Sci.* **145** (1984) 407.
- [37] G. L. Kellogg. Direct observations of the (1 × 2) surface reconstruction on the Pt(110) plane. *Phys. Rev. Lett.* **55** (1985) 2168.
- [38] P. Fery, W. Moritz, and D. Wolf. Structure determination of the (1 × 2) and (1 × 3) reconstructions of Pt(110) by low energy electron diffraction. *Phys. Rev. B* **38** (1988) 7275.
- [39] P. Fenter and T. Gustafsson. Structural analysis of the Pt-(1 × 2) surface using medium-energy ion scattering. *Phys. Rev. B* **38** (1988) 10197.
- [40] T. Gritsch, D. Coulman, R. J. Behm, and G. Ertl. Mechanism of the CO-induced (1×2)-(1×1) structural transformation of Pt(110). *Phys. Rev. Lett.* **63** (1989) 1086.

- [41] R. Imbihl, S. Ladas, and G. Ertl. Spatial coupling of autonomous kinetic oscillations in the catalytic CO oxidation on Pt(110). *Surf. Sci.* **215** (1989) L307.
- [42] C. Punckt. *Untersuchungen zur optischen Beobachtung musterbildender katalytischer Oberflaechenreaktionen*. Ph.D. thesis, Technische Universitaet Berlin (2005).
- [43] M. Pollmann. *Musterbildung bei der CO-Oxidation auf Pt(110) unter gezielter Beeinflussung*. Ph.D. thesis, Freie Universitaet Berlin (2002).
- [44] G. Blyholder. Molecular orbital view of chemisorbed carbon monoxide. *J. Phys. Chem.* **68** (1964) 2772.
- [45] G. Doyen and G. Ertl. Theory of carbon-monoxide chemisorption on transition-metals. *Surface Science* **43** (1974) 197.
- [46] C. M. Comrie and R. M. Lambert. Chemisorption and surface structural chemistry of carbon monoxide on Pt-(1 \times 2). *J. Chem. Soc., Faraday Trans. I* **72** (1976) 1659.
- [47] R. W. McCabe and L. D. Schmidt. Adsorption of H₂ and CO on clean and oxidized Pt(110). *Surf. Sci.* **60** (1976) 85.
- [48] R. P. H. Gasser and E. B. Smith. A surface mobility parameter for chemisorption. *Chem. Phys. Lett.* **1** (1967) 457.
- [49] P. R. Norton, J. A. Davies, and T. E. Jackman. Absolute coverages of CO and O on Pt(110); comparison of saturation CO coverages on Pt(100), (110), and (111) surfaces. *Surf. Sci.* **122** (1982) L593.
- [50] W. N. Unertl, T. E. Jackman, P. R. Norton, D. P. Jackson, and J. A. Davies. Surface phases of clean, CO and NO covered Pt(110). *J. Chem. Phys.* **20** (1982) 607.
- [51] R. Imbihl, S. Ladas, and G. Ertl. The CO-induced (1 \times 2) reversible (1 \times 1) phase-transition of Pt(110) studied by LEED and workfunction measurements. *Surf. Sci.* **206** (1988) L903.
- [52] H. Over and S. Y. Tong. Chemically adsorbed layers on metal and semiconductor surfaces. In W. N. Unertl, editor, *Physical structure*, vol. 1 of *Handbook of surface science*. Elsevier, Amsterdam (1996).
- [53] A. von Oertzen, H. H. Rotermund, and S. Nettesheim. Diffusion of carbon monoxide and oxygen on Pt(110): experiments performed with the PEEM. *Surf. Sci.* **311** (1994) 322.

- [54] J. Fair and R. J. Madix. Low and high coverage determinations of the rate of carbon monoxide adsorption and desorption from Pt(110). *J. Chem. Phys.* **73** (1980) 3480.
- [55] P. Hofmann, S. R. Bare, and D. A. King. Surface phase-transitions in CO chemisorption on Pt(110). *Surface Science* **117** (1982) 245.
- [56] A. V. Walker, B. Kloetzer, and D. A. King. Dynamics and kinetics of oxygen dissociative adsorption on Pt(110)(1×2). *J. Chem. Phys.* **109** (1998) 6879.
- [57] M. Wilf and P. T. Dawson. Adsorption and desorption of oxygen on the Pt(110) surface - a thermal desorption and LEED-AES Study. *Surf. Sci.* **65** (1977) 399.
- [58] I. Langmuir. The mechanism of the catalytic action of platinum in the reactions $2\text{CO} + \text{O}_2 = 2 \text{CO}(2)$ and $2\text{H}(2) + \text{O}_2 = 2\text{H}(2)\text{O}$. *Transactions of the Faraday Society* **17** (1922) 0621.
- [59] R. Imbihl and G. Ertl. Oscillatory kinetics in heterogeneous catalysis. *Chem. Rev.* **95** (1995) 697.
- [60] K. Krischer, M. Eiswirth, and G. Ertl. Bifurcation-analysis of an oscillating surface-reaction model. *Surf. Sci.* **251** (1991) 900.
- [61] N. Freyer, M. Kiskinova, G. Pirug, and H. P. Bonzel. Oxygen-adsorption on Pt(110)-(1×2) and Pt(110)-(1×1). *Surf. Sci.* **166** (1986) 206.
- [62] M. Eiswirth, P. Moeller, K. Wetzl, R. Imbihl, and G. Ertl. Mechanisms of spatial self-organization in isothermal kinetic oscillations during the catalytic CO oxidation on Pt single-crystal surfaces. *J. Chem. Phys.* **90** (1989) 510.
- [63] A. von Oertzen, A. S. Mikhailov, H. H. Rotermund, and G. Ertl. Subsurface oxygen in the CO oxidation reaction on Pt(110): experiments and modeling of pattern formation. *J. Phys. Chem. B* **102** (1998) 4966.
- [64] K. C. Rose, R. Imbihl, B. Rausenberger, C. S. Rastomjee, W. Engel, and A. M. Bradshaw. Nucleation of chemical waves at structural defects: a mirror electron microscopy study of catalytic CO oxidation on Pt(110). *Surface Science* **352** (1996) 258.
- [65] M. Bertram. *Controlling Turbulence and Pattern Formation in Chemical Reactions*. Ph.D. thesis, Technische Universitaet Berlin (2002).

- [66] H. H. Rotermund, G. Haas, R. U. Franz, R. M. Tromp, and G. Ertl. Imaging pattern-formation in surface-reactions from ultrahigh-vacuum up to atmospheric pressures. *Science* **270** (1995) 608.
- [67] B. Marwaha, J. Annamalai, and D. Luss. Hot zone formation during carbon monoxide oxidation in a radial flow reactor. *Chemical Engineering Science* **56** (2001) 89.
- [68] F. Cirak, J. E. Cisternas, A. M. Cuitino, G. Ertl, P. Holmes, I. G. Kevrekidis, M. Ortiz, H. H. Rotermund, M. Schunack, and J. Wolff. Oscillatory thermomechanical instability of an ultrathin catalyst. *Science* **300** (2003) 1932.
- [69] C. Punckt, P. S. Bodega, and H. H. Rotermund. Quantitative measurement of the deformation of ultra-thin platinum foils during adsorption and reaction of CO and O₂. *Surface Science* **600** (2006) 3101.
- [70] R. Imbihl, A. E. Reynolds, and D. Kaletta. Model for the formation of a microscopic Turing structure - the faceting of Pt(110) during catalytic-oxidation of CO. *Physical Review Letters* **67** (1991) 275.
- [71] J. Falta, R. Imbihl, and M. Henzler. Spatial Pattern-Formation in a Catalytic Surface-Reaction - the Faceting of Pt(110) in CO and O₂. *Physical Review Letters* **64** (1990) 1409.
- [72] M. Sander, R. Imbihl, and G. Ertl. Conditions and Kinetics of the Faceting of Pt(110) and Pt(210) in CO+O₂. *Surface Science* **251** (1991) 921.
- [73] S. Ladas, R. Imbihl, and G. Ertl. Microfacetting of a Pt(110) surface during catalytic CO oxidation. *Surf. Sci.* **197** (1988) 153.
- [74] R. Imbihl, M. Sander, and G. Ertl. The formation of new oxygen-adsorption states on Pt(110) by facetting induced by catalytic reaction. *Surface Science* **204** (1988) L701.
- [75] J. Lauterbach, G. Haas, H. H. Rotermund, and G. Ertl. Spatiotemporal pattern-formation on polycrystalline platinum surfaces during catalytic CO oxidation. *Surf. Sci.* **294** (1993) 116.
- [76] C. E. Wartnaby, A. Stuck, Y. Y. Yee, and D. A. King. Microcalorimetric heats of adsorption for CO, NO, and oxygen on Pt(110). *J. Phys. Chem.* **100** (1996) 12483.
- [77] A. F. Holleman and E. Wiberg. *Lehrbuch der Anorganischen Chemie*. de Gruyter, Berlin/New York, 101 edn. (1995).

- [78] C. E. Wartnaby, A. Stuck, Y. Y. Yeo, and D. A. King. Calorimetric measurement of catalytic surface reaction heat: CO oxidation on Pt(110). *J. Chem. Phys.* **102** (1995) 1855.
- [79] A. Stuck, C. E. Wartnaby, Y. Y. Yeo, J. T. Stuckless, N. al Sarraf, and D. A. King. An improved single crystal adsorption calorimeter. *Surf. Sci.* **349** (1996) 229.
- [80] K. Krischer, M. Eiswirth, and G. Ertl. Oscillatory CO oxidation on Pt(110) - Modeling of temporal self-organization. *J. Chem. Phys.* **96** (1992) 9161.
- [81] M. Baer, M. Eiswirth, H. H. Rotermund, and G. Ertl. Solitary-wave phenomena in an excitable surface-reaction. *Phys. Rev. Lett.* **69** (1992) 945.
- [82] C. Beta, M. Bertram, A. S. Mikhailov, H. H. Rotermund, and G. Ertl. Controlling turbulence in a surface chemical reaction by time-delay autosynchronization. *Phys. Rev. E* **67** (2003) 6224.
- [83] M. Kim, M. Bertram, M. Pollmann, A. von Oertzen, A. S. Mikhailov, H. H. Rotermund, and G. Ertl. Controlling chemical turbulence by global delayed feedback: pattern formation in catalytic CO oxidation on Pt(110). *Science* **292** (2001) 1357.
- [84] M. Baer, S. Nettesheim, H. H. Rotermund, M. Eiswirth, and G. Ertl. Transition between fronts and spiral-waves in a bistable surface-reaction. *Phys. Rev. Lett.* **74** (1995) 1246.
- [85] G. Haas, M. Baer, I. G. Kevrekidis, P. B. Rasmussen, H. H. Rotermund, and G. Ertl. Observation of front bifurcations in controlled geometries - from one to two dimensions. *Phys. Rev. Lett.* **75** (1995) 3560.
- [86] M. Bertram and A. S. Mikhailov. Pattern formation on the edge of chaos: mathematical modeling of CO oxidation on a Pt(110) surface under global delayed feedback. *Phys. Rev. E* **67** (2003) 036207.
- [87] A. von Oertzen, A. Mikhailov, H. H. Rotermund, and G. Ertl. Subsurface oxygen formation on the Pt(110) surface: experiment and mathematical modeling. *Surf. Sci.* **350** (1996) 259.
- [88] K. Krischer. *Nichtlineare Dynamik zweier Grenzflaechenreaktionen*. Ph.D. thesis, Freie Universitaet Berlin (1990).
- [89] M. Eiswirth. *Phaenomene der Selbstorganisation bei der Oxidation von CO an Pt(110)*. Ph.D. thesis, Ludwig-Maximilians-Universitaet Muenchen (1987).

- [90] M. Baer, C. Zuelicke, M. Eiswirth, and G. Ertl. Theoretical modeling of spatiotemporal self-organization in a surface catalyzed reaction exhibiting bistable kinetics. *J. Chem. Phys.* **96** (1992) 8595.
- [91] M. Falcke, M. Baer, H. Engel, and M. Eiswirth. Traveling waves in the CO oxidation on Pt(110) - Theory. *J. Chem. Phys.* **97** (1992) 4555.
- [92] M. Baer, N. Gottschalk, M. Eiswirth, and G. Ertl. Spiral waves in a surface-reaction: model calculations. *J. Chem. Phys.* **100** (1994) 1202.
- [93] M. Hildebrand, M. Baer, and M. Eiswirth. Statistics of topological defects and spatiotemporal chaos in a reaction-diffusion system. *Phys. Rev. Lett.* **75** (1995) 1503.
- [94] M. Falcke and H. Engel. Influence of global coupling through the gas-phase on the dynamics of CO oxidation on Pt(110). *Phys. Rev. E* **50** (1994) 1353.
- [95] M. Falcke and H. Engel. Pattern formation during the CO oxidation on Pt(110) surfaces under global coupling. *J. Chem. Phys.* **101** (1994) 6255.
- [96] M. Falcke, H. Engel, and M. Neufeld. Cluster formation, standing waves, and stripe patterns in oscillatory active media with local and global coupling. *Phys. Rev. E* **52** (1995) 763.
- [97] A. von Oertzen, H. H. Rotermund, A. S. Mikhailov, and G. Ertl. Standing wave patterns in the CO oxidation reaction on a Pt(110) surface: experiments and modeling. *J. Phys. Chem. B* **104** (2000) 3155.
- [98] H. Levine and X. Q. Zou. Standing waves in catalysis at single-crystal surfaces. *Physical Review Letters* **69** (1992) 204.
- [99] H. Levine and X. Q. Zou. Catalysis at single-crystal Pt(110) surfaces - global coupling and standing waves. *Physical Review E* **48** (1993) 50.
- [100] M. Falcke and H. Engel. Traveling pulses in anisotropic oscillatory media with global coupling. *Physical Review E* **56** (1997) 635.
- [101] S. Nettesheim, A. von Oertzen, H. H. Rotermund, and G. Ertl. Reaction-diffusion patterns in the catalytic CO oxidation on Pt(110) - front propagation and spiral waves. *J. Chem. Phys.* **98** (1993) 9977.
- [102] S. Jakubith. Ph.D. thesis, Freie Universitaet Berlin (1991).

- [103] H. Beusch, E. Wicke, and P. Fieguth. Thermisch und kinetisch verursachte Instabilitäten im Reaktionsverhalten einzelner Katalysatorkörner. *Chem.-Ing.-Tech.* **44** (1972) 445.
- [104] G. Ertl, P. R. Norton, and J. Rustig. Kinetic oscillations in the platinum-catalyzed oxidation of CO. *Physical Review Letters* **49** (1982) 177.
- [105] M. Eiswirth, K. Krischer, and G. Ertl. Transition to chaos in an oscillating surface-reaction. *Surf. Sci.* **202** (1988) 565.
- [106] M. Eiswirth and G. Ertl. Forced-oscillations of a self-oscillating surface-reaction. *Physical Review Letters* **60** (1988) 1526.
- [107] M. Eiswirth, P. Moeller, and G. Ertl. Periodic perturbations of the oscillatory CO oxidation on Pt(110). *Surf. Sci.* **208** (1989) 13.
- [108] W. Engel, M. E. Kordesch, H. H. Rotermund, S. Kubala, and A. von Oertzen. A UHV-compatible photoelectron emission microscope for applications in surface science. *Ultramicroscopy* **36** (1991) 148.
- [109] H. H. Rotermund. Imaging pattern formation in surface reactions from ultra-high vacuum up to atmospheric pressures. *Surf. Sci.* **386** (1997) 10.
- [110] R. Luther. Space propagation of chemical reactions. *Zeitschrift Fur Elektrochemie Und Angewandte Physikalische Chemie* **12** (1906) 596.
- [111] H. H. Rotermund, S. Jakubith, A. von Oertzen, and G. Ertl. Solitons in a surface-reaction. *Phys. Rev. Lett.* **66** (1991) 3083.
- [112] K. C. Rose, D. Battogtokh, A. Mikhailov, R. Imbihl, W. Engel, and A. M. Bradshaw. Cellular structures in catalytic reactions with global coupling. *Physical Review Letters* **76** (1996) 3582.
- [113] P. S. Bodega, P. Kaira, C. Beta, D. Krefting, D. Bauer, B. Mirwald-Schulz, C. Punckt, and H. H. Rotermund. High frequency periodic forcing of the oscillatory catalytic CO oxidation on Pt (110). *New Journal of Physics* **9** (2007) 61.
- [114] M. D. Graham, I. G. Kevrekidis, K. Asakura, J. Lauterbach, K. Krischer, H. H. Rotermund, and G. Ertl. Effects of boundaries on pattern-formation - catalytic oxidation of CO on platinum. *Science* **264** (1994) 80.
- [115] L. Qiao, I. G. Kevrekidis, C. Punckt, and H. H. Rotermund. Geometry-induced pulse instability in microdesigned catalysts: the effect of boundary curvature. *Phys. Rev. E* **73** (2006) 036219.

- [116] L. Qiao, I. G. Kevrekidis, C. Punckt, and H. H. Rotermund. Guiding chemical pulses through geometry: Y junctions. *Physical Review E* **73** (2006) 6219.
- [117] M. Stich, C. Punckt, C. Beta, and H. H. Rotermund. Control of spatiotemporal chaos in catalytic CO oxidation by laser-induced pacemakers. *Philosophical Transactions of the Royal Society A-Mathematical Physical and Engineering Sciences* **366** (2008) 419.
- [118] R. Imbihl. Nonlinear dynamics on catalytic surfaces. *Catal. Today* **105** (2005) 206.
- [119] H. H. Rotermund, W. Engel, S. Jakubith, A. von Oertzen, and G. Ertl. Methods and application of UV photoelectron microscopy in heterogeneous catalysis. *Ultramicroscopy* **36** (1991) 164.
- [120] A. Oertzen. *Untersuchung der Diffusion von Adsorbaten mittels Photoemissions-Elektronenmikroskopie (PEEM)*. Ph.D. thesis, Freie Universitaet Berlin (1992).
- [121] E. Hecht. *Optics*. Addison Wesley Longman, Inc., New York (1998).
- [122] A. A. Michelson and E. W. Morley. On the relative motion of the earth and the luminiferous aether. *Philos. Mag. S. 5* **24** (1887) 449.
- [123] F. Mansfeld. *Corrosion Mechanisms*. Marcel Dekker, New York (1987).
- [124] L. Balazs and J. F. Gouyet. 2-Dimensional pitting corrosion of aluminum thin-layers. *Physica A* **217** (1995) 319.
- [125] Z. Szklarska-Smialowska. *Pitting corrosion of metals*. National Assoc. of Corrosion Engineers, Houston, Texas (1986).
- [126] T. T. Lunt, J. R. Scully, V. Brusamarello, A. S. Mikhailov, and J. L. Hudson. Spatial interactions among localized corrosion sites, experiments and modeling. *J. Electrochem. Soc.* **149** (2002) B163.
- [127] G. S. Frankel. Pitting corrosion of metals - A review of the critical factors. *J. Electrochem. Soc.* **145** (1998) 2186.
- [128] P. C. Pistorius and G. T. Burstein. Metastable pitting corrosion of stainless steel and the transition to stability. *Philos. T. Roy. Soc. A* **341** (1992) 531.
- [129] M. Dornhege. *Beobachtung von Prozessen an der Phasengrenze Elektrode/Elektrolyt und deren Einordnung in den Bereich der nichtlinearen Dynamik*. Ph.D. thesis, Technische Universitaet Berlin (2007).

- [130] Z. Szklarsk. Review of literature on pitting corrosion published since 1960. *Corrosion* **27** (1971) 223.
- [131] www.corrosiondoctors.org.
- [132] C. M. Abreu, M. J. Cristobal, R. Losada, X. R. Novoa, G. Pena, and M. C. Perez. High frequency impedance spectroscopy study of passive films formed on AISI 316 stainless steel in alkaline medium. *J. Electroanal. Chem.* **572** (2004) 335.
- [133] M. Knoll. Charge potential and secondary emissions of electron irradiated bodies. *Physikalische Zeitschrift* **36** (1935) 861.
- [134] C. W. Oatley. The early history of the scanning electron-microscope. *Journal of Applied Physics* **53** (1982) R1.
- [135] H. Lueth. *Surfaces and Interfaces of Solid Materials*. Springer, Berlin (1996).
- [136] G. Binnig, C. F. Quate, and C. Gerber. Atomic Force Microscope. *Physical Review Letters* **56** (1986) 930.
- [137] G. Binnig and H. Rohrer. Scanning Tunneling Microscopy. *Helvetica Physica Acta* **55** (1982) 726.
- [138] J. Buck and E. Buck. Synchronous fireflies. *Scientific American* **234** (1976) 74.
- [139] M. R. Guevara and L. Glass. Phase locking, period doubling bifurcations and chaos in a mathematical-model of a periodically driven oscillator - a theory for the entrainment of biological oscillators and the generation of cardiac dysrhythmias. *Journal of Mathematical Biology* **14** (1982) 1.
- [140] T. Bohr, P. Bak, and M. H. Jensen. Transition to chaos by interaction of resonances in dissipative systems. Josephson-junctions, charge-density waves, and standard maps. *Physical Review A* **30** (1984) 1970.
- [141] F. W. Schneider. Periodic Perturbations of Chemical Oscillators - Experiments. *Annual Review of Physical Chemistry* **36** (1985) 347.
- [142] P. Rehms and J. Ross. *Oscillations and Travelling Wave in Chemical Systems*. Wiley, New York (1985).
- [143] A. L. Lin, M. Bertram, K. Martinez, H. L. Swinney, A. Ardelea, and G. F. Carey. Resonant phase patterns in a reaction-diffusion system. *Physical Review Letters* **84** (2000) 4240.

- [144] A. Pikovsky, M. Rosenblum, and J. Kurths. *Synchronization: A universal concept in nonlinear science*. Cambridge nonlinear science series: 12. Cambridge University Press (2001).
- [145] V. Petrov, Q. Ouyang, and H. L. Swinney. Resonant pattern formation in a chemical system. *Nature* **388** (1997) 655.
- [146] P. B. Umbanhowar, F. Melo, and H. L. Swinney. Localized excitations in a vertically vibrated granular layer. *Nature* **382** (1996) 793.
- [147] R. Kapral and K. Showalter. *Chemical Waves and Patterns*. Kluwer, Dordrecht (1995).
- [148] A. L. Lin, A. Hagberg, A. Ardelea, M. Bertram, H. L. Swinney, and E. Meron. Four-phase patterns in forced oscillatory systems. *Physical Review E* **62** (2000) 3790.
- [149] A. L. Lin, A. Hagberg, E. Meron, and H. L. Swinney. Resonance tongues and patterns in periodically forced reaction-diffusion systems. *Physical Review E* **69** (2004) 6.
- [150] V. K. Vanag, A. M. Zhabotinsky, and I. R. Epstein. Oscillatory clusters in the periodically illuminated, spatially extended Belousov-Zhabotinsky reaction. *Physical Review Letters* **86** (2001) 552.
- [151] B. Marts, K. Martinez, and A. L. Lin. Front dynamics in an oscillatory bistable belousov-zhabotinsky chemical reaction. *Phys. Rev. E* **70** (2004) 056223.
- [152] S. Ladas, R. Imbihl, and G. Ertl. Kinetic oscillations and facetting during the catalytic CO oxidation on Pt(110). *Surf. Sci.* **198** (1988) 42.
- [153] M. Bertram, C. Beta, H. H. Rotermund, and G. Ertl. Complex patterns in a periodically forced surface reaction. *J. Phys. Chem. B* **107** (2003) 9610.
- [154] D. S. *Scientific Foundations of Vacuum Technique*. Wiley, New York (1949).
- [155] J. Davidsen, A. Mikhailov, and R. Kapral. Front explosion in a periodically forced surface reaction. *Phys. Rev. E* **72** (2005) 6214.
- [156] A. S. Mikhailov and K. Showalter. Control of waves, patterns and turbulence in chemical systems. *Physics Reports-Review Section of Physics Letters* **425** (2006) 79.

- [157] P. Coulet and K. Emilsson. Strong resonances of spatially distributed oscillators - A laboratory to study patterns and defects. *Physica D* **61** (1992) 119.
- [158] B. Lindner, J. Garcia-Ojalvo, A. Neiman, and L. Schimansky-Geier. Effects of noise in excitable systems. *Physics Reports-Review Section of Physics Letters* **392** (2004) 321.
- [159] N. G. and P. I. *Self-Organization in Non-equilibrium Systems*. Wiley, New York (1977).
- [160] F. R. and E. W. *Evolution of Complex Systems*. Kluwer, Dordrecht (1989).
- [161] F. Sagues, J. M. Sancho, and J. Garcia-Ojalvo. Spatiotemporal order out of noise. *Reviews of Modern Physics* **79** (2007) 829.
- [162] S. Kadar, J. C. Wang, and K. Showalter. Noise-supported travelling waves in sub-excitable media. *Nature* **391** (1998) 770.
- [163] J. C. Wang, S. Kadar, P. Jung, and K. Showalter. Noise driven avalanche behavior in subexcitable media. *Physical Review Letters* **82** (1999) 855.
- [164] I. Sendina-Nadal, S. Alonso, V. Perez-Munuzuri, M. Gomez-Gesteira, V. Perez-Villar, L. Ramirez-Piscina, J. Casademunt, J. M. Sancho, and F. Sagues. Brownian motion of spiral waves driven by spatiotemporal structured noise. *Physical Review Letters* **84** (2000) 2734.
- [165] S. Alonso and F. Sagues. Noise-induced brownian motion of spiral waves. *Physical Review E* **63** (2001) 46205.
- [166] S. Alonso, I. Sendina-Nadal, V. Perez-Munuzuri, J. M. Sancho, and F. Sagues. Regular wave propagation out of noise in chemical active media. *Physical Review Letters* **87** (2001) 7.
- [167] H. Schuster. *Handbook of Chaos Control*. Wiley-VCH, Weinheim (1999).
- [168] M. Bertram, C. Beta, M. Pollmann, A. S. Mikhailov, H. H. Rotermund, and G. Ertl. Pattern formation on the edge of chaos: experiments with CO oxidation on a Pt(110) surface under global delayed feedback. *Phys. Rev. E* **67** (2003) 036208.
- [169] Z. H. Liu, Y. C. Lai, and J. M. Lopez. Noise-induced enhancement of chemical reactions in nonlinear flows. *Chaos* **12** (2002) 417.
- [170] J. E. Truscott and J. Brindley. Ocean plankton populations as excitable media. *Bulletin of Mathematical Biology* **56** (1994) 981.

- [171] C. S. Zhou and J. Kurths. Noise-sustained and controlled synchronization of stirred excitable media by external forcing. *New Journal of Physics* **7** (2005) 18.
- [172] C. Beta. *Controlling chemical turbulence in surface reactions*. Dissertation, Freie Universitaet Berlin (2004).
- [173] J. Garcia-Ojalvo and J. M. Sancho. *Noise in Spatially Extended Systems*. Springer, New York (1999).
- [174] V. Barelko, I. I. Kurochka, A. G. Merzhanov, and K. G. Shkadinskii. Investigation of traveling waves on catalytic wires. *Chem. Eng. Sci.* **33** (1978) 805.
- [175] S. L. Lane and D. Luss. Rotating temperature pulse during hydrogen oxidation on a nickel ring. *Phys. Rev. Lett.* **70** (1993) 830.
- [176] L. Lobban, G. Philippou, and D. Luss. Standing temperature waves on electrically heated catalytic ribbons. *J. Phys. Chem.* **93** (1989) 733.
- [177] D. Luss. Temperature fronts and pulses on catalytic ribbons. *Physica A* **188** (1992) 68.
- [178] S. J. Dixonwarren, M. Kovar, C. E. Wartnaby, and D. A. King. Pyroelectric single-crystal adsorption microcalorimetry at low-temperatures - oxygen on Ni(100). *Surface Science* **309** (1994) 16.
- [179] Y. Y. Yeo, C. E. Wartnaby, and D. A. King. Calorimetric measurement of the energy difference between 2 solid-surface phases. *Science* **268** (1995) 1731.
- [180] H. H. Rotermund. Imaging of dynamic patterns on surfaces. *Curr. Opin. Solid. St. M.* **3** (1998) 354.
- [181] M. Takeda, H. Ina, and S. Kobayashi. Fourier-transform method of fringe-pattern analysis for computer-based topography and interferometry. *J. Opt. Soc. Am.* **72** (1982) 156.
- [182] D. Malacara, M. Servín, and Z. Malacara. *Interferogram Analysis for Optical Testing*. CRC Press, London, New York, Singapur, 2 edn. (2005).
- [183] D. E. Starr, D. J. Bald, J. E. Musgrove, J. T. Ranney, and C. T. Campbell. Microcalorimetric measurements of the heat of absorption of Pb on well-defined oxides: MgO(100) and p(2 × 1)-oxide on Mo(100). *J. Chem. Phys.* **114** (2001) 3752.

- [184] D. E. Starr and C. T. Campbell. Low-temperature adsorption microcalorimetry: Pb on MgO(100). *J. Phys. Chem. B* **105** (2001) 3776.
- [185] C. T. Campbell and D. E. Starr. Metal adsorption and adhesion energies on MgO(100). *J. Am. Chem. Soc.* **124** (2002) 9212.
- [186] S. Kaiser, T. Maier, A. Grossmann, and C. Zimmermann. Fizeau interferometer for phase shifting interferometry in ultrahigh vacuum. *Rev. Sci. Instr.* **72** (2001) 3726.
- [187] G. K. White. Thermal expansion of Ca, Sr, and Ba at low-temperatures. *Journal of Physics F-Metal Physics* **2** (1972) 865.
- [188] J. Arblaster. *Platinum Met. Rev.* **38** (1994).
- [189] W. T. Berg. Low temperature heat capacity of platinum. *Journal of Physics and Chemistry of Solids* **30** (1969) 69.
- [190] A. C. Luntz. A new detection method for microcalorimetry of single crystal surfaces. *Surface Science* **600** (2006) 3099.
- [191] A. Hagemeyer, B. Jandeleit, Y. M. Liu, D. M. Poojary, H. W. Turner, A. F. Volpe, and W. H. Weinberg. Applications of combinatorial methods in catalysis. *Applied Catalysis A-General* **221** (2001) 23.
- [192] L. F. Garfias and D. J. Siconolfi. In situ high-resolution microscopy on duplex stainless steels. *Journal of the Electrochemical Society* **147** (2000) 2525.
- [193] T. T. Lunt, V. Brusamarello, J. R. Scully, and J. L. Hudson. Interactions among localized corrosion sites investigated with electrode arrays. *Electrochem. Solid. St.* **3** (2000) 271.
- [194] T. Nagatani. Structural transition in pitting corrosion of binary-alloys. *Physical Review A* **45** (1992) 2480.
- [195] T. Nagatani. Multifractality of growth probability-distribution in diffusion-limited-corrosion pit. *Physical Review A* **45** (1992) R6985.
- [196] P. Meakin, T. Jossang, and J. Feder. Simple passivation and depassivation model for pitting corrosion. *Physical Review E* **48** (1993) 2906.
- [197] R. Reigada, F. Sagues, and J. M. Costa. A Monte-Carlo simulation of localized corrosion. *Journal of Chemical Physics* **101** (1994) 2329.

- [198] C. H. Liang and W. Zhang. Fractal characteristic of pits distribution on 304 stainless steel corroded surface and its application in corrosion diagnosis. *Journal of Wuhan University of Technology-Materials Science Edition* **22** (2007) 389.
- [199] Z. Szklarska-Smialowska. Pitting corrosion of aluminum. *Corrosion Science* **41** (1999) 1743.
- [200] N. J. Laycock and S. P. White. Computer simulation of single pit propagation in stainless steel under potentiostatic control. *J. Electrochem. Soc.* **148** (2001) B264.
- [201] D. W. Buzza and R. C. Alkire. Growth of corrosion pits on pure aluminum in 1M NaCl. *Journal of the Electrochemical Society* **142** (1995) 1104.
- [202] H. J. Kreuzer. Low energy electron point source microscopy. *Micron* **26** (1995) 503.

Acknowledgments

First, I would like to thank Prof. Dr. Harm H. Rotermund for giving me the opportunity to join his group, the freedom to choose projects, his constant support and advice, for sharing his expertise, for giving a comfortable working atmosphere, and for emphasizing the fact that doing science has to be fun.

Furthermore, I would also like to thank:

Prof. Dr. Gerhard Ertl for inspiring discussions and for the scientific excellency of the department he built.

Prof. Dr. Mario Dähne for being my second advisor at the Technische Universität Berlin.

Dr. Michael Stich and Dr. Naza Castellanos for being the “perfect contacts”.

Dr. Christian Punckt for the work together in the thin-foil and the forcing projects, for lots of discussions and advice, for technical and computational assistance, and for being a patient teacher.

Dr. Dagmar Krefting, Dr. Carsten Beta, Dieter Bauer, Prahba Kaira, and Dr. Birgit Mirwald-Schulz for the shared work within the dynamic forcing project.

Dr. Sergio Alonso for being an excellent co-worker in the noise project.

Dr. Shafaat Ahmed and Dr. Robert Lynch for their help and cooperation with the AFM and SEM.

Dr. Monika Dornhege for introducing me to the pitting corrosion.

Willi Krauss, Dieter Bauer, and Alex Feargrieve for technical assistance.

Prof. Dr. Alexander S. Mikhailov, Prof. Dr. Frances Sagués, Dr. Markus Eiswirth, and Dr. Oliver Rudzick for helpful discussions.

Peter Klages and Waruno Mahdi for critical reading of early drafts.

All the members of the Fritz Haber Institut Physical Chemistry Department, members of the IMPRS Berlin, people from the University of Limerick Physics Department,

and people from the Dalhousie University Physics Department for an agreeable and enriching time.

The Marie Curie European Project “Patterns” for financial support, and the Fritz Haber Institut for making my work run as completely and smoothly as possible.

Lastly, and most importantly, I wish to thank my family, to whom I dedicate this thesis.

Publications

- C. Punckt, P. S. Bodega, and H. H. Rotermund. **Quantitative measurement of the deformation of ultra-thin platinum foils during adsorption and reaction of CO and O₂.** *Surface Science* **600** (2006) 3101.
- P. S. Bodega, P. Kaira, C. Beta, D. Krefting, D. Bauer, B. Mirwald-Schulz, C. Punckt, and H. H. Rotermund. **High frequency periodic forcing of the oscillatory catalytic CO oxidation on Pt(110).** *New Journal of Physics* **9** (2007) 61.
- P. Kaira, P. S. Bodega, C. Punckt, H. H. Rotermund, and D. Krefting. **Pattern formation in 4:1 resonance of the periodically forced CO oxidation on Pt (110).** *Physical Review E* **77** (2008) 4.
- P. S. Bodega, S. Alonso, and H. H. Rotermund. **Effects of external global noise on the catalytic CO Oxidation on Pt(110).** *Submitted*.
- C. Punckt, P. S. Bodega, P. Kaira, and H. H. Rotermund. **Forest fires in the lab: experiments, simple modeling, and relation to other phenomena.** *In preparation*.

Curriculum Vitae

Name	Pablo Sánchez Bodega
Born	August 23, 1978 in Madrid, Spain
Parents	Jesús Sánchez Rodriguez and Celedonia Bodega López
1982 – 1992	C. P. Méjico Madrid
1992 – 1996	I. E. S. Salvador Dalí (<i>cum laude</i>)
06/1996	Selectividad
09/1996 – 06/2004	Studies in Physics
09/1996 – 10/2003	Universidad Autónoma de Madrid
10/2000 – 07/2001	Università degli Studio di Bologna
10/2003	Physics Diploma
10/2003 – 06/2004	PhD programme Universidad Complutense de Madrid
since 01/2005	PhD student with Prof. H. H. Rotermund at the Department of Physical Chemistry, Fritz-Haber-Institut der Max-Planck-Gesellschaft, Berlin